Measurement of the mass of the W boson in e^+e^- collisions with the OPAL detector

Koji ISHII

The graduate School of Science and Technology, Kobe University

Doctoral thesis, January, 1998

Abstract

The mass of the W boson has been measured using the data taken in 1996 with the OPAL detector at LEP2. We firstly analysed the W^+W^- cross-section at $\sqrt{s}$ = 161 GeV based on a calculation of complete four-fermion processes. The W mass is obtained to be $M_W = 80.40^{+0.44+0.09}_{-0.41-0.10} \pm 0.03$ GeV, where the first and second errors are statistical and systematic, respectively, and the third arises from the beam energy uncertainty. Secondly we utilize the data at $\sqrt{s} = 172$ GeV to measure the W mass directly from the invariant mass of the decay products. The final states of $W^+W^- \rightarrow q\bar{q}'q''\bar{q}'''$ and $W^+W^- \rightarrow q\bar{q}'\ell\bar{\nu}_\ell$ can both be used to measure the W mass, resulting in $M_W = 80.32 \pm 0.30(stat.) \pm 0.09$(syst.) GeV. These measurements of the M_W are in good agreement with those from the other experiments at LEP2 and TEVATRON, and with the indirect determination of the M_W through the radiative corrections in the Standard Model. The combined result at $\sqrt{s}$ = 161-172 GeV is $M_W = 80.35 \pm 0.24(stat.) \pm 0.07(syst.)$ GeV.

Preface

The LEP2, a new phase operation of the LEP accelerator for the pair production of on-shell W^+W^- bosons, started in 1996. It was just the year when I joined the OPAL Collaboration, one of the four experiments at LEP2. Many colleagues of the OPAL collaboration had prepared for the data taking and the physics analyses at the high centre-of-mass energies with looking forward to new expected or unexpected physics phenomena. I took part in the maintenance of the electro-magnetic calorimeter and started to study the measurement of the mass of the W boson. The M_W measurement with a good precision is one of the major goals of the LEP2 programme.

The first collision of the high centre-of-mass energy, $\sqrt{s} = 161$ GeV, started in July 1996, and the first event of the W^+W^- production, $W^+W^- \to q\bar{q}'q''\bar{q}'''$, was observed with the OPAL detector (Figure 0.1) on 14th July. The 161 GeV data were accumulated during July and August, and each experiment collected a data sample of about 10 pb^{-1} luminosity. The OPAL detector obtained a total of 28 W^+W^- candidates at this centre-of-mass energy. After the technical stop, during which additional super-conducting RF cavities were installed, the data taking at $\sqrt{s} = 172$ GeV resumed in October. The run was continued until the beginning of November, and each experiment recorded a data sample of about 10 pb^{-1} again. The OPAL detector further observed 120 W^+W^- candidates well above the W^+W^- production threshold.

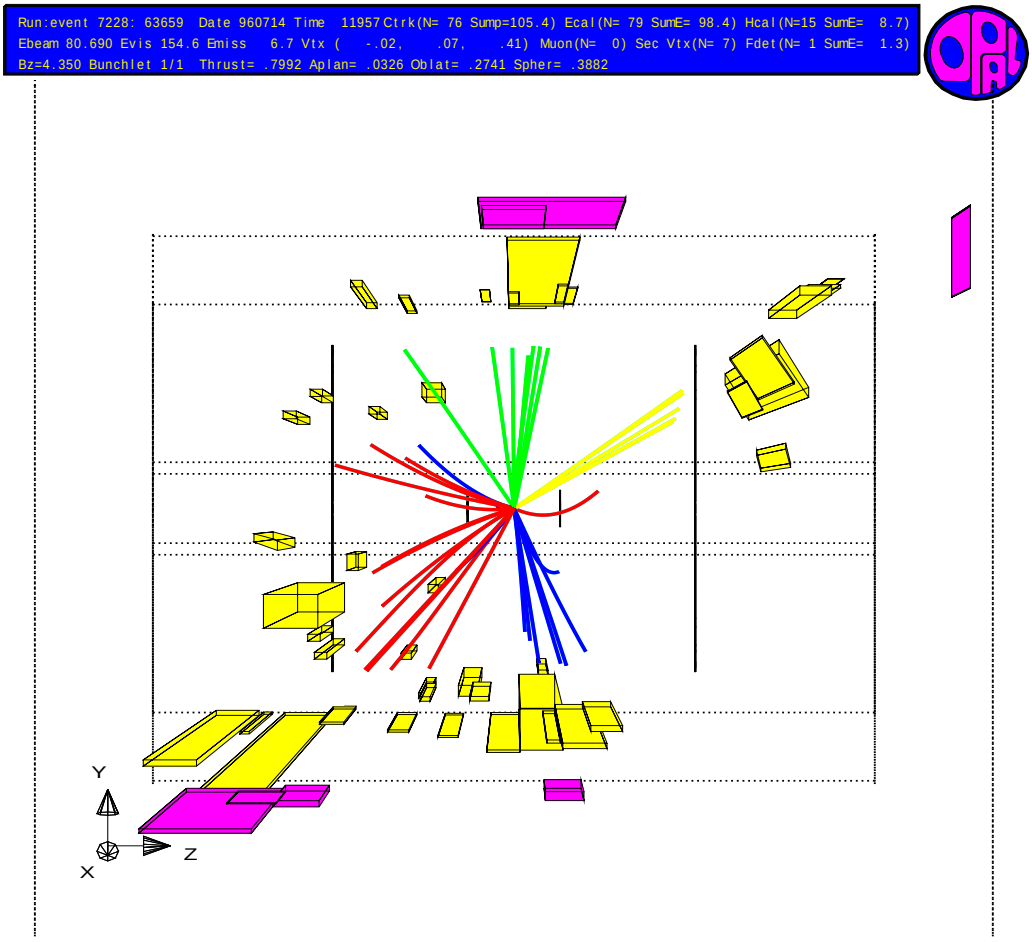

Figure 0.1: The event display of the first $W^+W^- \to q\bar{q}'q''\bar{q}'''$ candidate.

I analysed both of the data samples. Methods of the M_{W} measurement at 161 GeV and at 172 GeV utilized completely different approaches. In the analysis of the 161 GeV data, I contributed to extracting the mass of the W boson from the measured $\mathrm{W^+W^-}$ cross-section. I studied the cross-section based on the calculation of complete four-fermion processes. As the systematic effects including the four-fermion interference are taken into account in this analysis, the result was accepted as the main result in the paper [1] which was published in October 1996. In the analysis of the 172 GeV data, I worked on the mass reconstruction, the direct M_{W} determination, and on the associated systematic effects. The paper [2] which contained all my work at 172 GeV was published in July 1997.

This thesis is based on the above two papers. It also contains a brief summary of the physics motivation, experimental method, the OPAL detector, etc.. In addition, a current status of the M_{W} measurement including the obtained results at $\sqrt{s}$ = 161-172 GeV with the OPAL detector and the future prospect at LEP2 are discussed.

Acknowledgment

This work has been done as a part of the OPAL experiment and thanks are due to all of the physicists and engineers of this experiment for their construction and successful operation.

I would like to thank Prof. Hiroshi Takeda and Prof. Shuji Orito who gave me a chance to join the OPAL Collaboration. I also thank Prof. Kiyotomo Kawagoe who introduced me the W physics with the OPAL detector at LEP2. Also special thanks are due to Prof. Mituaki Nozaki.

I am grateful to the members of the International Center for Elementary Particle Physics (ICEPP) for their discussions and advises. In particular I want to express my gratitude to Prof. Sachio Komamiya who helped me to understand the experimental physics, and to Prof. Tatsuo Kawamoto and Dr. Satoru Yamashita for many bright suggestions to my work.

It is also a pleasure to thank the OPAL collaborators, especially the members of the WW working group. They are very helpful to a newcomer and without their help, I would have never performed my work. I express my thanks to the spokesman of the OPAL collaboration, Rolf D. Heuer, and the conviener of the WW group, Nigel K. Watson.

Finally, I would like to thank the SL Division of CERN for the efficient operation of the LEP accelerator, and other CERN staffs for their support.

Contents

Chapter 1

Introduction

In 1996, the LEP (Large Electron Positron collider) at CERN (European Laboratory for Particle Physics) entered a new phase of operation, LEP2, with the first e^+e^- collisions above the W^+W^- production threshold. One of the principal goals of the LEP2 programme is the measurement of the mass of the W boson, M_W. The precision of M_W is expected to be about 30 MeV with the luminosity of 500 pb^{-1} per experiment at LEP2. Comparison between this direct measurement and the indirect M_W determination from precise electroweak measurements at $\sqrt{s} \sim 91$ GeV (LEP1) and elsewhere will eventually provide an important test of the Standard Model (SM) of electroweak interactions. This thesis describes the measurement of M_W from the observed W^+W^- cross-section at 161 GeV centre-of-mass energy ($\sqrt{s}$) and from the direct reconstruction of the invariant mass from the W decay products at $\sqrt{s} = 172$ GeV.

The structure of the thesis is as follows. Chapter 1 contains a brief overview of the physics motivation together with the experimental methods of M_W measurement at LEP2. Chapter 2 describes the experimental apparatus; the LEP2 accelerator and the OPAL detector. In Chapter 3 the description is given on the data samples, together with the measurements of luminosity and of beam energy. The event reconstruction algorithm and the parameters used in the analyses are explained in Chapter 4. In Chapters 5 and 6, the details of analyses of M_W measurement at 161 GeV and 172 GeV are presented, respectively. Finally Chapter 7 discusses the current status of M_W measurement.

1.1 Physics Motivation

The theory of the electroweak interaction, known as the Standard Model together with QCD for strong interaction, is a present-day basis in elementary particle physics. It is a gauge invariant quantum field theory with the symmetry group $SU(2) \times U(1)$, spontaneously broken by the Higgs mechanism. Experimentally the Standard Model is well tested and established with many precision measurements of its parameters. No discrepancy is found so far between the theory and the experiments. In this framework the force is transferred by exchanging an intermediate particle, called "Gauge Boson". Four kinds of intermediate particles, γ, g, Z^0, and $W^\pm$ are experimentally observed. The photon, γ, is the intermediate particle of the electromagnetic interaction, and is massless. The gluon, g, is the carrier of the strong interaction, and also massless. On the other hand, weak bosons, Z^0 and $W^\pm$, which mediate the weak interaction, are heavy, having masses of about 90 GeV and 80 GeV, respectively. In the Standard Model,

the origin of the massive gauge bosons is explained by the spontaneous symmetry-breaking, and an undiscovered neutral Higgs particle is believed to be the origin of the masses of all the particles except its own. The masses of the massive gauge bosons are basic parameters in the Standard Model, and therefore precise measurement of the masses are of fundamental physical importance.

According to the Standard Model prediction with a Higgs doublet, we obtain the relation between the massive gauge bosons,

$$M_{\mathrm{Z}} = \frac{M_{\mathrm{W}}}{\cos\theta_{\mathrm{W}}},$$

where θ_{W} is the weak mixing angle in the lowest order expression. A brief introduction of this relation in the Standard Model is given in Appendix A. Current precision of the measured M_{Z} is about 0.002 % (91.1867 $\pm$ 0.0020 GeV) mainly determined by the extremely precise measurements at LEP1. On the other hand, before the start of LEP2, M_{W} is measured with a precision of only about 2 % at $\mathrm{p\bar{p}}$ collider; $M_{\mathrm{W}} = 80.33\pm$ 0.15 GeV [3, 4, 5].

Assuming the Standard Model to be correct, M_{W} can be deduced from various precise measurements, mainly from LEP1. The M_{W} can thus be indirectly determined with a precision of 0.5 %, $M_{\mathrm{W}} = 80.329 \pm 0.041$ GeV. Compared to the direct measurement, the precision is about 4 times better. If the error of the direct measurement can be made compatible to, or better than that of the indirect one, *i.e.* $< O(50)$ MeV, it becomes a good test of the Standard Model. Previous studies [6] of the physics potential of LEP2 indicated that with the luminosity of 500 pb^{-1} one may directly measure the W boson mass with a precision in the range 30 - 50 MeV.

Furthermore, the improved M_{W} measurement may constrain the allowed values of the Higgs boson mass in the Standard Model. The masses M_{W}, M_{t}, and M_{H} are related through radiative corrections, and M_{H} decreases as M_{W} increases. In particular, if M_{W} has a high value, M_{H} is strongly constrained. An assumption with $M_{\mathrm{W}} = 80.43 \pm 0.04$ GeV and $M_{\mathrm{t}} = 175.6 \pm 3$ GeV leads to $M_{\mathrm{H}} \leq 180$ GeV, in the framework of the Standard Model with a calculation including higher order radiative corrections [7].

A precise value of M_{W} obtained from the direct measurement could contradict the value determined indirectly by the global fit of the electroweak measurements, thus indicating a breakdown of the Standard Model. The Minimal Supersymmetric Standard Model (MSSM) is one of the most promising new-physics candidates. It is therefore important to consider the MSSM prediction for M_{W}. Figure 1.1 shows W mass as a function of M_{t} in the Standard Model (solid lines) and in the MSSM (dashed lines). In each case the prediction is indicated by a band, corresponding to a variation of the model parameters. In the Standard Model case, the M_{H} is dominant, and the band corresponds to the range 70 GeV $\leq M_{\mathrm{H}} \leq$ 1000 GeV. The MSSM bound is calculated by varying the SUSY parameters so that they are consistent with current experimental results of non-observation of the Higgs and SUSY particles at LEP2 [7].

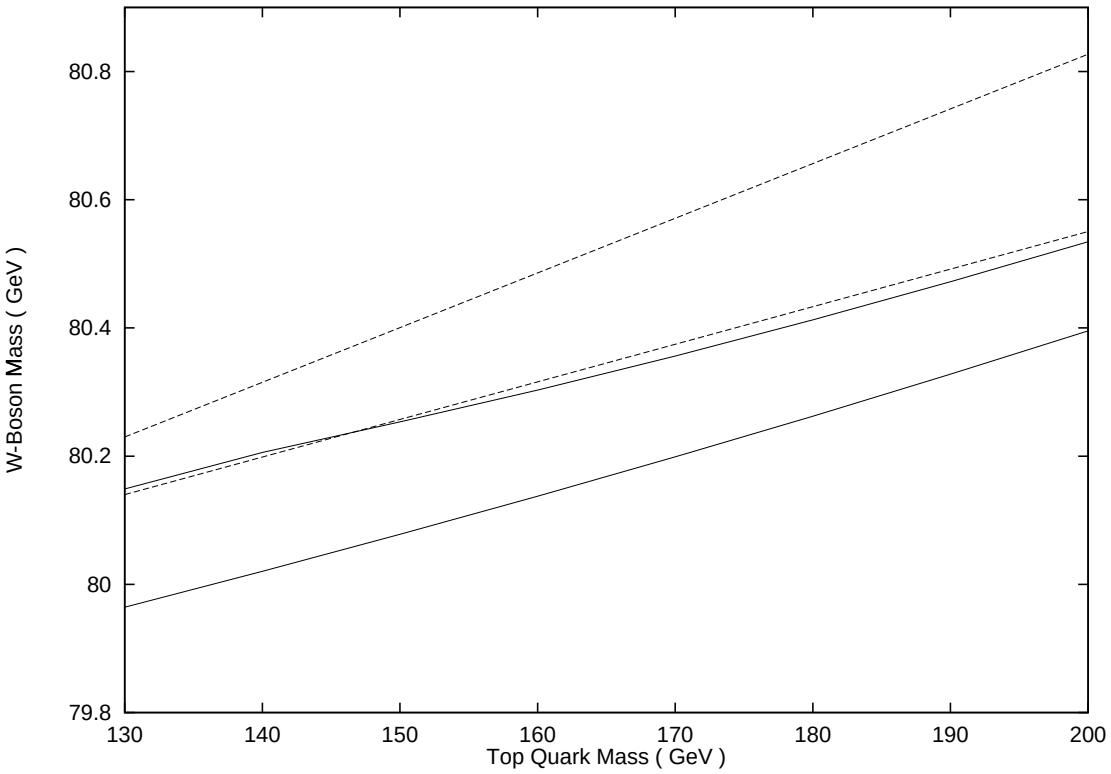

Figure 1.1: Predictions for M_{W} as a function of M_{t} in the SM (solid lines) and in the MSSM (dashed lines), from Ref.[7].

As discussed in the next section, methods of M_{W} measurement at LEP2 are different with that at the $\mathrm{p\bar{p}}$ collider. Before starting the LEP2 experiments, M_{W} value is dominantly determined by the measurements at CDF and D0 experiments of Fermilab TEVATRON $\mathrm{p\bar{p}}$ collider, in which M_{W} is measured by using the transverse mass. The $\mathrm{e^+e^-}$ collider is suitable for a precision measurement like the determination of M_{W}, and two different methods are available to determine M_{W} in the LEP2 programme. As these three measurements at LEP2 and at the $\mathrm{p\bar{p}}$ collider are considered as independent, they provide a good cross-check and the results can be combined.

1.2 Methods of Measuring the Mass of W Boson

In the Standard Model, three Feynman diagrams mainly contribute to the $\mathrm{W^+W^-}$ production[1] in $\mathrm{e^+e^-}$ interactions; the s-channel γ and $\mathrm{Z^0}$-boson exchange and the t-channel ν_{e} exchange, shown in Figure 1.2 (a). The W boson decays into a quark-antiquark pair, for example $\mathrm{W^-} \rightarrow \bar{\mathrm{u}}\mathrm{d}$ or $\bar{\mathrm{c}}\mathrm{s}$, which forms well separated two hadronic jets, or into a lepton-neutrino pair, $\mathrm{W^-} \rightarrow \ell\bar{\nu}_\ell$ [2]. In general, since neutrinos can not be observed directly, the event topologies are classified to the three categories having the following characteristics; (1) 4-jets with no missing momentum, (2) 2-jets + 1 lepton with large missing momentum, and (3) 2 acoplanar leptons with large missing momentum.

[1] In this thesis, the W pair production diagrams are referred to as "CC03", following the notation of [6].
[2] It implicitly includes the charge conjugate state.

(a) The W^+W^- production diagrams (in this example, $e^+e^- \to u\bar{u}d\bar{d}$).

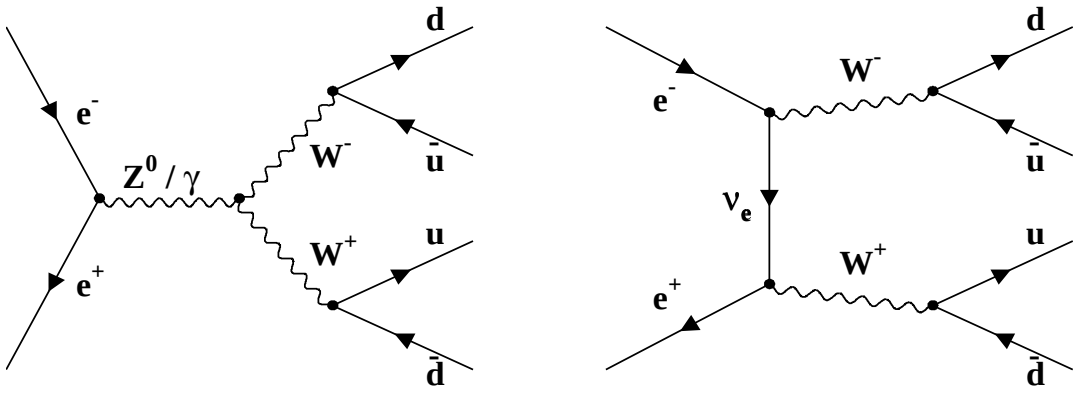

(b) The four-fermion diagrams which interfere with the W^+W^- production processes.

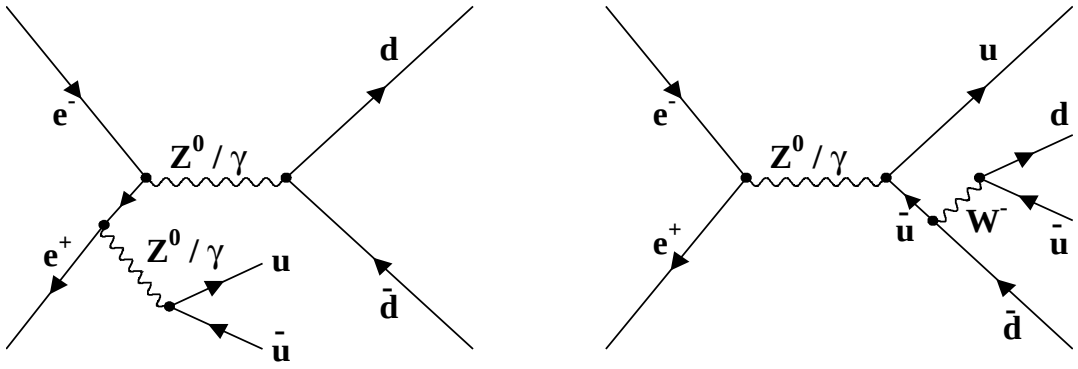

Figure 1.2: Examples of W^+W^- production and four-fermion diagrams.

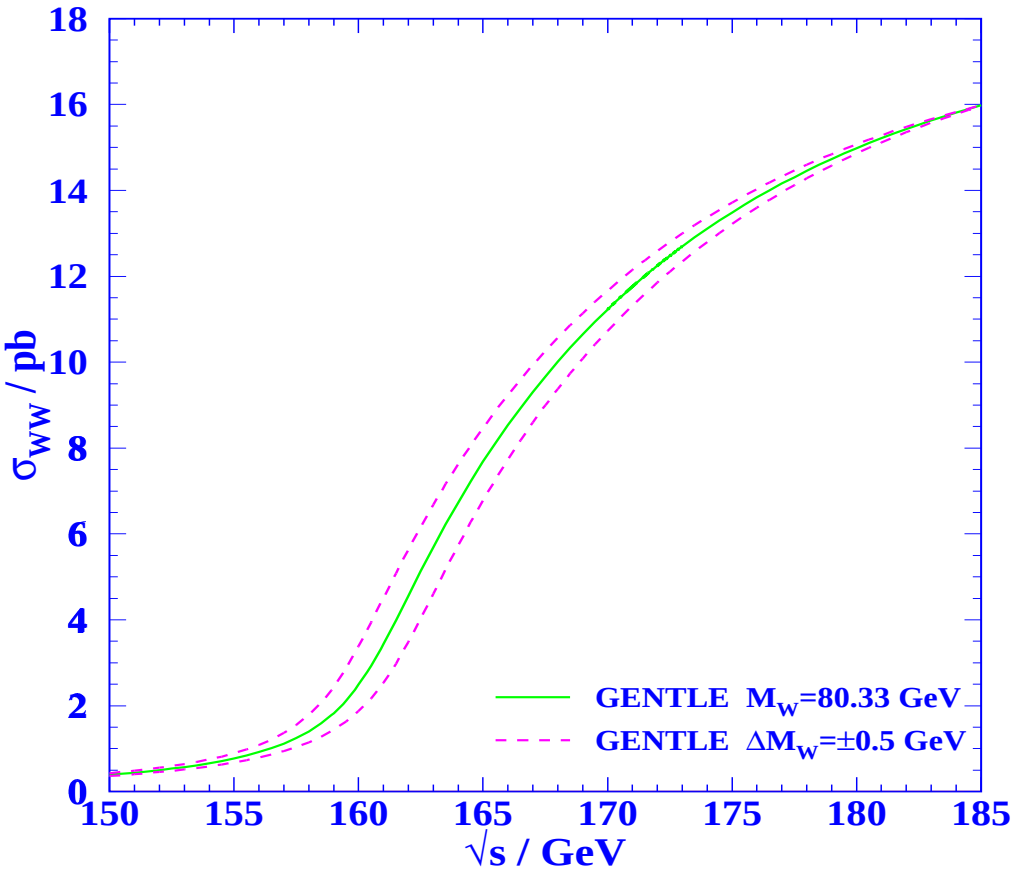

Figure 1.3: The Standard Model W^+W^- cross-section dependence on the centre-of-mass energy in the threshold region. Solid line shows the prediction by GENTLE [8] for $M_W = 80.33$ GeV. Dashed lines represent the cases for $M_W = 79.83$ and 80.83 GeV.

Analyses are performed to measure M_W using the observed quantities of these events. In principle M_W can be measured using (A) the rapidly varying total cross-section at threshold, (B) the sharp (Breit-Wigner) peaking behavior of the invariant mass distribution of the $W^\pm$ decay products, and (C) the sharp end-point spectrum of the lepton energy in $W^\pm$ decay.

Figure 1.3 shows the cross-section for W^+W^- production as a function of $\sqrt{s}$ in the threshold region, for different values of M_W. In this figure, the semi-analytic programme GENTLE [8] is used to calculate the W^+W^- cross-section, which includes the finite width effects, the Coulomb correction and Initial State Radiations. The statistical power of the method (A) is maximum at the centre-of-mass energy $\sqrt{s} \simeq 2M_W + 0.5$ GeV, giving $\Delta M_W \simeq 90$ MeV with an integrated luminosity of 100 pb^{-1} assuming 100 % signal efficiency and no background.

Figure 1.4 shows the invariant mass spectrum of the W^+W^- Monte Carlo samples. The plotted mass is a simple mean of the two reconstructed W masses and perfect detector resolutions are assumed. The statistical power of the method (B) is estimated to be $\Delta M_W \sim \Gamma_W/\sqrt{N} \simeq$ 50 MeV / 100 pb^{-1} in this case and again 100 % signal efficiency and no background are assumed. The statistical error of the method (C) is determined by the statistical error of the measurement of the lepton end-point energy. The end-point of the distribution is considerably smeared by finite width effects and by initial state radiations, and only a fraction of events close to the end-point are sensitive to M_W. This significantly weakens the statistical power, resulting in about 10 times worse statistical precision than those of the other two methods.

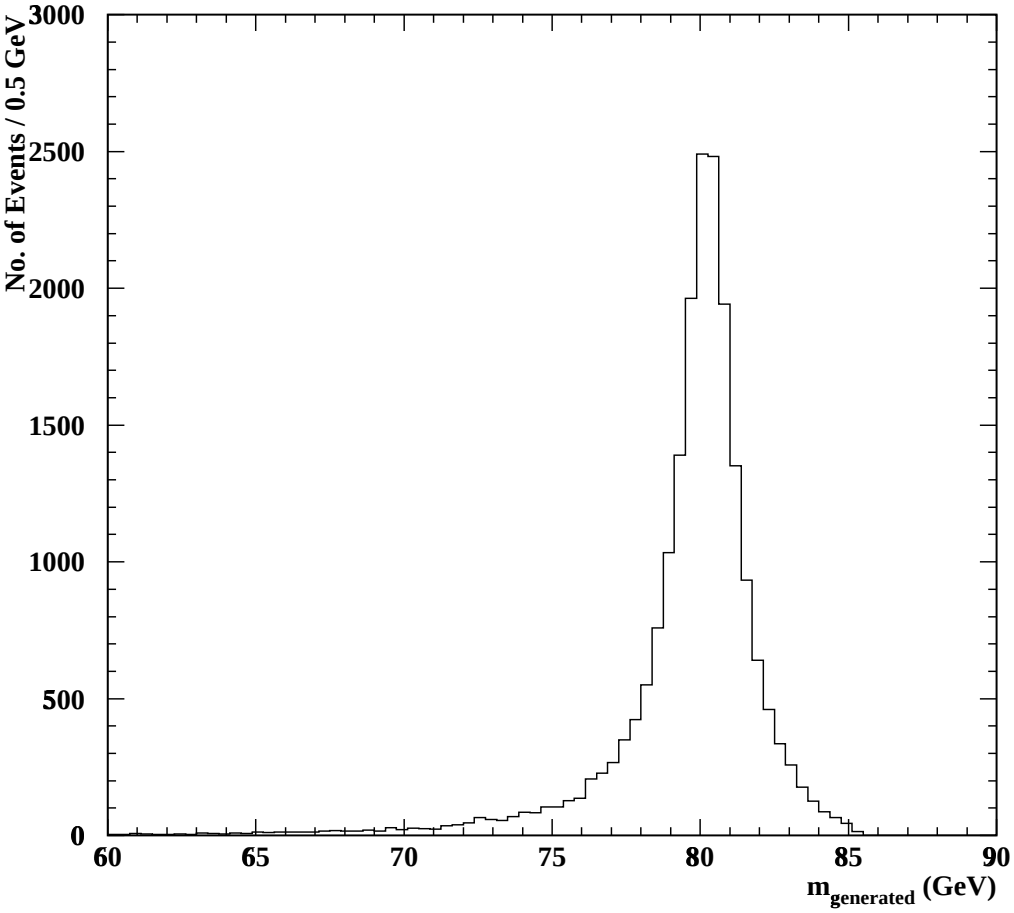

Figure 1.4: Illustration of the invariant W mass peak.

The statistical precision of the method (A) is comparable to that of the method (B) in realistic estimations. Because the two methods have the different systematic errors, they can be used for an internal cross-check with each other on the W mass measurements with at LEP2 experiments. This is one of the motivations for spending some luminosity at the threshold region. The cross-section method is not useful at higher centre-of-mass energy well above the W^+W^- threshold. For example, the error of M_W at $\sqrt{s} = 172$ GeV using the method (A) is about 5 times worse than that at $\sqrt{s} = 161$ GeV, with the same integrated luminosity. In contrast, the direct reconstruction method (B) is invalid at the threshold region due to the low number of observed events. Therefore, at $\sqrt{s} = 161$ GeV only the method (A) is used to determine the W mass and at higher centre-of-mass energies, $\sqrt{s} \sim 172$ GeV, the M_W measurement is mainly performed with the method (B).

Chapter 2

Experimental Apparatus

2.1 Accelerator

The CERN Large Electron Positron (LEP) collider is a 26.67 km circumference e^+e^- storage ring across the border between Switzerland and France (Figure 2.1). This collider was built to investigate the electroweak theory with high precision. In the first phase (LEP1), the collider is operated at the centre-of-mass energy of the $Z^0 \rightarrow q\bar{q}$ resonance ($\sim$ 91 GeV) and it produced a large number of Z^0 bosons. From the analyses of using these Z^0 decay products, quite many important physics results, like a precision measurement of mass of the Z^0 boson, have been obtained.

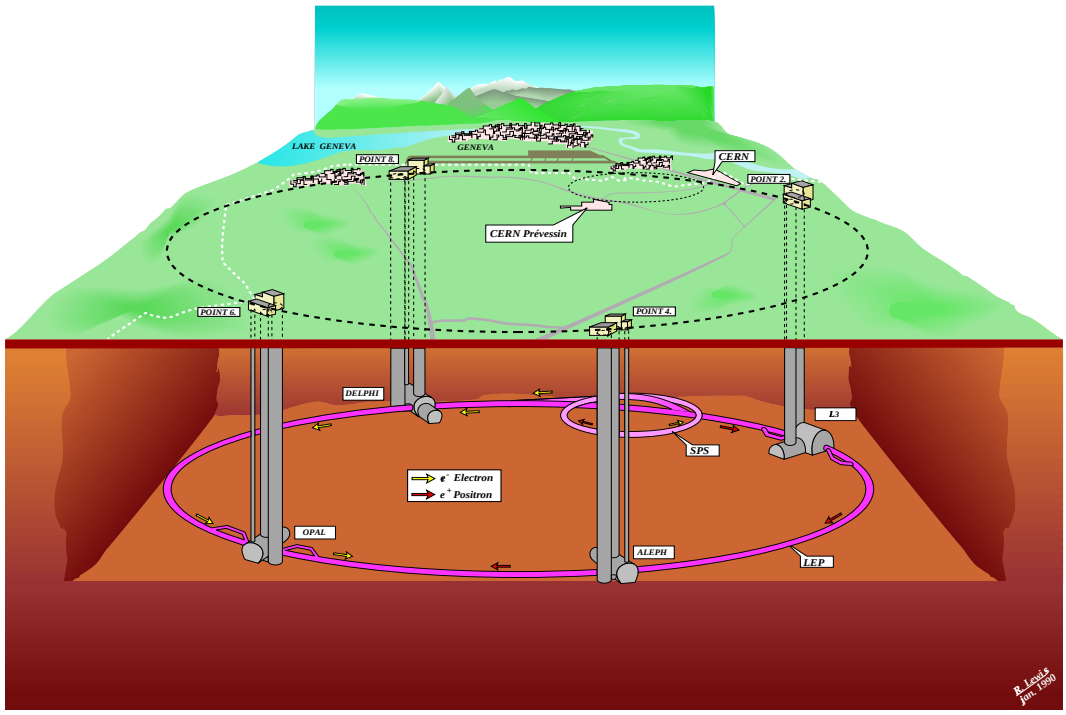

Figure 2.1: Overview of the LEP collider.

In 1996 the centre-of-mass energy is raised above the W^+W^- production threshold ($\geq$ 161 GeV) to start the second phase operation (LEP2). The measurement of mass of the W boson is one of the major goals as well as searches for new particles, such as the Higgs boson. The LEP2 will be running until 1999 and planning to collect a total integrated luminosity more than 500 pb^{-1} for each experiment.

The performance and condition of LEP2 during 1996 run are described elsewhere [9] in detail. Only a brief summary of the structure of the LEP and the accelerating system for LEP2 are described in this section.

2.1.1 Structure

The LEP storage ring consists of eight straight sections connected by the same number of curved sections. The ring is situated underground, in a tunnel of 3.8 m inner diameter, at an average depth of 100 m. Electrons and positrons are constrained in the vacuum chamber along the nominal orbit by the electro-magnetic guide field system. The system consists of dipole, quadrupole and sextupole magnets, dipole correctors in horizontal and vertical directions, rotated quadrupoles, and electrostatic deflectors. The curved sections are occupied by sets of standard cells consisting of these magnets. The beams are bent by the dipole field of about 0.1 T, which is unusually low as a circular accelerator, in order to reduce the radiative energy loss. The quadrupoles produce alternating-gradient focussing, and the sextupoles are used to compensate the energy dependence of the focusing strength. In the middle of the eight straight sections are the interaction points. Four of them are surrounded by solenoidal magnets used by the detectors of the experiments. Beams are focussed tightly at the interaction points by the strong quadrupole field generated by a set of superconducting magnets to obtain maximum luminosity. Typical transverse dimension of the beam at an interaction point is about 10 μm $\times$ 250 μm in the vertical and horizontal plane respectively. The longitudinal dimension is typically $\sim$ 2 cm.

2.1.2 Accelerating System

The LEP storage ring is the last one in a chain of five accelerators. Electrons are generated at the end point of the 200 MeV linac and are accelerated by the electrostatic field. Positrons are generated by the positron converter which converts some of the accelerated electrons into the positrons. Electrons and positrons are then accelerated up to 600 MeV by a linac. Accelerated particles are injected into the Electron-Positron Accumulating ring (EPA). The role of this ring is to generate bunches for electrons and positrons with a high intensity and a constant energy. The high intense beams are transferred to the CERN Proton Synchrotron (CERN-PS) which operates as a 3.5 GeV synchrotron. The PS injects the beams into the next circular accelerator, Super Proton Synchrotron (CERN-SPS), operating as a electron-positron injector for LEP. Particles are further accelerated up to 20 GeV in this ring and finally they are transferred to the LEP ring. After the transfer, the LEP accelerating system accelerates the bunches up to the full energy required for collisions.

Since the particles are constrained to a circular motion, they continually lose energy through the emission of synchrotron radiation. The Radio-Frequency (RF) acceleration installed in the straight section of the LEP ring compensates this energy loss and maintains the beams in their

orbit. In the initial phase, LEP1, the RF system consisted 120 RF cavities made of copper, powered by klystrons. With the conventional copper cavities, however, the power dissipated as heat in the cavities. To reduce this power dissipation RF cavities made of superconducting material is developed for the higher beam energy of the second phase operation, LEP2. Before the LEP2 operation in 1996, 144 superconducting cavities were installed to enable LEP2 to be operated at 80.5 GeV per beam. After the summer shutdown for installation of additional 32 superconducting cavities, LEP2 was operated at 86 GeV per beam.

2.2 The OPAL Detector

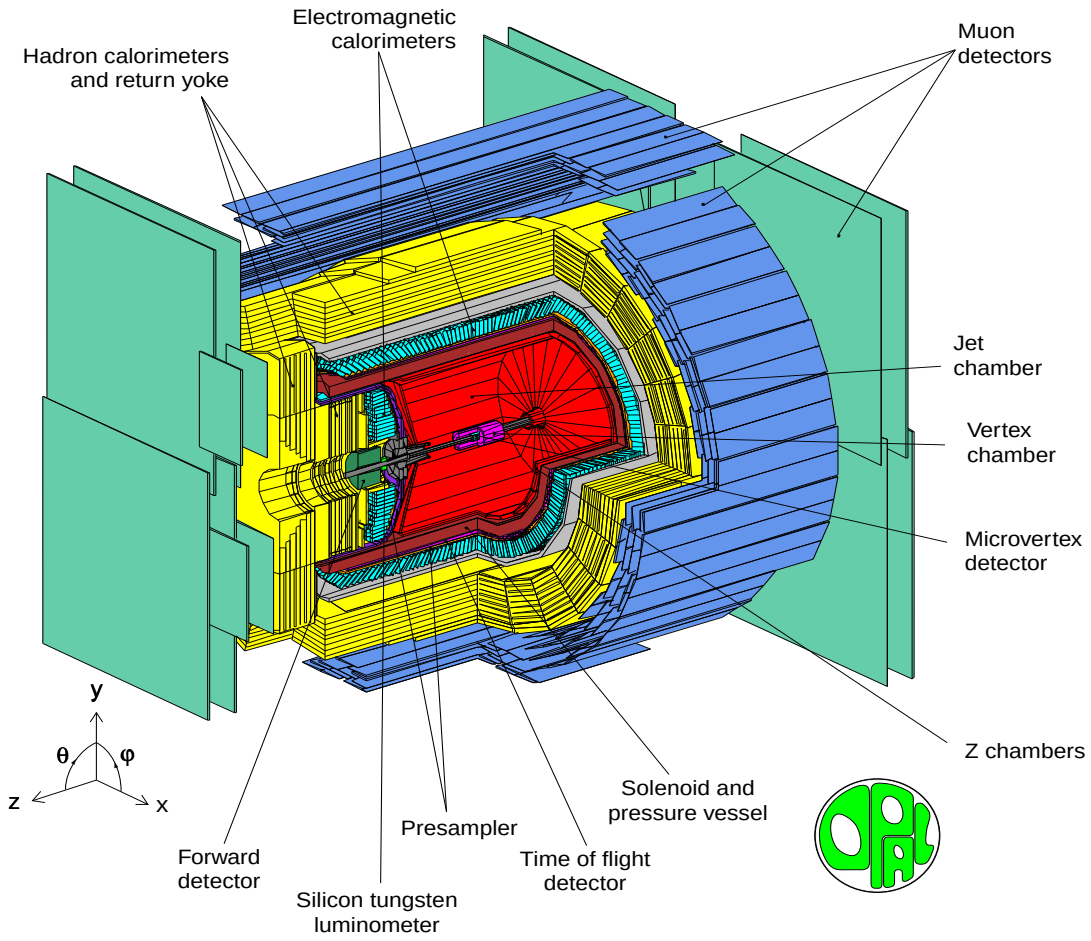

Figure 2.2: General layout of the OPAL detector.

OPAL (**O**mni-**P**urpose **A**pparatus for **L**EP) is a multipurpose apparatus designed to reconstruct efficiently and identify all types of e^+e^- events. The main features of the OPAL detector are:

- Detecting charged particles in the central region of a solenoidal coil, measurements of their direction and momentum with their trajectories, particle identification by their dE/dx, and reconstruction of primary and secondary vertices at and near the interaction.
- Identification of photons and electrons, and measuring their energy.

- Measurement of hadronic energy by the total absorption using the magnet yoke instrumented as a calorimeter.
- Identification of muons by measurement of their position and direction within and behind the hadron absorber.
- Measurement of absolute machine luminosity using Bhabha scattering events in very forward direction with respect to the beam line.

The general layout of the detector is shown in figure 2.2, indicating the location and relative size of the various components. Figure 2.3 shows cross sections of the detector parallel and perpendicular to the beam axis. The OPAL right-handed coordinate system is defined such that the origin is at the geometric centre of the jet chamber, z is parallel to, and has positive sense along, the e^- beam direction, r is the coordinate normal to z, θ is the polar angle with respect to $+z$ and ϕ is the azimuthal angle around z. Full details of the OPAL detector can be found in [10, 11, 12] and only a brief introduction is given here.

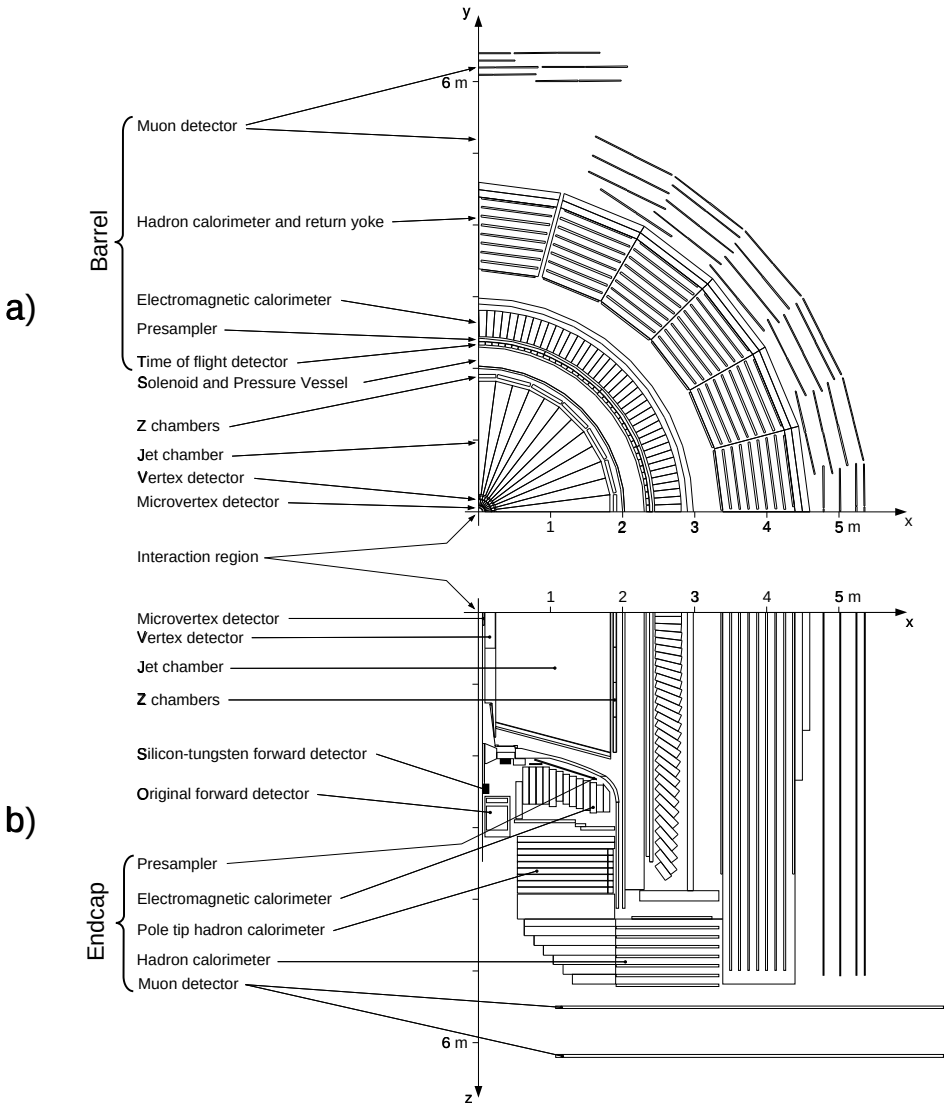

Figure 2.3: Cross section of a quadrant of the detector (a) perpendicular to the LEP beam axis, and (b) parallel to the beam axis.

2.2.1 The Central Detector

The Central Detector consists of a Silicon Microvertex detector and three drift chamber devices, the vertex detector, jet chamber and surrounding Z-chambers located inside a pressure vessel holding a pressure of 4 bar. The central detector is inside a solenoid supplying a uniform axial magnetic field of 0.435 T. Originally (< 1991) there was no Silicon detector and the inner wall of the pressure vessel at 7.8 cm radius formed the beam pipe. This beam pipe consisted of 0.13 cm thick carbon fibre with a 100μm aluminium inner lining. In 1991 the second beam pipe at a radius of 5.35 cm, consisting of 0.11 cm thick Beryllium, was added and the Silicon detector was inserted between them.

Silicon Microvertex Detector: The Silicon Microvertex Detector consists of two barrels of single sided Silicon Microstrip Detectors at radii of 6 and 7.5 cm. The inner layer consists of 12 ladders and the outer of 15. Each ladder consists of 5 silicon wafers daisy chained together. There are 629 strips per detector at 25μm pitch and each strip is read out at 50μm pitch. The detector was originally installed in OPAL in 1991 and had $r-\phi$ readout only. In 1993 an upgraded detector was installed that had $r-\phi$ and $r-z$ wafers glued back to back.

Vertex Detector: The vertex detector is a high precision cylindrical jet drift chamber. It is 100 cm long with a radius of 23.5 cm and consists of two layers of 36 sectors each. The inner layer contains axial sectors, each containing a plane of 12 sense wires strung parallel to the beam direction. The wires range radially from 10.3 to 16.2 cm with a spacing of 0.583 cm. The outer layer contains stereo sectors each containing a plane of 6 sense wires inclined at a stereo angle of $\sim 4°$. The stereo wires lie between the radii 18.8 and 21.3 cm with a spacing of 0.5 cm. A precise measurement of the drift time on to the axial sector sense wires allows the $r-\phi$ position to be calculated. Measuring the time difference between signals at either end of the sense wires allows a fast but relatively coarse z coordinate that is used by the OPAL track trigger and in pattern recognition. A more precise z measurement is then made by combining axial and stereo drift time information offline. Multiple hits on a wire can be recorded.

Jet Chamber: The jet chamber is a cylindrical drift chamber of 400 cm in length with an outer radius of 185 cm and an inner one of 25 cm. The chamber consists of 24 identical sectors each containing a sense wire plane of 159 wires strung parallel to the beam direction. The end planes are conical and can be described by $|z| = 147 + 0.268 \times R$. The coordinates of wire hits in the $r-\phi$ plane are determined from a measurement of drift time. The z coordinate is measured using a charge division technique and by summing the charges received at each end of a wire allows the energy loss, $\mathrm{d}E/\mathrm{d}x$ to be calculated.

Z-Chamber: The Z-chambers provide a precise measurement of the z coordinate of tracks as they leave the jet chamber. They consist of a layer of 24 drift chambers 400 cm long, 50 cm wide and 5.9 cm thick covering 94% of the azimuthal angle and the polar angle range $|\cos\theta| < 0.72$. Each chamber is divided in z into 8 cells of 50 cm$\times$50 cm, with every cell containing 6 sense wires spaced at 0.4 cm.

2.2.2 Electromagnetic Calorimeter

The function of the electromagnetic calorimeter is to detect and identify electrons and photons. It consists of a lead glass total absorption calorimeter split into a barrel and two end cap arrays. This arrangement together with two forward lead scintillator calorimeters of the forward detector makes the OPAL acceptance for electron and photon detection almost 99% of the solid angle.

The presence of ∼2 radiation lengths of material in front of the lead glass (mostly due to the solenoid and pressure vessel), results in most electromagnetic showers initiating before reaching the lead glass. Presampling devices are therefore installed in front of the lead glass in the barrel and endcap regions to measure the position and energy of showers to improve overall spatial and energy resolutions and give additional γ/π^0 and electron/hadron discrimination. In front of the Presampler is the Time of Flight Detector.

Time-Of-Flight Counters: The Barrel time-of-flight system provides charged particle identification in the range 0.6 to 2.5 GeV, fast triggering information and an effective rejection of cosmic rays. It consists of 160 scintillation counters forming a barrel layer 684 cm long at a mean radius of 236 cm surrounding the OPAL coil covering the polar angle range $|\cos\theta| < 0.82$. In 1996 the Tile Endcap system was added to enhance the triggering information available from the forward region, and to identify which bunches in a bunch train are responsible for a particular observed collision. It consists of a 10mm thick scintillator layer, between the endcap presampler and the endcap electromagnetic calorimeter, divided into tiles and read out using embedded wavelength-shifting fibers.

Barrel Electromagnetic Presampler: The Barrel Electromagnetic Presampler consists of 16 chambers forming a cylinder of radius 239 cm and length 662 cm covering the polar angle range $|\cos\theta| < 0.81$. Each chamber consists of two layers of drift tubes operated in the limited streamer mode with anode wires running parallel to the beam direction. Each layer of the tubes contains 1 cm wide cathode strips on both sides at $\pm 45°$ to the wire direction. Spatial positions can then be determined by reading out the strips in conjunction with a measurement of the charge collected at each end of the wires to give a z coordinate by charge division. The hit multiplicity is approximately proportional to the energy deposited in the material in front of the presampler, allowing the calorimeter shower energy to be corrected with a corresponding improvement in resolution.

Barrel Lead Glass Calorimeter: The barrel lead glass calorimeter consists of a cylindrical array of 9440 lead glass blocks at a radius of 246 cm covering the polar angle range $|\cos\theta| < 0.81$. Each block is 24.6 radiation lengths, 37 cm in depth and $\sim 10 \times 10$ cm^2 in cross-section. In order to maximise detection efficiency the longitudinal axis of each block is angled to point at the interaction region. The focus of this pointing geometry is slightly offset from the e^+e^- collision point in order to reduce particle losses in the gaps between blocks. Čerenkov light from the passage of relativistic charged particles through the lead glass is detected by 3 inch diameter phototubes at the base of each block.

Endcap Electromagnetic Presampler: The endcap presampler is a multiwire proportional counter located in the region between the pressure bell and the endcap lead glass detector. The device consists of 32 chambers arranged in 16 sectors covering all ϕ and the polar angle range $0.83 < |\cos\theta| < 0.95$.

Endcap Electromagnetic Calorimeter: The endcap electromagnetic calorimeter consists of two dome-shaped arrays of 1132 lead glass blocks located in the region between the pressure bell and the pole tip hadron calorimeter. It has an acceptance coverage of the full azimuthal angle and $0.81 < |\cos\theta| < 0.98$. As opposed to the barrel calorimeter, the endcap lead glass blocks follow a non-pointing geometry being mounted coaxial with the beam line. The lead glass blocks provide typically 22 radiation lengths of material and come in three lengths (38, 42 and 52 cm) to form the domed structure following the external contours of the pressure bell. The blocks are read out by special Vacuum Photo Triodes operating in the full OPAL magnetic field.

2.2.3 Hadron Calorimeter

The hadron calorimeter is built in three sections; the barrel, the endcaps and the pole-tips. By positioning detectors between the layers of the magnet return yoke a sampling calorimeter is formed covering a solid angle of 97% of 4π and offering at least 4 interaction lengths of iron absorber to particles emerging from the electromagnetic calorimeter. Essentially all hadrons are absorbed at this stage leaving only muons to pass on into the surrounding muon chambers.

To correctly measure the hadronic energy, the hadron calorimeter information must be used in combination with that from the preceding electromagnetic calorimeter. This is necessary due to the high probability of hadronic interactions occurring in the 2.2 interaction lengths of material that exists in front of the iron yolk.

Hadron Endcap and Barrel Calorimeter: The barrel region contains 9 layers of chambers sandwiched between 8 layers of 10 cm thick iron. The barrel ends are then closed off by toroidal endcap regions which consist of 8 layers of chambers sandwiched between 7 slabs of iron. The chambers themselves are limited streamer tube devices strung with anode wires 1 cm apart in a gas mixture of isobutane(75%) and argon(25%) that is continually flushed through the system. The signals from the wires themselves are used only for monitoring purposes. The chamber signals result from induced charge collected on pads and strips located on the outer and inner surfaces of the chambers respectively. The layers of pads are grouped together to form towers that divide up the detector volume into 48 bins in ϕ and 21 bins in θ. The analogue signals from the 8 or so pads in each chamber are then summed to produce an estimate of the energy in hadronic showers. The strips consist of 0.4 cm wide aluminium that run the full length of the chamber, centered above the anode wire positions. They hence run parallel to the beam line in the barrel region and in a plane perpendicular to this in the endcaps. Strip hits thus provide muon tracking information with positional accuracy limited by the 1 cm wire spacing. Typically, the hadronic shower initialised by a normally incident 10 GeV pion produces 25 strip hits and generates a charge of 600 pc.

Hadron Pole-Tip Calorimeter: Complementing the barrel and endcap regions, the pole-tip extends the coverage of hadron calorimeter from $|\cos\theta| = 0.91$ down to 0.99. The sampling frequency in this region is increased to 10 in an effort to improve the OPAL energy resolution in the forward direction. The detectors themselves are 0.7 cm thick multiwire proportional chambers containing a gas mixture of CO_2 (55%) and n-pentane (45%), strung with anode wires at a spacing of 0.2 cm. Again, the chambers have pads

on one side (of typical area 500 cm^2) and strips on the other. Corresponding pads from the 10 layers then form towers analogous to the treatment in the rest of the calorimeter.

2.2.4 Muon Detector

The muon detector aims to identify muons in an unambiguous way from a potential hadron background. To make the background manageable, particles incident on the detector have traversed the equivalent of 1.3 m of iron so that the probability of a pion not interacting is reduced to be less than 0.001.

Barrel Muon Detector: The barrel region consists of 110 drift chambers that cover the acceptance $|\cos\theta| < 0.68$ for four layers and $|\cos\theta| < 0.72$ for one or more layers. The chambers range in length between 10.4 m and 6 m in order to fit between the magnet support legs and all have the same cross sectional area of 120 cm×9 cm. Each chamber is split into two adjoining cells each containing an anode signal wire running the full length of the cell, parallel to the beamline. The inner surfaces of the cells have 0.75 cm cathode strips etched in them to define the drift field and in the regions directly opposite the anode wires are diamond shaped cathode pads. In all, six signals are read out from each cell namely, one from each end of the anode wire and four from the cathode pads and are digitised via an 8-bit FADC. Spatial position in the ϕ plane is derived using the drift time onto the anode and can be reconstructed to an accuracy of better than 0.15 cm. A rough estimate of the z coordinate is also achieved by using the difference in time and pulse height of the signals arriving at both ends of the anode wire. A much better measure of the z coordinate is given by using induced signals on two sets of cathode pads whose diamond shape repeats every 17.1 cm and 171 cm respectively. This results in a z coordinate accurate to 0.2 cm, modulo 17.1 cm or accurate to 3 cm modulo 171 cm.

Endcap Muon Detector: Each endcap muon detector consists of two layers of four quadrant chambers (6 m×6 m) and two layers of two patch chambers (3 m×2.5 m), for an angular coverage of $0.67 < |\cos\theta| < 0.985$. Each chamber is an arrangement of two layers of limited streamer tubes in the plane perpendicular to the beam line, where one layer has its wires horizontal and the other vertical. The basic streamer tube used has a cross section of 0.9 cm×0.9 cm with the inner walls coated with a carbon-suspension cathode. Each plane of tubes is open on one side and closed on the other to rows of aluminium strips 0.8 cm wide. The strips on the open side, run perpendicular to the tube anode wires and typically have charge induced over five or so strips. By finding a weighted average using the recorded pulse heights, the streamer is located to better than 0.1 cm. The strips on the closed side run parallel to the tube wires and so can only give that coordinate to the nearest wire or $0.9/\sqrt{12}$ cm. Within each chamber therefore, with two layers of tubes each with two layers of strips, the x and y coordinates of a track can be measured once accurately and once relatively coarsely. As with the barrel region, the actual position of the strips is known to about 0.1 mm via survey information.

2.2.5 The Forward Detector

The forward detector consists of an array of devices, listed below, whose primary objective is to detect low angle Bhabha scattering events as a way of determining the LEP luminosity for

the normalisation of measured reaction rates from Z^0 decays.

To achieve this, the forward detector is covering angles from the interaction point between 40 to 150 mrad, with the only obstructions being the beam pipe and 2 mm of aluminium from the central detector pressure vessel in the horizontal and vertical planes.

- Calorimeter. The forward calorimeter consists of 35 sampling layers of lead-scintillator sandwich divided into a presampler of 4 radiation lengths and the main calorimeter of 20 radiation lengths.
- Tube Chambers. There are three layers of proportional tube chambers positioned between the presampler and main sections of the calorimeter. The positioning is known to ± 0.05 cm and they can give the position of a shower centroid to ± 0.3 cm.
- Gamma Catcher. The gamma catcher is a ring of lead scintillator sandwich sections of 7 radiation lengths thickness. They plug the hole in acceptance between the inner edge of EE and the start of the forward calorimeter.
- Far Forward Monitor. The far forward monitor counters are small lead-scintillator calorimeter modules, 20 radiation lengths thick, mounted either side of the beampipe 7.85 m from the intersection region. They detect electrons scattered in the range 5 to 10 mrad that are deflected outwards by the action of LEP quadrupoles.

2.2.6 Silicon Tungsten Detector

The silicon tungsten detector is a sampling calorimeter designed to detect low angle Bhabha scattering events in order to measure the luminosity. There are 2 calorimeters at ± 238.94cm in z from the interaction point with an angular acceptance of 25 mrad to 59 mrad. Each calorimeter consists of 19 layers of silicon detectors and 18 layers of tungsten. At the front of each calorimeter is a bare layer of silicon to detect preshowering, the next 14 silicon layers are each behind 1 radiation length (3.8mm) of tungsten and the final 4 layers are behind 2 radiation lengths (7.6 mm) of tungsten.

Each silicon layer consists of 16 wedge shaped silicon detectors. The wedges cover 22.5° in ϕ with an inner radius at 6.2 cm and an outer one at 14.2 cm. The wedges are subdivided into 64 pads (32 in r and 2 in ϕ) giving a total of 38912 channels which are read out individually. Adjacent wedges in a layer are offset by 800μm in z and positioned in such a way that there is no gap in the active area of the silicon. Consecutive layers in the detector are offset in ϕ by half a wedge (11.25°) so that any cracks between the tungsten half–rings do not line up.

2.2.7 Trigger

Events are only recorded by the data acquisition system if they satisfy certain trigger conditions. Subdetector trigger signals divide into two categories, 'stand-alone' signals such as multiplicity counts or energy sums, and lower threshold signals from a 6×24 binning in θ and ϕ respectively. The trigger processor makes its decision by forming correlations in space between subdetectors in θ/ϕ together with the stand-alone signals. Similarly, subdetector pretrigger signals divide into 'stand-alone' signals from energy sums, and lower threshold signals from 12 bins in θ/ϕ. The pretrigger processor makes its decision by multiplicity counting and possibly forming correlations in θ/ϕ between subdetectors, together with the stand–alone signals.

Chapter 3

Data and Monte Carlo Samples

3.1 Data Samples

In 1996, the initial year of LEP2, the first e^+e^- collisions above the W^+W^- production threshold were performed at centre-of-mass energies, 161.3, 170.3 GeV, and 172.3 GeV. The data recorded by the OPAL detector at these energies approximately correspond to luminosity of 9.9, 1.0, and 9.3 pb^{-1}, respectively. The mass of the W boson is determined using these data samples.

The measured integrated luminosities, $\mathcal{L}$, and the measured centre-of-mass energy, $\sqrt{s}$, are given below. As the data samples at $\sqrt{s} = 170.3$ and 172.3 GeV are analysed together, the combined luminosity and the luminosity weighted mean centre-of-mass energy are presented.

$$\begin{aligned} \mathcal{L} &= 9.890 \pm 0.042(\text{stat.}) \pm 0.040(\text{syst.})\text{pb}^{-1} \text{ at } \sqrt{\text{s}} = 161.3 \pm 0.05 \text{ GeV} \\ \mathcal{L} &= 10.363 \pm 0.045(\text{stat.}) \pm 0.036(\text{syst.})\text{pb}^{-1} \text{ at } \sqrt{\text{s}} = 172.12 \pm 0.06 \text{ GeV} \end{aligned}$$

The luminosity measurement is performed by the silicon-tungsten luminometer using small-angle Bhabha scattering events [13]. The average beam energy is measured at two lower energy points using the technique of resonant depolarisation, and then the energy scale at LEP2 was inferred by an extrapolation based on the measurements of magnetic field with a number of NMR probes in the LEP dipole magnets, and the flux-loop measurement of the integrated LEP dipole field [14]. A summary of these measurements is described below.

3.1.1 Luminosity Measurement

The integrated luminosity is measured using small-angle Bhabha scattering events, $e^+e^- \rightarrow e^+e^-$, recorded in the forward calorimeter. Independent measurements are available from two separate devices: a high precision silicon-tungsten luminometer, covering angles between 25 and 59 mrad from the beam, and a lead-scintillator sampling calorimeter instrumented with streamer tubes, covering the region from 40 to 150 mrad. These devises have been described in section 2.2.

Bhabha scattering events with the silicon-tungsten luminometer are selected by requiring a high energy cluster in each end of the detector, as described below. The energy in each calorimeter have to be at least half the beam energy, and the average energy had to be at

least three quarters of the beam energy. The two highest energy clusters are required to be back-to-back in ϕ, $||\phi_R - \phi_L| - \pi| < 200$ mrad, where ϕ_R and ϕ_L are the azimuthal angles of the cluster in the right- and left-hand calorimeter respectively. They are also required to be collinear, by placing a cut on the difference between the radial positions, $\Delta R \equiv |R_R - R_L| < 25$ mm, where R_R and R_L are the radial coordinates of the clusters on a plane approximately 7 radiation lengths into the calorimeter. This cut, corresponding to an acollinearity angle of about 10.4 mrad, effectively defines the acceptance for single-photon radiative events, thus reducing the sensitivity of the measurement to the detailed energy response of the calorimeter.

The inner and outer radial acceptance cuts delimit a region between 38 and 52 mrad on one side of the calorimeter, while for the opposite calorimeter a wider zone between 34 and 56 mrad is used. Two luminosity measurements are performed; the narrower acceptance on one side plus the wider acceptance on the other side, and vice versa. The final measurement is the average of the two and has no first-order dependence on beam offsets or tilts. The cross-section for Bhabha scattering accepted by these cuts is calculated using the Monte Carlo programme BHLUMI [15]. The error on the luminosity measurement is dominated by data statistics. The statistical error amounts to 0.42% and 0.43% at 161 GeV and 172 GeV, respectively. The largest systematic uncertainty arises from theoretical knowledge of the cross-section 0.25%, with detector effects amounting to 0.20% (0.23%) at 161 (172) GeV.

The second luminosity measurement is provided by the forward detector. The selection of Bhabha events within the calorimeter acceptance is the following: $\overline{\phi} > 15°$ away from vertical and horizontal axes, where $\overline{\phi} = (\phi_R + \phi_L - \pi)/2$; acoplanarity $|\Delta\phi - \pi| < 20°$, where $\Delta\phi = |\phi_R - \phi_L|$; $\mathrm{E}_L + \mathrm{E}_R > (2/3)\sqrt{s}$; $\mathrm{E}_{L,R} > 0.225\sqrt{s}$. Here E_L, E_R are the energies deposited in the left and right forward detectors. The acceptance is limited to the region between 65 and 105 mrad because of the silicon-tungsten luminometer on the inside front edge of the device. The overall acceptance of the calorimeter is measured by normalising to the precisely known cross-section for hadronic events at the Z^0 peak, and applying small corrections derived from Monte Carlo simulations. Knowledge of the hadronic acceptance for the Z^0 data is the main source of the systematic error in the forward detector luminosity measurement, which amounts to 1.0%.

The luminosity measured by the forward detector agreed with that measured by the silicon-tungsten luminometer within one standard deviation of the combined results. The latter is used in this analysis since the measurement of the silicon-tungsten luminometer is more precise. The approximate total error amounts to 0.6 %, including the systematic errors.

3.1.2 Beam Energy Measurement

In the W mass measurement at LEP2, an uncertainty of the beam energy is directly contributed to the error of M_{W}. Therefore it is significant to measure the beam energy with a good precision.

The momentum of the electron and positron beams circulating in LEP2 is proportional to the magnetic bending field integrated over the path of the particles. For particles on the central orbit, *i.e.* passing through the centre of the quadrupoles and sextupoles, the momentum is dominantly determined by the field of the main bending magnets of dipoles. However, small constant fields such as the Earth's magnetic field or remanent fields in the beam pipe additionally contribute to the bending field. Contributions from the quadrupoles and the sextupoles also have to be considered for non-central orbits. In order to measure the absolute

beam energy a precise calibration is necessary. This beam energy calibration is performed with the technique of resonant depolarisation, which is well established in the measurement of the LEP1 beam energy [16]. The magnetic field measurements are performed in two ways, using the flux loop which provides a calibration of the non-linearity of the ensemble of the LEP dipoles, and using a set of NMR probes which provides a precise measurement of the local magnetic field in a sample of LEP dipole magnets.

Resonant spin depolarisation:

Resonant depolarisation determines the beam energy by measuring the frequency with which the spins of transversely polarised electrons rotate about the vertical bending field. This technique measures the beam energy under conditions very close to those of data-taking runs and is by far the most precise method available. The transversely polarized electrons are depolarised in a controlled way by applying an oscillating horozontal magnetic field. Under the influence of such a weak field the spins are slightly rotated away from the vertical axis on each turn, and a depolarising resonance occurs if the depolarising field is in phase with the spin precession. The number of spin precessions per revolution, the spin tune ν_s, is related to the beam energy via

$$E_{beam} \;=\; \frac{\nu_s \;\times\; m_e c^2}{(g_e - 2)/2} \;\equiv\; 0.4406486 \text{ GeV} \;\times\; \nu_s,$$

where $(g_e - 2)/2$ is the magnetic moment anomaly of the electron, m_e is the electron mass, and c is the speed of light. The depolarising field is applied once per turn, and therefore the resonance occurs at a frequency which is independent of the integer part of the spin tune: $f_{dep} = (\nu_s \text{ - int}(\nu_s)) \times f_{rev}$, where $f_{rev} = 11245.50$ H_Z is the revolution frequency of the beam particles. The integer part of ν_s is well known from the other calibration techniques, since a unit tune change corresponds to a ~ 440 MeV change in beam energy. The frequency f_{dep} of the RF magnet is produced with a synthesized function generator. According to the instrument specifications, f_{dep} is generated with an accuracy 25×10^{-3} H_Z.

Flux loop:

The flux loop consists of closed electrical loops around the pole tips of every magnet in the ring. The voltage induced in the loop when the whole dipole system undergoes a magnetic cycle of a given excursion allows a measurement of the variation of the magnetic flux up to beam energies of 100 GeV. The response curve of the magnets can be obtained to an absolute precision at the level of ~ 5 MeV.

NMR probes:

The 16 NMR probes are installed in dipole magnets in the tunnel. There is at least one probe in each octant, and in octants 1 and 5 there are strings of 5 probes in adjacent dipoles. The limitation is not in the accuracy in the measurement of the magnetic field, good to $\sim 10^{-6}$, but in the fact that the NMR's sample a very small fraction of the guiding field. This set of NMR probes provides a very precise and continuous measurement of the local magnetic field, on-line with the operation of the machine.

In 1996 the maximum energy at which a depolarisation measurement was achieved was 50 GeV, and the beam energy calibrations were made at the energies 45 and 50 GeV. This fixes

the lever arm to 5 GeV, over which the extrapolation of magnetic measurements can be tested. The beam energies of LEP2 are around 80.5 and 86 GeV, so that the measured uncertainties must be scaled by 30.5/5 and 36/5 for the two running periods.

The detailed results of the LEP energy calibration in 1996 are found in [14]. The absolute beam energy is determined by the calibrated dipole field measurements, and is found to be 150 MeV larger than the nominal value. The flux loop and NMR energy measurements agree to about 10 MeV at the physics energy, and show similar linear extrapolation properties. The extrapolation error estimates from NMR and flux loop data are typically 10 to 12 MeV. However these rely heavily on a single fill in which resonant depolarisation measurements were made at two different energies. Taking into account the worst case of the consistency between the depolarisation and NMR data, the extrapolation errors of 24 and 29 MeV are assigned at the beam energy 80.5 and 86 GeV, respectively. Including other errors of energy scale such as fill-by-fill normalisation, the error of variation within a fill, and the error of interaction point specific, the total errors are estimated to be 27 MeV at the beam energy 80.5 GeV and 30 MeV at 86 GeV.

3.2 Monte Carlo Samples

A number of Monte Carlo models are used to provide estimates of efficiencies and backgrounds as well as the shapes of the W mass distributions. The majority of the Monte Carlo samples are generated at $\sqrt{s}$ = 161 and 171 GeV with M_{W} =80.33 GeV. Unless stated otherwise, all Monte Carlo samples are generated with a full simulation of the OPAL detector [17]. A number of Monte Carlo studies are also performed without detector simulation, referred as "generator level".

The separation between the signal and background processes is complicated by the interference between the $\mathrm{W^+W^-}$ production diagrams (class CC03) and other four-fermion diagrams. For example, the process $\mathrm{Z^0/\gamma \rightarrow q\bar{q}}$ where a $\mathrm{W^{\pm}}$ is radiated off one of the quarks can interfere with $\mathrm{W^+W^- \rightarrow q\bar{q}'\ell\bar{\nu}_\ell}$ and $\mathrm{W^+W^- \rightarrow q\bar{q}'q''\bar{q}'''}$ final states. The effect of the interference is included in samples of four-fermion final states (including $\mathrm{W^+W^-}$) using models such as grc4f [18] or EXCALIBUR [19]. In both cases samples are generated using the full set of interfering four fermion diagrams. Monte Carlo samples of $\mathrm{W^+W^-}$ events, restricted to the CC03 diagrams, are obtained with the PYTHIA [20], KORALW [21], HERWIG [22], grc4f [18] and EXCALIBUR [19] generators. A number of PYTHIA Monte Carlo samples generated with different values of $\sqrt{s}$ and M_{W} are used to investigate the sensitivities of the analyses to these parameters. To study the effect of the Γ_{W}, the EXCALIBUR generator is used. The selection efficiencies for the $\mathrm{W^+W^-}$ events are estimated by using the KORALW generator.

The main background process, $\mathrm{Z^0/\gamma \rightarrow q\bar{q}}$, is simulated using PYTHIA, while HERWIG and ARIADNE [23] are used as alternatives to study possible systematic effects. Other backgrounds involving two fermions in the final state are studied using KORALZ [24] for $\mathrm{e^+e^- \rightarrow \mu^+\mu^-}$ and $\mathrm{e^+e^- \rightarrow \tau^+\tau^-}$, and BHWIDE [25] for $\mathrm{e^+e^- \rightarrow e^+e^-}$. Backgrounds from processes with four-fermions in the final state are evaluated using grc4f, EXCALIBUR and FERMISV [26]. Two-photon background processes with hadronic final states are simulated using PYTHIA and PHOJET [27] at low Q^2. At high Q^2 TWOGEN [28], PYTHIA, and HERWIG programmes are used. The Vermaseren programme [29] is used to simulate purely leptonic final states in two-photon

processes. At least two independent Monte Carlo estimates are available for each category of two-photon and four-fermion backgrounds.

To calculate the Standard Model W^+W^- cross-section, the semi-analytic programme GENTLE [8] is used. The use of GENTLE is motivated by the fact that it provides a more complete calculation than current Monte Carlo generators[6]. The calculated cross-sections are 3.77 and 12.4 pb^{-1} at $\sqrt{s} = 161.3$ and 172.12 GeV, respectively, using the current world-average W boson mass of $M_W = 80.33$ GeV [3, 4]. Throughout in this thesis, the GENTLE programme is used to calculate the expected number of W^+W^- events.

Chapter 4

Event Reconstruction

The event records accepted by each subdetector have to be reconstructed, *i.e.* the raw detector data are converted into physical quantities such as particle energies or momenta. In this section the process of the event reconstruction is described.

4.1 Charged Tracks and Energy Clusters

In the OPAL detector, the particles in an event are regarded as the reconstructed charged tracks or energy clusters. The charged particle trajectories are reconstructed using the central tracking detector; silicon microvertex detector, vertex detector, jet-chamber, and Z-chamber. In each subdetector, the raw data are converted to hit coordinates through the calibration. A pattern recognition is then performed, in which track segments from each component of the central detector are compared and associated to form a set of tracks. For each track, a fit is done in r-phi and in r-z independently, where the sets of hits from the associated segments are fit to obtain the five parameters of a helix (κ, ϕ_0, d_0, $\tan\lambda$, and z_0) and the covariance matrix in these parameters, taking into account of the multiple Coulomb scattering errors. The parameters of the helix are the curvature κ, the azimuthal angle ϕ_0 made by the track tangent at the nominal interaction point, the distance of closest approach d_0 from the track to the beam axis in r-phi, the track co-tangent θ, and the distance z_0 along the beam axis from the nominal interaction point, respectively. These parameters are related to the physics quantities of the charged tracks as

$$\begin{aligned} p_t &= a \mid \frac{B_z}{\kappa} \mid, \\ p_x &= p_t \cos\phi_0, \\ p_y &= p_t \sin\phi_0, \\ p_z &= p_t \tan\lambda, \end{aligned}$$

where B_z is the axial magnetic field along the z axis and a is the constant, $a = \mathrm{c}/2 \times 10^{-14} \simeq 1.5 \times 10^{-4}$. The integrated charge measured at both ends of the signal wire in the jet chamber is summed up and used to calculate the $\mathrm{d}E/\mathrm{d}x$ in the chamber gas. The $\mathrm{d}E/\mathrm{d}x$ of each charged track is used for particle identification.

The "good" charged track is defined to reject the poor reconstruction like the noise track. The selection criteria are as follows;

- the transverse momentum, p_t, exceeds 150 MeV,
- the absolute momentum, $|\vec{p}|$, is less than 90 GeV,
- the track has at least 40 measured hits of the jet chamber and more than 50 % of the hits geometrically expected,
- the track comes from the cylinder of 50.0 cm in length and 2.0 cm in radius at the center of the nominal interaction point ($|z_0| < 25.0$ cm and $|d_0| < 2.0$ cm),
- the χ^2 of the track fitting should be less than 100 both in r-phi and in r-z.

The resolutions of the various parameters, used for "good" charged track, have been investigated with the $e^+e^- \rightarrow \mu^+\mu^-$ events in the calibration data, which were recorded with an integrated luminosity of 1.2 pb^{-1} at the Z^0 peak during 1996. The resolutions of the d_0 and ϕ_0 are obtained to be about 20 μm and 0.24 mrad. The momentum resolution, σ_p/p^2, is found to be 1.5×10^{-3} GeV^{-1}. The effects of mis-calibrations of the tracks are also studied using di-muon events in the high statistics LEP1 data samples. The calibration of the muon momentum scale is found to be accurate within 1 %.

The electromagnetic energy clusters are formed with the barrel and endcap electromagnetic calorimeter. In the barrel region "good" electromagnetic energy clusters are required to have an energy of at least 100 MeV, while in the endcap region they are required to have at least 250 MeV. The energy scale of the electromagnetic cluster is investigated with the $e^+e^- \rightarrow e^+e^-$ events in the same high statistics data samples. The accuracy of the energy scale is understood within 1 %.

The hadronic clusters are reconstructed with the barrel, the endcap, and the pole-tip hadron calorimeters. The energy resolution of the calorimeter for hadrons is about $120/\sqrt{E}$ % (E in GeV). A "good" hadronic cluster should have an energy exceeding 250 MeV.

4.2 Particle Identification

For the selected "good" tracks and clusters, a particle identification is performed for further analyses. In general, electrons are identified by requiring a good matching between the measured directions of a track and a cluster, and by requiring the dE/dx and the E/p ratio to be consistent with the expectations for an electron, where the dE/dx, E, and p are the ionisationn energy loss, the electromagnetic cluster energy, and the track momentum, respectively. Muons are identified if a track has associated hits in the muon chambers or the hadron calorimeter and deposites only a small energy in the electromagnetic cluster. These electron and muon identifications are used in the analysis of the $W^+W^- \rightarrow q\bar{q}'e\bar{\nu}_e$, $q\bar{q}'\mu\bar{\nu}_\mu$ and $\ell^-\bar{\nu}_\ell\ell'^+\nu_{\ell'}$ event selections at $\sqrt{s}$ = 161 GeV, described in Appendix B.2 and B.4. In the $q\bar{q}'e\bar{\nu}_e$ and $q\bar{q}'\mu\bar{\nu}_\mu$ event selections at $\sqrt{s}$ = 172 GeV, the probability of electron or muon from the $W \rightarrow e\bar{\nu}_e$ or $W \rightarrow \mu\bar{\nu}_\mu$ is defined to identify it, instead of the explicit electron or muon identification. These identifications are described in Appendix C.2.1. The identification of tau lepton is more complicated because the tau lepton decays immediately through various decay modes. A tau is treated as a narrow jet in the selection of the 161 GeV analysis, and the probability of the tau from the $W \rightarrow \tau\bar{\nu}_\tau$ is defined and used in the selection of the 172 GeV analysis.

Since neutrinos can not be detected directly, the missing momentum is taken as the neutrino momentum in an event where only one neutrino is expected to be produced. For the $W^+W^- \rightarrow q\bar{q}'e\bar{\nu}_e$ and $W^+W^- \rightarrow q\bar{q}'\mu\bar{\nu}_\mu$ channels, the missing momentum is used to reconstruct the invariant mass of the W boson.

Quarks convert themselves into hadronic jets through fragmentation process. The assignment of the tracks and clusters to a jet and reconstruction of the jet momentum are described later. No attempt is made to identify the quark flavor.

4.3 Jet-Finding

A quark is fragmented by the strong interaction process, which converts the high energy quark into a hadronic jet. The 3-momentum of the observed jet is considered as that of the quark and therefore assignment of particles to the jets is important for the reconstruction of the quark quantities, in particular, in the case of multi-jet event. This assignment is called as jet-finding, and several standard algorithms exist. Throughout this thesis, the "Durham" jet-finding algorithm [30] is used. This algorithm finds the jets based on the jet resolution parameter, y_{ij}, defined as

$$y_{ij} = \frac{2\min(E_i^2, E_j^2)(1 - \cos\theta_{ij})}{E_{sum}^2},$$

where E_i is the energy of the particle i, E_{sum} is the sum of E_i and E_j, and $\cos\theta_{ij}$ is the angle between two particles. For all the possible combinations, the pair of particles with the smallest y_{ij} value is grouped and replaced by one artificial particle k with an energy $E_k = E_i + E_j$ and 3-momentum $\vec{p_k} = E_k/|\vec{p_i} + \vec{p_j}| \times (\vec{p_i} + \vec{p_j})$. This procedure is repeated until all the pairs have the jet resolution parameters exceeding a threshold value y_{cut} or a required number of jets are reconstructed.

4.4 Jet Energy Reconstruction

Particles, *i.e.* tracks and clusters, are assigned to the jets by the above jet-finding algorithm. However, hadronic jet is an ensemble of charged hadrons, photons, charged leptons, and neutral hadrons. It is not obvious how to combine the information from tracking chambers, calorimeters and muon chambers, and construct jet quantities, avoiding double counting of signals from the different detector components. In OPAL there are two alternative algorithms for jet energy reconstruction; Globally Corrected Energy flow algorithm (GCE) [31] and the Matching method (MT) [31, 32]. The GCE sums up all the energies of tracks and calorimeter clusters in a jet, and corrects for the estimated amount of double counting based on a parameterisation for the single charged particle response in calorimeters. The MT tries to reconstruct 4-vectors of individual particle (charged particle, photon and neutral hadron). Tracks and unassociated calorimeter clusters are identified as charged particles and neutral particles, respectively. Track-associated clusters are then examined. If a cluster is identified as due to an overlap of a neutral particle and charged particle(s), the cluster energy is corrected for the estimated contribution from the charged particle, and used to construct the 4-vector of the neutral particle.

In both algorithms, the energy scale of a jet is found to be accurate within 1 % using the di-jets events of the calibration data samples at $\sqrt{s} \sim M_{\mathrm{Z}}$. The reconstructed jet energies and directions of these data samples are also compared with those of the Monte Carlo samples to investigate the deficiencies in the detector simulation for the jet reconstruction. The observed accuracies are the same in both cases, about 1 %.

In this thesis the GCE algorithm is used as the standard method. Because the jet quantities are essential to reconstruct the invariant mass of the W decay products, the alternative algorithm, MT, is used as a consistency check and to evaluate the systematic error.

4.5 Constrained Kinematic Fit

When some kinematic constraints can be imposed, a kinematic fit is used to improve the precision of event reconstruction. In the calculation of the invariant mass from the W decay products, the mass resolution is greatly improved by incorporating the constraints of the energy-momentum conservation. A kinematic fit is also useful to reduce background and poorly reconstructed events on the bases of the χ^2 probability on the hypothesis. The kinematic fit used in this thesis attempts to minimise the χ^2 value under the constraint of $\mathbf{f}(\mathbf{x}) = 0$;

$$\chi^2 = (\mathbf{x} - \mathbf{m})^{\mathrm{T}} \cdot \mathrm{G} \cdot (\mathbf{x} - \mathbf{m})$$

where $\mathbf{x}$ is a vector of parameters to be fitted, $\mathbf{m}$ is the vector of input parameters, and G^{-1} is the covariance matrix of the input parameters.

For the input parameters in the invariant mass reconstruction, one scalar momentum and two directions are used for each quark or lepton. A total of 12 parameters are input to reconstruct the W mass. The detailed discussion of using the kinematic fit for the invariant mass reconstruction is described in Section 6.2.3 together with a study of input parameters themselves and their errors.

4.6 Effective Centre-of-mass Energy

At energies above the Z^0 resonance, the initial state radiation, often involving radiative return to the Z^0 pole, plays an important role. Therefore it is useful to estimate the effective centre-of-mass energy of the event, $\sqrt{s'}$, excluding the initial state photon. The $\sqrt{s'}$ is calculated by

$$\sqrt{s'} = \sqrt{s - 2E_\gamma \sqrt{s}},$$

where E_γ is the energy of the initial state photon. To find a possible initial state photon two ways are tried; firstly by explicitly searching for an isolated photon in the electromagnetic calorimeter, and secondly by performing a kinematic fit to the event, where the event is considered as a system of jets and a photon aligned along the beam direction. When the kinematic fit fails, the $\sqrt{s'}$ is computed simply from the jet angles.

4.7 Hadronic Event

A multihadron event is defined on the basis of multiplicities of the electromagnetic clusters and the charged tracks [33]. The following criteria are used:

- at least 7 clusters
- at least 5 tracks
- the total energy deposited in the lead glass of at least 10% of the centre-of-mass energy;

$$R_{vis} \equiv \frac{\Sigma E_{clus}}{\sqrt{s}} > 0.1,$$

- the energy balance along the beam direction which satisfies

$$R_{bal} \equiv \frac{\mid \Sigma(E_{clus} \cdot \cos\theta) \mid}{\Sigma E_{clus}} < 0.65,$$

  where θ is the polar angle of the cluster.

This event classification is useful to select the multihadron event with a high efficiency, rejecting the undesirable events such as cosmic or noise events. This is used in the event selection of $W^+W^- \rightarrow q\bar{q}'q''\bar{q}'''$ and $W^+W^- \rightarrow q\bar{q}'\ell\bar{\nu}_\ell$.

Chapter 5

Analysis of 161 GeV Data

The cross-section of the process $e^+e^- \rightarrow W^+W^-$ increases rapidly as the centre-of-mass energies, $\sqrt{s}$, near the nominal W^+W^- production threshold of $\sqrt{s} = 2\ M_W$. In other words, the cross-section at a given $\sqrt{s}$ is sensitive to the W boson mass. Therefore it is possible to determine M_W by measuring the cross-section and comparing it with theoretical predictions as a function of M_W in the context of the Standard Model. The measurement is complementary to those at $p\bar{p}$ colliders and to those which is performed at higher centre-of-mass energies at LEP2, where M_W is directly reconstructed from the decay products.

To identify W^+W^- production events in all possible decay topologies, a set of event selections are used. The criteria are required to strictly isolate the signal events, as the cross-sections for W^+W^- production and dominant background process $Z^0/\gamma \rightarrow f\bar{f}$, where f is any charged fermion, are quite different in magnitude; 3 pb and 200 pb, respectively. Additional backgrounds arise from processes with four-fermion final states which do not contain two resonant W bosons. These four-fermion backgrounds fall into two classes; those which interfere with the four-fermion states from W^+W^- production, and those which do not. The interfering four-fermion backgrounds are particularly problematic because they may also depend on the W mass. The mass-dependent four-fermion background is taken into account in the determination of the W mass. To this purpose, we applied a set of selections to Monte Carlo samples based on a complete calculation of the four-fermion processes, in which the interference effects are fully included. The results of "accepted" cross-section with the different M_W are analysed to determine the W mass.

This analysis uses the data recorded during the LEP2 run in 1996 at 161 GeV by the OPAL detector. The basic luminosity measurement and the beam energy measurement have been described in Section 3.1. The integrated luminosity is $9.890 \pm 0.042(\text{stat.}) \pm 0.040(\text{syst.})$ pb^{-1}. The luminosity weighted mean centre-of-mass energy for the data sample is $\sqrt{s} = 161.3 \pm 0.05$ GeV. For systematic checks of the analysis, sample of real data and Monte Carlo at different centre-of-mass energies are also used: the events at $\sqrt{s} = 133$ GeV and high statistics samples at $\sqrt{s} = 91$ GeV. A variety of Monte Carlo events are used to estimate efficiencies and backgrounds.

5.1 Selection of W^+W^- Events

Event selections are optimised for individual decay channel of the W pairs; $q\bar{q}'q''\bar{q}'''$, $q\bar{q}'e\bar{\nu}_e$, $q\bar{q}'\mu\bar{\nu}_\mu$, $q\bar{q}'\tau\bar{\nu}_\tau$, and $\ell^-\bar{\nu}_\ell\ell'^+\nu_{\ell'}$. The criteria used for each selection are described in Appendix B. This section presents the result of the selected W^+W^- events together with the systematic uncertainties of the selections.

5.1.1 $W^+W^- \rightarrow q\bar{q}'q''\bar{q}'''$ Events

Approximately 46% of the W pairs are expected to decay in the $q\bar{q}'q''\bar{q}'''$ channel, which is characterised by four energetic hadron jets. As the W boson has relatively low momentum near the threshold, a pair of jets from the W boson often appears back-to-back in the detector. The main backgrounds are the events from $Z^0/\gamma \rightarrow q\bar{q}$. They are particularly difficult to distinguish from the $W^+W^- \rightarrow q\bar{q}'q''\bar{q}'''$ events, especially when hard gluon emission take place.

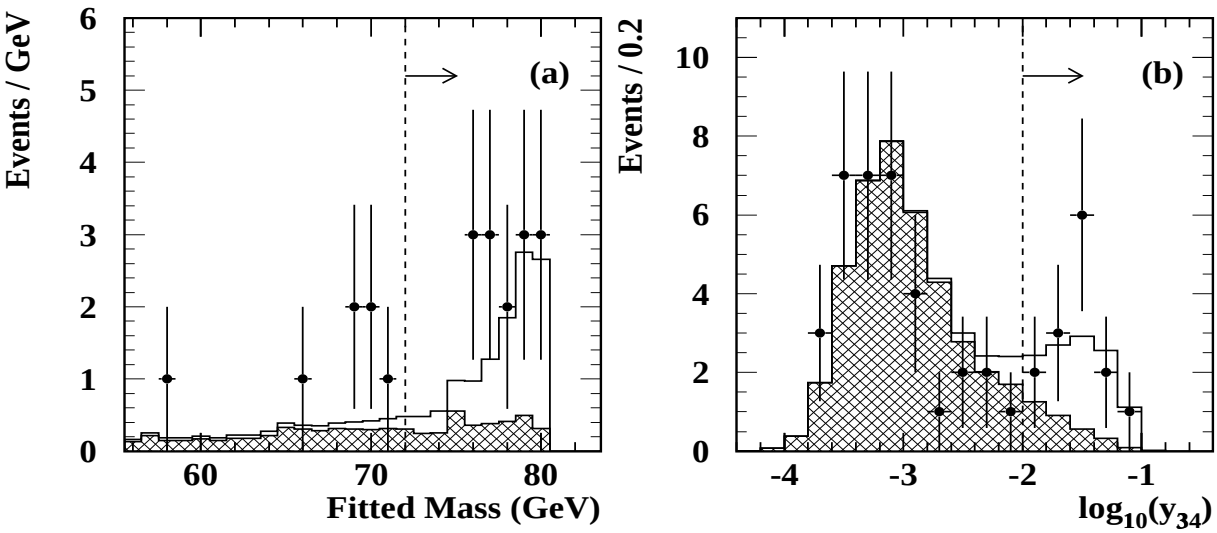

Figure 5.1: Illustration of the selection quantities together with Monte Carlo signal and background events: (a) the kinematically fitted mass and (b) $\log y_{34}$ for the $W^+W^- \rightarrow q\bar{q}'q''\bar{q}'''$ channel. The pairing of jets chosen for plot (a) is the one with the largest fitted mass with a fit χ^2 probability greater than 1%. Cuts are indicated with a vertical line and an arrow pointing in the direction of selected events. Each distribution is shown after all other selection requirements have been applied. The hatched histogram shows the expected distribution of the backgrounds and the open histogram is the sum of the expected signal and the backgrounds. The data are indicated by points.

The selection is mainly based on a jet finding algorithm and a kinematic fit. We use the "Durham" jet finding algorithm, and the value y_{34}, which is the jet resolution parameter for the three- to four-jet transition, is used for the selection. The kinematic fit imposes the energy-momentum conservation and the equality of the masses of two jet pairs. Distributions of the kinematically fitted mass and the y_{34} variable are shown in Figures 5.1 (a) and (b) for the

data and the Monte Carlo, after all other cuts. The number of candidate events and the corresponding Monte Carlo expectations for the signal and background events are given in Table 5.1. The background is dominated by the $Z^0/\gamma \rightarrow q\bar{q}$ events. The selection efficiency for the CC03 $W^+W^- \rightarrow q\bar{q}'q''\bar{q}'''$ events is estimated to be $(56.7 \pm 0.5)\%$.

Selection	Expected signal	Expected background	Observed
$W^+W^- \rightarrow q\bar{q}'q''\bar{q}'''$	9.6 ± 1.0	3.44 ± 0.39	14
$W^+W^- \rightarrow q\bar{q}'e\bar{\nu}_e$	3.89 ± 0.44	0.18 ± 0.27	3
$W^+W^- \rightarrow q\bar{q}'\mu\bar{\nu}_\mu$	4.19 ± 0.46	0.27 ± 0.15	2
$W^+W^- \rightarrow q\bar{q}'\tau\bar{\nu}_\tau$	2.32 ± 0.28	0.96 ± 0.34	7
$W^+W^- \rightarrow \ell^-\bar{\nu}_\ell\ell'^+\nu_{\ell'}$	2.58 ± 0.28	$0.19^{+0.12}_{-0.04}$	2
Combined	22.6 ± 2.4	5.0 ± 0.6	28

Table 5.1: Observed number of candidate events in each W^+W^- decay channel for an integrated luminosity of 9.89 ± 0.06 pb^{-1} at 161.3 ± 0.05 GeV, together with the expected numbers of signal and background with $M_W = 80.33 \pm 0.15$ GeV. The predicted numbers for signal include systematic uncertainties from the efficiency, the luminosity, the beam energy and the M_W value, while the background estimate includes selection and luminosity uncertainties.

A systematic uncertainty of 0.5% in the selection efficiency is estimated by comparing simulated W^+W^- events with a variety of models [19, 20, 22, 21], and by varying the fragmentation parameters within PYTHIA. The relative systematic uncertainty of 11.3% for backgrounds is estimated by comparing different Monte Carlo models [20, 22, 23], by comparing high statistics LEP1 data with that simulated by JETSET [20], and by varying the fragmentation model within PYTHIA. Background estimation is also checked using the data at $\sqrt{s} = 133$ GeV where the contribution from W^+W^- is negligible. A consistent result is obtained. The systematic uncertainties of both the selection efficiency and the background cross-section include a contribution from finite Monte Carlo statistics.

5.1.2 $W^+W^- \rightarrow q\bar{q}'e\bar{\nu}_e$ and $q\bar{q}'\mu\bar{\nu}_\mu$ Events

Approximately 29% of W pairs are expected to decay in the $q\bar{q}'e\bar{\nu}_e$ and $q\bar{q}'\mu\bar{\nu}_\mu$ channels, which contain an energetic charged lepton (e or μ), two or more hadronic jets and missing momentum due to the unobserved neutrino. There is a substantial $Z^0/\gamma \rightarrow q\bar{q}$ background in which a hadron or an initial state photon is misidentified as a lepton. Four-fermion processes such as $Z^0e^+e^-$, $We\bar{\nu}_e$ and off-shell Z^0Z^0 production can lead to the final state with two hadronic jets and one lepton thus constituting another source of background.

The event selection consists of multiplicity cuts, identification of an energetic isolated lepton, and kinematic cuts on quantities derived from the visible energy and the missing momentum. The distributions of the total transverse momentum, $\sum p_T$, and the momentum of the selected lepton candidate are shown in Figures 5.2 (a) and (b). The number of candidate events and the corresponding Monte Carlo expectations for signal and background events are given in Table 5.1. In order to investigate the possible disagreement between the data and the Monte Carlo, samples of "mixed" events are constructed from $q\bar{q}$ and $\ell^+\ell^-$ events at $\sqrt{s} = 91$ GeV. This "mixed" sample of the $q\bar{q}$ events plus the half of $\ell^+\ell^-$ events emulate the $W^+W^- \rightarrow q\bar{q}'\ell\bar{\nu}_\ell$

processes. The selection efficiencies have been reduced by 2–3% according to the difference of the data and the Monte Carlo samples. In addition, the reduction according to the mis-modeling of final state radiation is also found to be $\sim 1\%$. After these corrections the efficiencies for the $q\bar{q}'e\bar{\nu}_e$ and $q\bar{q}'\mu\bar{\nu}_\mu$ selections are $(71.4 \pm 2.6)\%$ and $(76.9 \pm 2.5)\%$, respectively. The contribution from the $q\bar{q}'\tau\bar{\nu}_\tau$ channel is estimated to be about 3.3 % for the $q\bar{q}'e\bar{\nu}_e$ selection and 4.0 % for the $q\bar{q}'\mu\bar{\nu}_\mu$ selection. The background is dominated by $Z^0/\gamma \rightarrow q\bar{q}$ and four-fermion processes, where the latter contribution is estimated as the difference between the accepted cross-sections for full four-fermion and CC03 W^+W^- Monte Carlo samples.

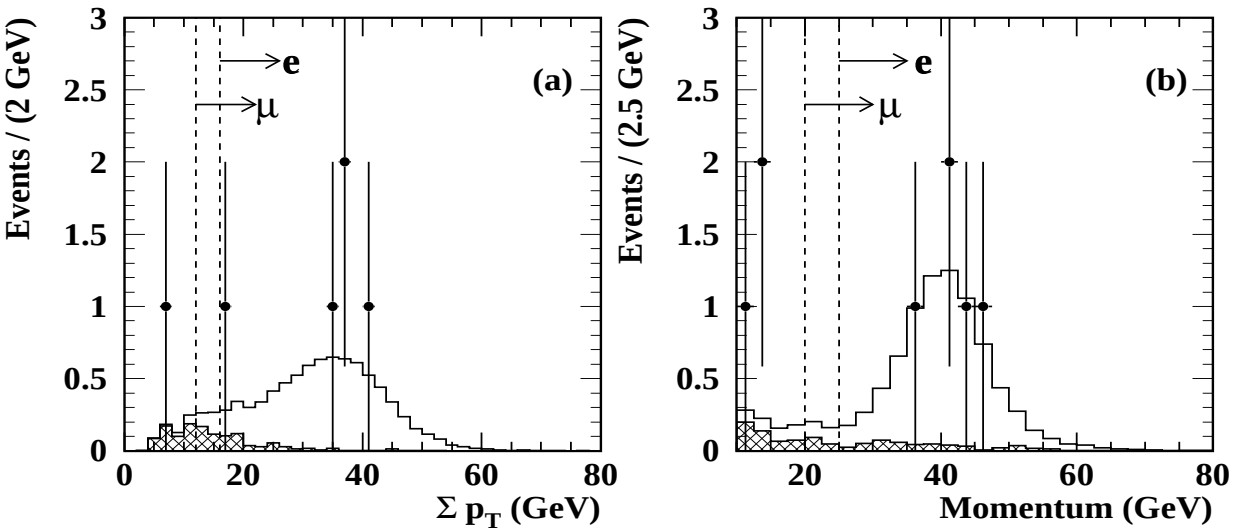

Figure 5.2: Illustration of the selection quantities: (a) $\sum p_T$ and (b) lepton momentum for the $W^+W^- \rightarrow q\bar{q}'e\bar{\nu}_e$, $q\bar{q}'\mu\bar{\nu}_\mu$ channels. Definitions of the symbols are the same as Figure 5.1.

The systematic uncertainty of approximately 2.5% in the selection efficiency in each channel includes contributions from comparisons of data and Monte Carlo using the samples of mixed events and W^+W^- events simulated using different models [18, 19, 20, 21]. The systematic uncertainties in the small accepted background cross-sections of four-fermion processes are estimated by comparing the grc4f and EXCALIBUR predictions. The corresponding uncertainties from $Z^0/\gamma \rightarrow q\bar{q}$ are obtained by comparing the predictions of different models [20, 22, 23], and by comparing high statistics LEP1 data with the Monte Carlo data simulated by JETSET. A consistent background estimate is obtained from the $\sqrt{s} = 133$ GeV data sample, as in the previous section. The systematic uncertainties of both the signal efficiency and the accepted background cross-section include a contribution from finite Monte Carlo statistics, particularly for the four-fermion processes.

5.1.3 $W^+W^- \rightarrow q\bar{q}'\tau\bar{\nu}_\tau$ Events

Approximately 14% of the W pairs are expected to decay in this mode, characterised by two or more hadronic jets, one τ decay jet and a missing momentum due to neutrinos. The background is dominated by $Z^0/\gamma \rightarrow q\bar{q}$ events, where the third jet originates from either an initial state photon observed in the detector, or a gluon emission. This analysis is also designed to select

the $W^+W^- \rightarrow q\bar{q}'e\bar{\nu}_e$ and $q\bar{q}'\mu\bar{\nu}_\mu$ events which do not pass the strict lepton identification requirements described above.

Distributions of $|\cos\theta_{\rm miss}|$ and $R_{\rm vis} \equiv E_{\rm vis}/\sqrt{s}$ are given in Figures 5.3 (a) and (b), where $\theta_{\rm miss}$ is the polar angle of the missing momentum and $E_{\rm vis}$ is the visible energy. The number of candidate events and the corresponding Monte Carlo expectations for signal and background events are given in Table 5.1. Considering all the selected $q\bar{q}'\tau\bar{\nu}_\tau$ events to be the signal leads to an efficiency of 42.5 ± 2.6 %, relative to the number of generated events from $W^+W^- \rightarrow q\bar{q}'\tau\bar{\nu}_\tau$. The dominant systematic effect in the background estimate is due to the simulation of the isolation parameter I (see Appendix B.3). It includes a correction of $(+15 \pm 9)\%$ evaluated by comparing the high statistics Z^0 data and the Monte Carlo. The mixture of W^+W^- decay modes in the selected events is expected to be $q\bar{q}'e\bar{\nu}_e$: $q\bar{q}'\mu\bar{\nu}_\mu$: $q\bar{q}'\tau\bar{\nu}_\tau$: $q\bar{q}'q''\bar{q}'''$ $\approx$ 1:1:8:0.05. If we exclusively remove the events selected by the other W^+W^- event selections, this selection attains an efficiency (relative to all $W^+W^- \rightarrow q\bar{q}'\tau\bar{\nu}_\tau$ decays) of about 40%.

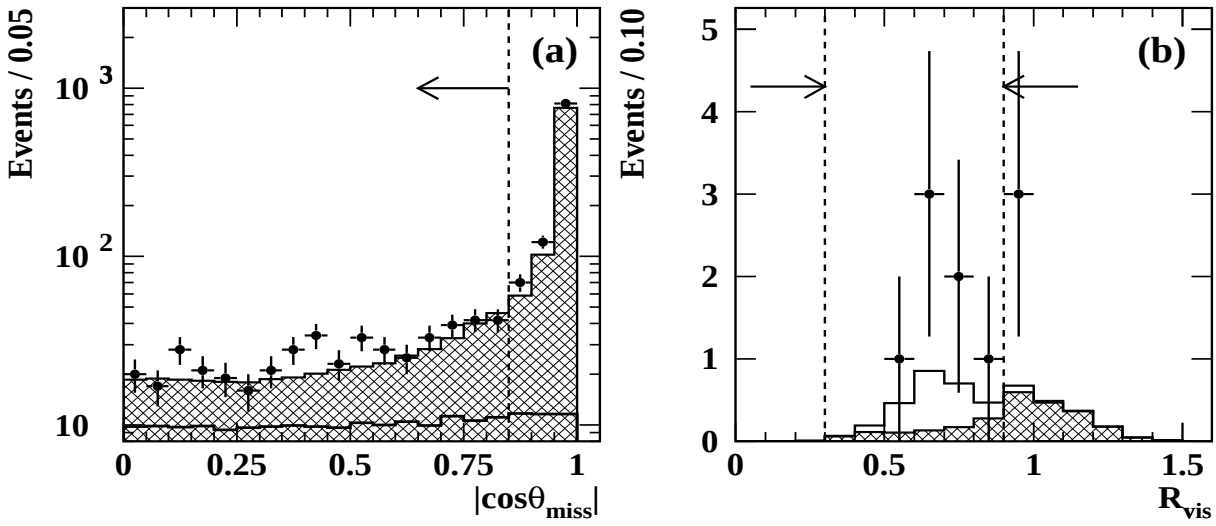

Figure 5.3: Illustration of the selection quantities: (a) $|\cos\theta_{\rm miss}|$ after multiplicity cuts only, and (b) $R_{\rm vis}$ after all other cuts in the $W^+W^- \rightarrow q\bar{q}'\tau\bar{\nu}_\tau$ channel. The symbols are as defined in Figure 5.1. In (a) the W^+W^- contribution is superimposed as a solid line and scaled up by a factor of 30.

The systematic uncertainty of 2.6% in the selection efficiency is estimated by comparing the data and Monte Carlo samples of the mixed events, and by comparing different Monte Carlo models [18, 19, 20, 21, 22]. The systematic uncertainties in the accepted background cross-section are estimated by comparing the predictions of different models [20, 22, 23], high statistics LEP1 data with those simulated by JETSET, the data and the Monte Carlo at $\sqrt{s} = 133$ GeV and background enriched samples at $\sqrt{s} = 161$ GeV. Systematic uncertainties in the four-fermion background are estimated using the grc4f and EXCALIBUR events. The finite Monte Carlo statistics also contributes to the systematic uncertainties.

5.1.4 $W^+W^- \rightarrow \ell^-\bar{\nu}_\ell\ell'^+\nu_{\ell'}$ Events

Approximately 11% of the W pairs may be observed as a pair of charged leptons or narrow tau jets with missing momentum. This analysis is sensitive to the six possible combinations of observed leptons, e^+e^-, $\mu^+\mu^-$, $\tau^+\tau^-$, $e^\pm\mu^\mp$, $e^\pm\tau^\mp$, $\mu^\pm\tau^\mp$, expected to be produced in the ratio 1:1:1:2:2:2. The main backgrounds are leptonic decays in $e^+e^- \rightarrow Z^0Z^0$, $e^+e^- \rightarrow Z^0e^+e^-$ and $e^+e^- \rightarrow We\bar{\nu}_e$ processes, and $e^+e^- \rightarrow \tau^+\tau^-$. The experimental signature depends on the number of stable leptons in the final state and the amount of background depends on whether the leptons are of the same flavor or not.

The distributions of $\phi_{\rm acop}$ vs. x_T and of x_T before applying the kinematic criteria are shown in Figures 5.4 (a) and (b), respectively. The parameter $\phi_{\rm acop}$ is the acoplanarity angle of the di-jet and the x_T is the transverse momentum of the event scaled by the beam energy. The other criteria are described in Appendix B.4. The number of candidate events (one $\mu^+\nu_\mu\mu^-\bar{\nu}_\mu$ and one $\mu^+\nu_\mu\ell^-\bar{\nu}_\ell$) and the corresponding Monte Carlo expectations for signal and background events are given in Table 5.1. The overall selection efficiency of the $W^+W^- \rightarrow \ell^-\bar{\nu}_\ell\ell'^+\nu_{\ell'}$ events is $(65.4 \pm 2.0)\%$. The efficiency and background estimates are corrected by a multiplicative factor of 0.959 ± 0.015 to account for effects in the data not modeled in the Monte Carlo, such as the detector occupancy due to off-momentum beam particles. A correction of -0.9% due to modeling of final state radiations is also included. The errors of the systematic uncertainty are estimated by the similar ways as the other event selections.

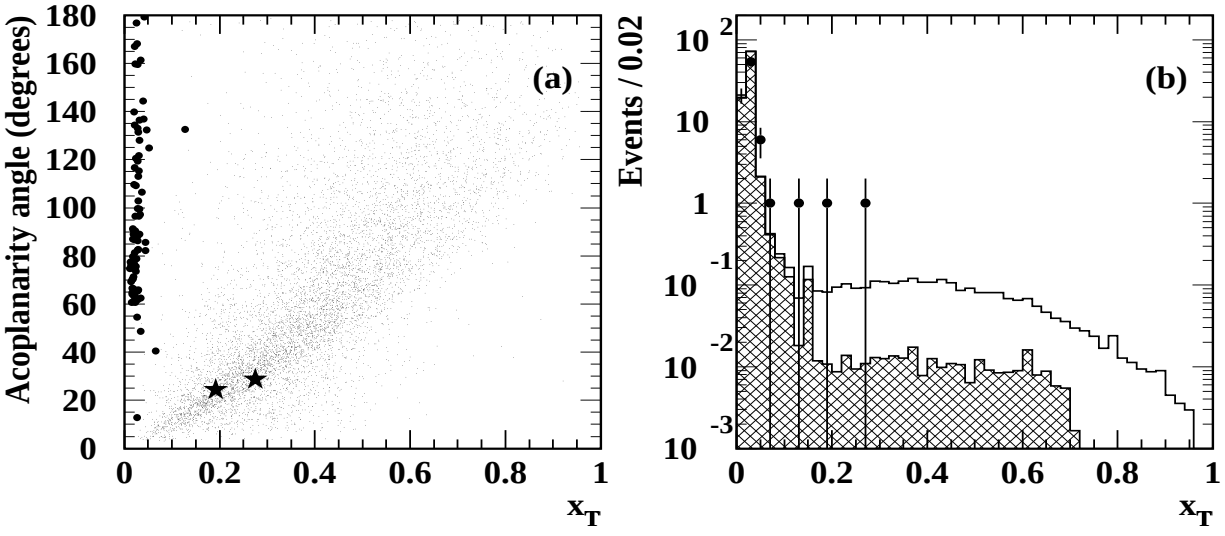

Figure 5.4: Illustration of the selection quantities. Plot (a) illustrates $\phi_{\rm acop}$ vs. x_T for selected di-jet events in the $W^+W^- \rightarrow \ell^-\bar{\nu}_\ell\ell'^+\nu_{\ell'}$ channel prior to applying the kinematic criteria. The large points are events in the data, the small points represent simulated W pair events. The two events accepted after all cuts are shown as stars. Plot (b) shows the projection of the x_T distribution, with symbols as defined in Figure 5.1.

5.2 Extraction of the W Mass from the W^+W^- Cross-section

It is recognised that the W-pair production must be treated as a part of four-fermion processes. In fact the four-fermion final states expected from the decay of a W-pair can also be produced from other diagrams. A complicated example is the $u\bar{u}d\bar{d}$ final state, which can be produced either from the decay of W-pair, or diagrams which involve a single virtual W, or via virtual Z^0/γ (see Figure 1.2). The latter two processes are regarded as background in view of the W^+W^- production and the contribution must be evaluated. In addition, the interference between these diagrams must also be considered. As a result the contributions of these diagrams are dependent on the W boson mass. Although the four-fermion interference effects are expected to be small at the current level of precision, the realistic effects should be estimated and included in the determination of the W mass.

In order to include the four-fermion interference effects, a set of the selections is applied to the Monte Carlo samples based on a compete calculation of the four-fermion processes. The "accepted" cross-section depending on the W mass has resulted in the expected number of events as a function of M_W. The M_W value is derived from a comparison between the number of events for the real data and those for the Monte Carlo prediction. To asses the dependence on the W mass of the accepted cross-section, a large number of event samples with different values of M_W are generated by the grc4f [18] Monte Carlo generator, where contributions of full diagrams are completely taken in account. This method also inherently takes account of the W boson mass dependence of the experimental selection cuts.

Figure 5.5 shows the ratio of the number of events accepted by the W^+W^- selections to the generated number of events for each channel using the grc4f Monte Carlo samples. These plots indicates the M_W dependence of the experimental selection cuts. For the $q\bar{q}'\mu\bar{\nu}_\mu$ and $q\bar{q}'\tau\bar{\nu}_\tau$ to which the W^+W^- production dominantly contributes, the ratios are almost constant. As against, for the $q\bar{q}'q''\bar{q}'''$, $q\bar{q}'e\bar{\nu}_e$, and $\ell^-\bar{\nu}_\ell\ell'^+\nu_{\ell'}$ channels, which have non-negligible contributions from other processes, the M_W dependence is seen in the plots. In these channels the ratios decrease as the M_W increases, because the fractions of the W^+W^- production in the generated events are reduced.

The Monte Calro predictions of the cross-section accepted by the W^+W^- selections are shown in Figure 5.6. The contributions from the other channels are included in each plot. Events are simulated at seven different values of M_W for all processes which give the same four-fermion states as the W^+W^- production, *i.e.* $q\bar{q}'q''\bar{q}'''$, $q\bar{q}'e\bar{\nu}_e$, $q\bar{q}'\mu\bar{\nu}_\mu$, $q\bar{q}'\tau\bar{\nu}_\tau$, and $\ell^-\bar{\nu}_\ell\ell'^+\nu_{\ell'}$. The accepted cross-section of non-interfering background processes, which have negligible W mass dependence, are evaluated at a single M_W value using grc4f and other generators. For each W^+W^- decay channel, i, the accepted cross-section is predicted as a function of $M_W - E_{beam}$ and parameterised by a second order polynomial using these Monte Carlo samples, $\sigma_i^{acc} = \sigma_i^{acc}(M_W - E_{beam})$. The parameterisations are also shown in Figure 5.6.

To determine the M_W and its statistical uncertainty, the likelihood $\mathcal{L}$ is formed from the product of the Poisson probabilities of observing N_i events for a Monte Carlo prediction of $\mu_i(M_W - E_{beam})$ events:

$$\mathcal{L} = \prod_i \frac{\mu_i(M_W - E_{beam})^{N_i} e^{-\mu_i(M_W - E_{beam})}}{N_i!}.$$

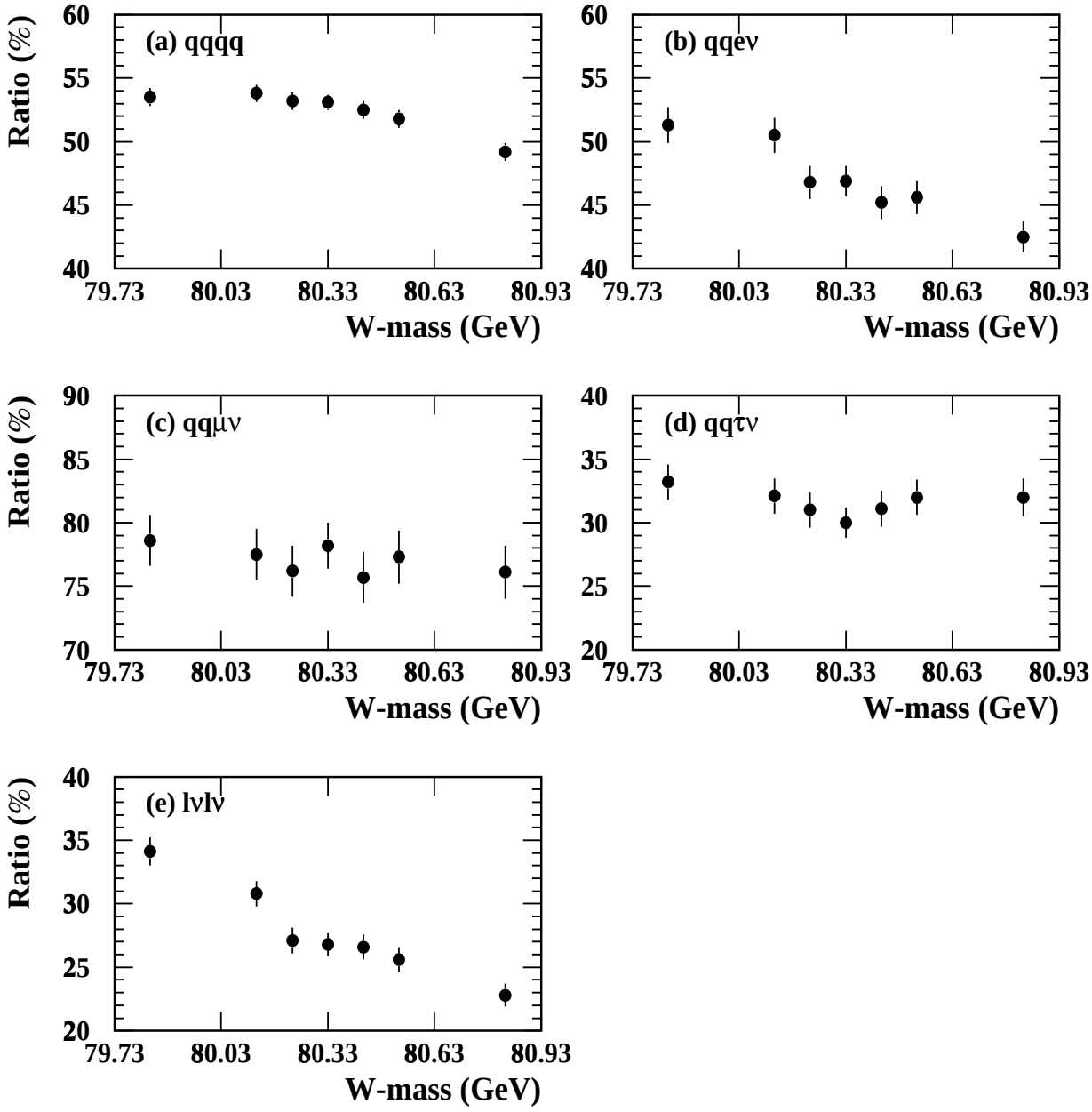

Figure 5.5: The ratios of accepted and generated numbers of events (in %) as a function of M_{W}. Plots (a)-(e) show the individual accepted events for $\mathrm{q\bar{q}'q''\bar{q}'''}$, $\mathrm{q\bar{q}'e\bar{\nu}_e}$, $\mathrm{q\bar{q}'\mu\bar{\nu}_\mu}$, $\mathrm{q\bar{q}'\tau\bar{\nu}_\tau}$, and $\ell^-\bar{\nu}_\ell\ell'^+\nu_{\ell'}$ final states, respectively.

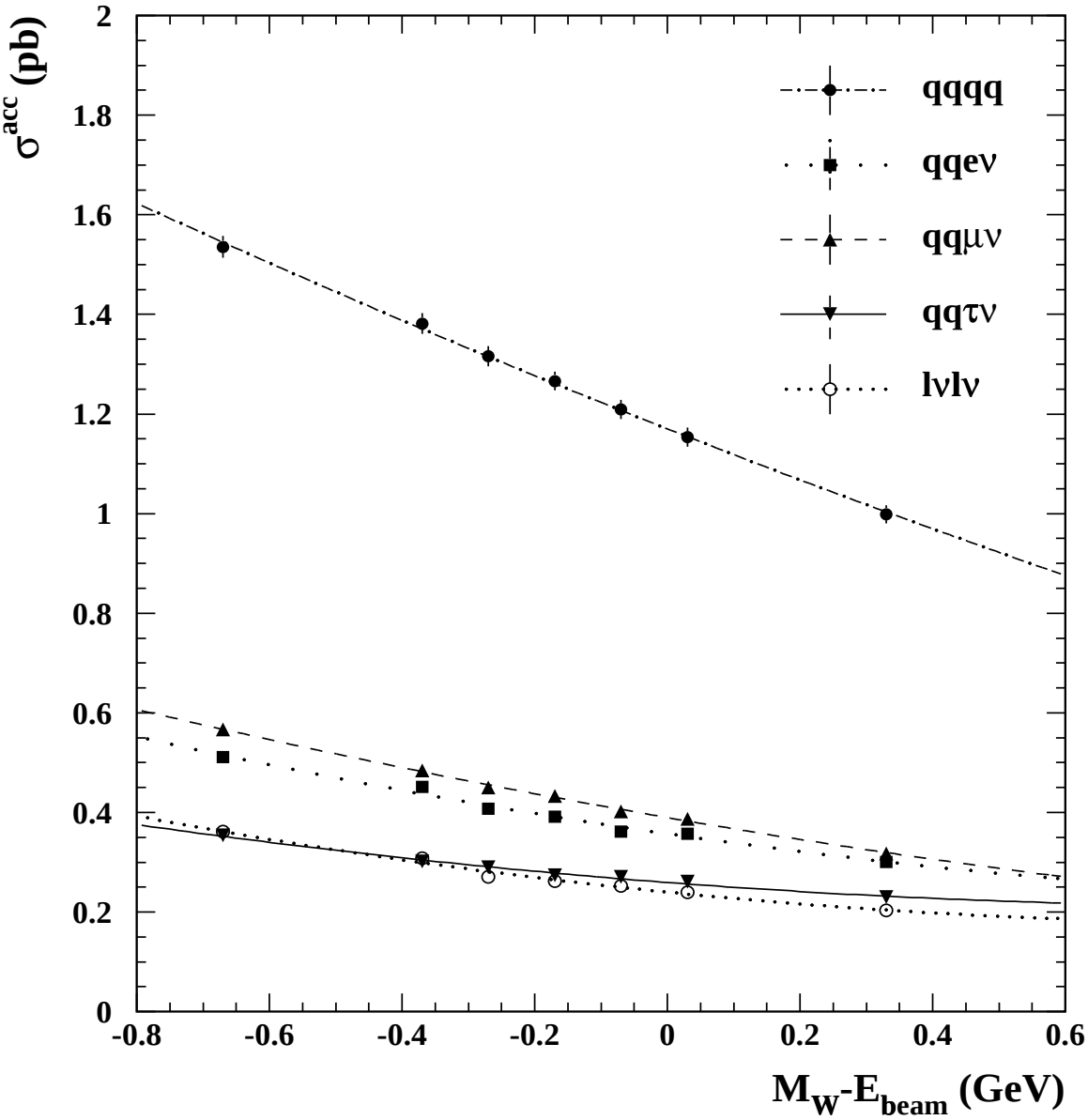

Figure 5.6: The accepted cross-sections in each W^+W^- decay channel are illustrated as a function of $M_W - E_{beam}$. In each case, the variation is parametrised by a second order polynomial.

The Monte Carlo prediction is a direct function of $M_{\mathrm{W}} - E_{\mathrm{beam}}$, and is given by $\mu_i(M_{\mathrm{W}} - E_{\mathrm{beam}})$ = luminosity $\times\ \sigma_i^{\mathrm{acc}}(M_{\mathrm{W}} - E_{\mathrm{beam}})$. The observed numbers from the data for the five separate channels, N_i, are summarised in Table 5.1. A maximum likelihood fit is performed to extract the W mass, taking into account the corrections of the $\mathrm{q\bar{q}'}\ell\bar{\nu}_\ell$ and $\ell^-\bar{\nu}_\ell\ell'^+\nu_{\ell'}$ channels, associated with the differences between the data and Monte Carlo samples, described in the previous subsection 5.1. The correlations between the $\mathrm{q\bar{q}'}\ell\bar{\nu}_\ell$ channels are included in the fit. Because the contributions from the $\mathrm{q\bar{q}'e\bar{\nu}_e}$ and $\mathrm{q\bar{q}'}\mu\bar{\nu}_\mu$ channels are not negligible in the $\mathrm{q\bar{q}'}\tau\bar{\nu}_\tau$ channel, the corrections of the $\mathrm{q\bar{q}'e\bar{\nu}_e}$ and $\mathrm{q\bar{q}'}\mu\bar{\nu}_\mu$ channels effect the accepted cross-section for the $\mathrm{q\bar{q}'}\tau\bar{\nu}_\tau$ channel. Figure 5.7 (a) shows the log-likelihood as a function of the M_{W}. The horizontal line of -0.5 determines the 1-σ limit of the statistical uncertainty.

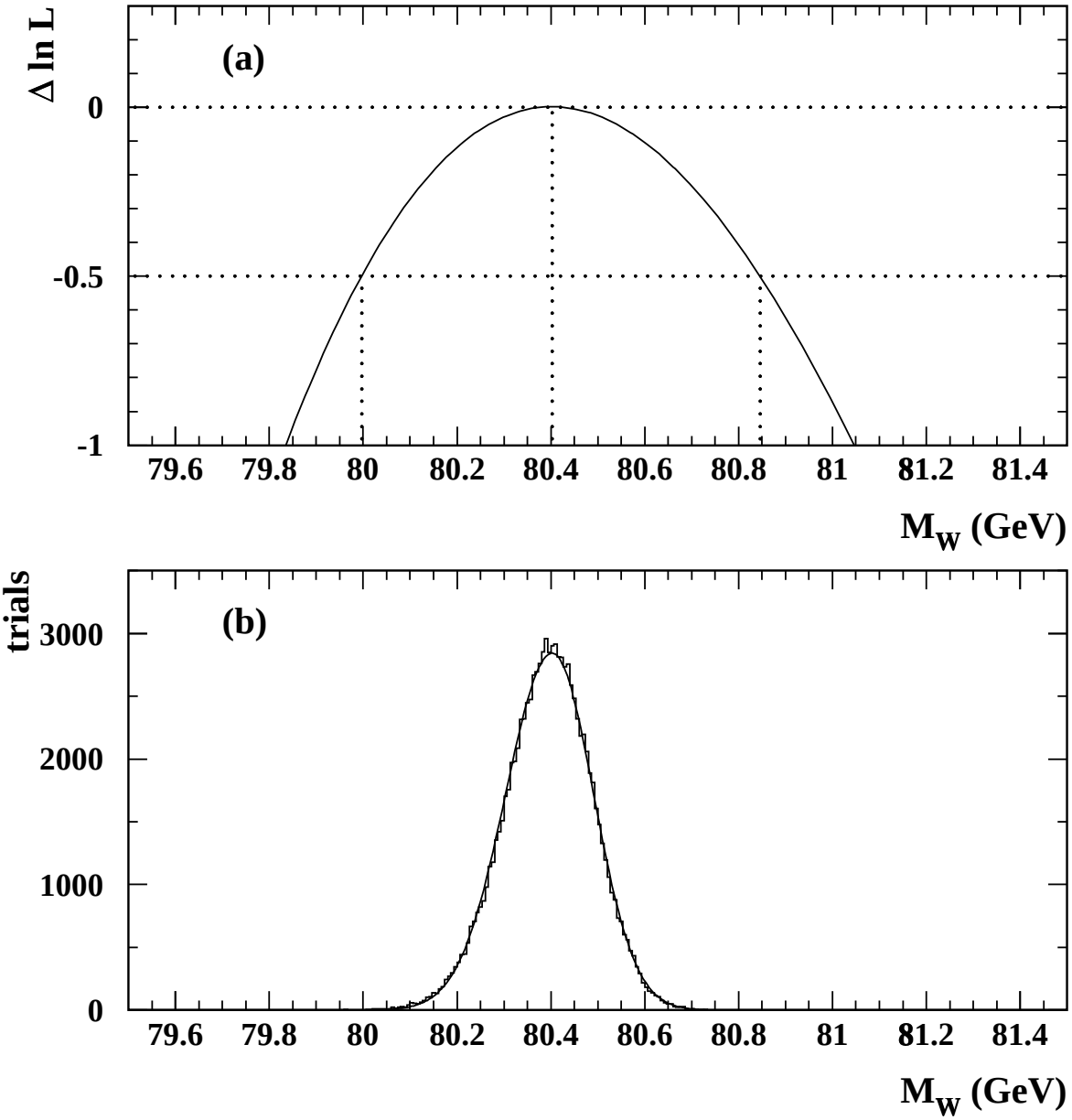

Figure 5.7: The likelihood function and the corresponding statistical uncertainty are shown in (a) for $\sqrt{s} = 161.3$ GeV. Plot (b) shows the distribution of M_{W} values evaluated using repeated Monte Carlo trials. Its width gives the systematic uncertainty.

5.3 Systematics Errors

The systematic uncertainties of the accepted cross-section for each channel are evaluated by the similar tests as described in the event selections. Although the treatment of the signal is different, *i.e.* taking the interfering four-fermion final states as the signal instead of the CC03 W^+W^- final states, the size of the total systematic uncertainty does not change in any channel. In these tests the comparisons of the signal Monte Carlo models are studied with the full sets of the grc4f and EXCALIBUR samples. These comparisons are performed not only at the generated $M_W = 80.33$ GeV but also at the different values of $M_W = 80.33 \pm 0.5$ GeV.

The systematic uncertainty on the derived M_W is obtained by means of repeated Monte Carlo trials. For each trial the expected number of events in each channel, $\mu_i(M_W - E_{beam}) =$ luminosity $\times \sigma_i^{acc}(M_W - E_{beam})$, is smeared according to the Gaussian uncertainties on the luminosity and the accepted cross-section. The corresponding M_W value is then re-evaluated. This procedure also takes into account the correlations between the $q\bar{q}'\ell\bar{\nu}_\ell$ channels. Figure 5.7 (b) shows the distribution of the M_W from the trials. The asymmetric Gaussian fit is performed to this distribution and the 1-σ spread is taken as the systematic uncertainty.

The beam energy uncertainty is directly taken as a systematic error, since the expected number of events is a function of the $M_W - E_{beam}$. The use of a function of $(M_W - E_{beam})$ is verified by generating the PYTHIA Monte Carlo samples with different centre-of-mass energies, $\sqrt{s}$ =160.0, 161.0, and 162.0 GeV.

In order to check any biases in the mass determination procedure, the two possible alternatives are further studied. First, the likelihood is formed without separating the channels. Second a, simple exponential function, $Ae^{B(M_W - E_{beam})} + C$, is used for the parameterisation of the accepted cross-section, instead of the second order polynomial. In each case, the obtained centre values of M_W are in good agreement. The size of the statistical and the systematic errors are also similar to those of the main analysis.

5.4 Results of 161 GeV Analysis

With the analysis where the interference in the four-fermion final states is taken into account, the selected 28 events determine the W mass to be

$$M_W = 80.40^{+0.44+0.09}_{-0.41-0.10} \pm 0.03\text{GeV}.$$

The first and second uncertainties are statistical and systematic respectively, and the third one is from the beam energy uncertainty.

The W mass can also be determined from the measurement of the CC03 W^+W^- production cross-section, neglecting the W mass dependent effects of the experimental selection cuts and absorbing the interference into a mass independent background. Since these effects are expected to be small, it is a good approximation at the current level of the statistical precision. Uncertainties associated with these effects evaluated from the comparison of several Monte Carlo samples are taken as systematic errors. A likelihood function is constructed from the Poisson probabilities, where the Monte Carlo prediction of $\mu_i(\sigma_{WW})$ events is now obtained by the calculation of the estimated efficiencies for signals and backgrounds. Maximising the

likelihood function yields the CC03 cross-section to be, $\sigma_{\mathrm{WW}} = 3.62\ ^{+0.93}_{-0.82} \pm 0.16$ pb, where the first uncertainty is statistical and the second is systematic.

To derive the dependence of the cross-section σ_{WW} on M_{W}, the semi-analytic programme GENTLE is used. The dependence of the $\mathrm{W^+W^-}$ cross-section on M_{W} in the CC03 framework is shown in Figure 5.8. The W mass is measured to be $M_{\mathrm{W}} = 80.40 \pm 0.43 \pm 0.09 \pm 0.03$ GeV, where the first error is statistical and the second is systematic, including all uncertainties in the cross-section measurement and in the σ_{WW} cross-section predicted by different programmes. The third error arises from the beam energy uncertainty. This measurement of M_{W} agrees with the value determined by the full four-fermion analysis, as illustrated in Figure 5.8.

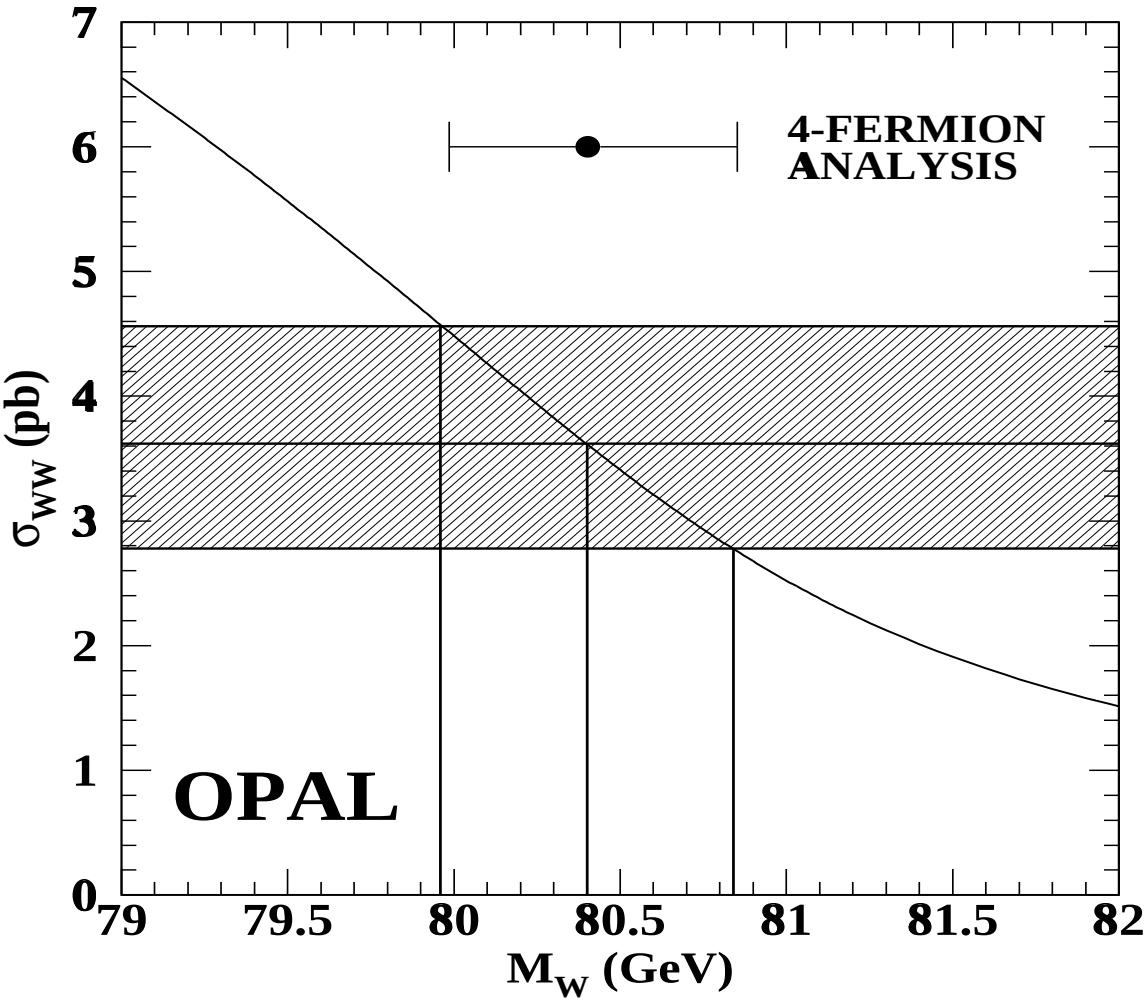

Figure 5.8: σ_{WW} as a function of M_{W}, as predicted by GENTLE for $\sqrt{s} = 161.3$ GeV. The measured $\mathrm{W^+W^-}$ cross-section is shown by a shaded band and the corresponding W boson mass by vertical lines. The principal measurement of M_{W} in this thesis is shown as a point with error bars. The uncertainties include statistical and systematic contributions, but do not include the effect of the beam energy uncertainty.

Chapter 6

Analysis of 172 GeV Data

As discussed in Section 1.2, at centre-of-mass energies well above the W^+W^- production threshold, we measure the W boson mass by the direct reconstruction of the invariant mass of the W decay products. This method is quite different from the measurement at the threshold, and is expected to have a higher statistical power.

The analysis of the direct reconstruction consists of four parts; selection of the W^+W^- events, reconstruction of the invariant mass of the W decay products, determination of the W mass, and estimation of systematic errors.

In this analysis the signal events ($W^+W^- \rightarrow q\bar{q}'q''\bar{q}'''$, $q\bar{q}'\ell\bar{\nu}_\ell$) have to be selected efficiently and with good purity. Compared to the 161 GeV data, the ratio of the cross-section of the W^+W^- production to the dominant background process Z^0/γ is slightly larger but still less than 0.1. A relative likelihood is used to separate the signal and background in each selection.

For a selected event, the masses of the two W bosons can be determined from measured invariant masses of the decay products. In order to further improve the mass resolution a kinematic fit is employed to the $q\bar{q}'e\bar{\nu}_e$, $q\bar{q}'\mu\bar{\nu}_\mu$, and $q\bar{q}'q''\bar{q}'''$ events. For the kinematic fit to work correctly, it is necessary that the measured quantities are unbiased and the error estimates are adequate. Section 6.2 discusses the biases of the measured quantities, the estimation of the error matrix, and results on the reconstructed mass distributions for each channel. The fully leptonic final state, $W^+W^- \rightarrow \ell^-\bar{\nu}_\ell\ell'^+\nu_{\ell'}$ is underconstrained as it contains at least two unmeasured neutrinos. Therefore this channel is not used here.

The reconstructed mass spectrum, however, has systematic shifts due to initial state radiations (ISR), the detector resolution, and the event selection. For example, under the constraint of the energy conservation the ISR effect pushes up the mass distribution. To calibrate these effects on the reconstructed mass spectrum, a large number of Monte Carlo samples are used. Two different methods are used to fit the reconstructed mass distribution. In the first, M_W is determined by performing a binned likelihood fit, comparing the mass spectra from the data and the Monte Carlo. This method is free of bias as long as these effects are simulated correctly. In the second method, a simple curve fit is applied to the data. Monte Carlo events are utilized to correct the fit result for the biases.

Previous studies [6] of the physics potential of LEP2 indicated that the statistical error would be dominant with the current luminosity of about 10 pb^{-1}. To estimate the total systematic error, a number of systematic uncertainties of theoretical and experimental sources

are considered. As expected, the total systematic error is found to be sufficiently small compared to the statistical error. Studies of systematic errors are described in section 6.4.

The data sample of 10.363 ± 0.045(stat.) $\pm$ 0.036(syst.) pb^{-1}, of which approximately 1.0 pb^{-1} was collected at $\sqrt{s} = 170.3$ GeV and 9.3 pb^{-1} at $\sqrt{s} = 172.3$ GeV, is used in this analysis. The luminosity weighted mean centre-of-mass energy for the data sample is $\sqrt{s} = 172.12 \pm 0.06$ GeV.

6.1 Selection of the W^+W^- Events

Event selections have been developed to identify the Standard Model W^+W^- final states of $q\bar{q}'\ell\bar{\nu}_\ell$ and $q\bar{q}'q''\bar{q}'''$. In the semi-leptonic case, selections are separated into the individual lepton type, $q\bar{q}'e\bar{\nu}_e$, $q\bar{q}'\mu\bar{\nu}_\mu$, and $q\bar{q}'\tau\bar{\nu}_\tau$. The $q\bar{q}'\tau\bar{\nu}_\tau$ selections are applied only to the events which failed in the $q\bar{q}'e\bar{\nu}_e$ and $q\bar{q}'\mu\bar{\nu}_\mu$ selections. No attempt has been made to identify the flavor composition of the hadronic final states. For each selection a relative likelihood is used to separate the signal events from the backgrounds. To categorise the lepton types of the final states, relative likelihoods are additionally used for $q\bar{q}'\ell\bar{\nu}_\ell$ selections. The events which are selected by both $q\bar{q}'\ell\bar{\nu}_\ell$ and $q\bar{q}'q''\bar{q}'''$ selections are treated as the $q\bar{q}'\ell\bar{\nu}_\ell$ candidates because the semi-leptonic selection has a higher purity. The signal likelihood is estimated using the WW Monte Carlo samples which include only CC03 diagrams. For the background $q\bar{q}$ Monte Carlo samples are used. Because the selections should be unbiased to the W mass, a set of variables which are used to calculate likelihoods in the selections are chosen not to have strong correlation with the reconstructed mass distribution. A full description of the selection criteria is given in Appendix C. A brief result of the event selections is presented here.

6.1.1 $q\bar{q}'q''\bar{q}'''$ Selection

Figure 6.1 shows the likelihood distributions of the $W^+W^- \rightarrow q\bar{q}'q''\bar{q}'''$ selection after preselection cuts. The preselection removes events which are likely to be from the process $Z^0 \rightarrow q\bar{q}$. The relative likelihood for an event is estimated using seven kinematic variables. A cut of likelihood > 0.2 is used for the measurement of the mass. The efficiency of the $W^+W^- \rightarrow q\bar{q}'q''\bar{q}'''$ selection is estimated to be $(79.8 \pm 0.2 \pm 1.2)\%$, where the errors are statistical and systematic respectively. The observed numbers of candidate events of this channel are found in Table 6.1. Those after the preselection cut and the likelihood cut are consistent with the expectations.

6.1.2 $q\bar{q}'\ell\bar{\nu}_\ell$ Selection

Figure 6.2 shows the likelihood distributions of the $W^+W^- \rightarrow q\bar{q}'e\bar{\nu}_e$ and $W^+W^- \rightarrow q\bar{q}'\mu\bar{\nu}_\mu$ selection for events passing preselection cuts, respectively. The contribution from $W^+W^- \rightarrow q\bar{q}'\tau\bar{\nu}_\tau$ decays is shown by the single hatched histogram and the contribution from background processes by the doubly hatched histogram. The peaks in the background distributions near one arise predominantly from four-fermion background. Events having relative likelihood value greater than 0.5 are selected. The $W^+W^- \rightarrow q\bar{q}'\tau\bar{\nu}_\tau$ selection consists of four relative likelihoods corresponding to the tau decay classes; electron, muon, hadronic one prong, and hadronic three prong. Events with a relative likelihood greater than 0.75 for any one of the tau likelihoods is selected as the $W^+W^- \rightarrow q\bar{q}'\tau\bar{\nu}_\tau$ candidates.

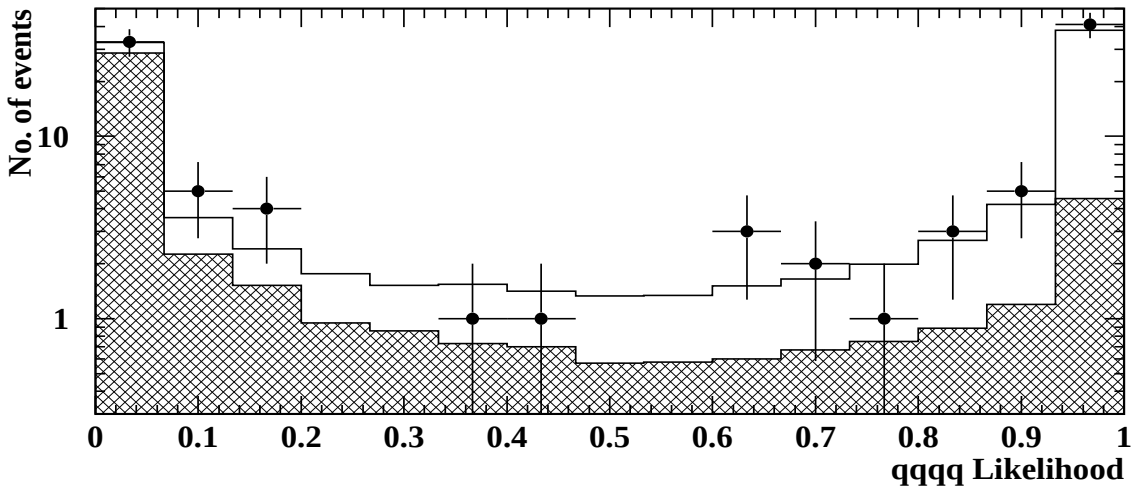

Figure 6.1: The likelihood distributions of the $W^+W^- \rightarrow q\bar{q}'q''\bar{q}'''$ selection. The points indicate the data, the open histogram shows the $W^+W^- \rightarrow q\bar{q}'q''\bar{q}'''$ Monte Carlo and the hatched histogram shows the total background expectation.

Channels	Expected signal	Expected background	Total	Observed
$W^+W^- \rightarrow q\bar{q}'q''\bar{q}'''$				
Preselection	53.0 ± 1.5	46.7 ± 2.1	99.7 ± 2.6	99
Likelihood	46.8 ± 1.2	14.3 ± 2.9	61.0 ± 3.1	57
$W^+W^- \rightarrow q\bar{q}'e\bar{\nu}_e$	16.8 ± 0.4	1.2 ± 0.4	18.0 ± 0.6	19
$W^+W^- \rightarrow q\bar{q}'\mu\bar{\nu}_\mu$	17.4 ± 0.4	0.6 ± 0.1	17.9 ± 0.4	16
$W^+W^- \rightarrow q\bar{q}'\tau\bar{\nu}_\tau$	13.5 ± 0.4	2.7 ± 0.7	16.2 ± 0.8	20

Table 6.1: Observed numbers of candidate events in each W^+W^- decay channel for an integrated luminosity of 10.36 ± 0.06 pb^{-1} at 172.12 ± 0.06 GeV, together with expected numbers of signal and background events, assuming $M_W = 80.33 \pm 0.15$ GeV. The predicted numbers of signal events include systematic uncertainties from the efficiency, luminosity, beam energy, W^+W^- cross-section and M_W, while the background estimates include selection and luminosity uncertainties. The errors on the expected total numbers account for correlations.

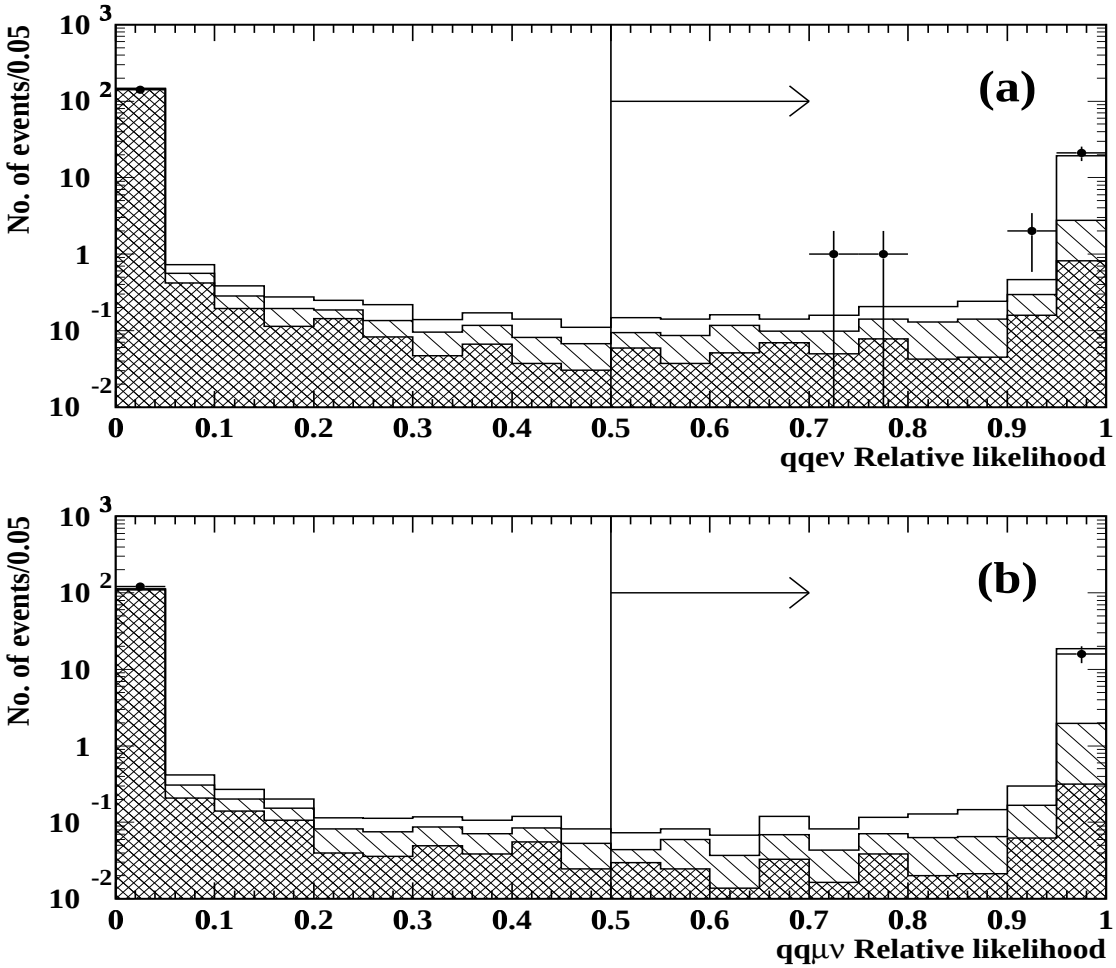

Figure 6.2: Relative likelihoods, $\mathcal{L}^{q\bar{q}'e\bar{\nu}_e}$ and $\mathcal{L}^{q\bar{q}'\mu\bar{\nu}_\mu}$ for (a) $W^+W^- \rightarrow q\bar{q}'e\bar{\nu}_e$ and (b) $W^+W^- \rightarrow q\bar{q}'\mu\bar{\nu}_\mu$. The data are shown by the points with error bars.

Table 6.2 shows the efficiencies of the selections for $W^+W^- \rightarrow q\bar{q}'\ell\bar{\nu}_\ell$ events after categorisation into the individual channel. These efficiencies, based on KORALW, include corrections which account for observed differences between the data and the Monte Carlo simulation. The uncertainties include both systematic and statistical contributions. The observed numbers of candidate events of this channel are also in Table 6.1.

	Generated as		
Selected as	$W^+W^- \rightarrow q\bar{q}'e\bar{\nu}_e$	$W^+W^- \rightarrow q\bar{q}'\mu\bar{\nu}_\mu$	$W^+W^- \rightarrow q\bar{q}'\tau\bar{\nu}_\tau$
$W^+W^- \rightarrow q\bar{q}'e\bar{\nu}_e$	$85.1 \pm 0.9\%$	$0.1 \pm 0.1\%$	$3.9 \pm 0.3\%$
$W^+W^- \rightarrow q\bar{q}'\mu\bar{\nu}_\mu$	$0.2 \pm 0.1\%$	$87.6 \pm 0.8\%$	$4.4 \pm 0.3\%$
$W^+W^- \rightarrow q\bar{q}'\tau\bar{\nu}_\tau$	$4.7 \pm 0.5\%$	$5.2 \pm 0.5\%$	$61.4 \pm 1.2\%$

Table 6.2: Selection efficiencies for the $W^+W^- \rightarrow q\bar{q}'\ell\bar{\nu}_\ell$ channels after event categorisation, showing the cross contamination among channels.

6.2 Invariant Mass Reconstruction

6.2.1 The $W^+W^- \to q\bar{q}'\ell\bar{\nu}_\ell$ Channel

For the selected $W^+W^- \to q\bar{q}'\ell\bar{\nu}_\ell$ event, the masses of the two W bosons can be determined by measured invariant masses of the decay products. Without imposing any constraints the reconstructed mass m_{rec} can be given by the invariant mass of the di-jet system:

$$m_{rec} = \sqrt{(E_{tot})^2 - (\vec{P}_{tot})^2},$$

where E_{tot} and $\vec{P}_{tot}$ are the total energy and momentum of the di-jet system. Figure 6.3 (a) shows the distribution of the reconstructed mass for the $M_W = 80.33$ GeV Monte Carlo sample. The mass resolution is roughly 10 %. In case of the $q\bar{q}'e\bar{\nu}_e$ and $q\bar{q}'\mu\bar{\nu}_\mu$ events, another m_{rec} can be also determined for the leptonic system when the unknown three-momentum of the neutrino is estimated with a help of momentum conservation. In order to improve the M_W resolution, the requirements are imposed on the energy-momentum conservation and on the mass-equality of the two W bosons. The total energy, or the centre-of-mass energy, is given in an e^+e^- collider with a good precision, a few ten MeV (see Section 3.1.2). The equality of the two M_W's is assumed by neglecting the finite W width event by event. In practice, the W width is small compared to the mass resolution.

The most effective way to use all the information available in an event is to perform a constrained kinematic fit. In this fit, the measured parameters are varied within a given error assuming the Gaussian distribution until the χ^2 is minimized. As the input measured parameters, the absolute momentum and two direction angles are taken for each of 4 particles. The error matrix of these 12 parameters are also fed to the kinematic fit, assuming that the correlations between the particles can be neglected. In the case of electron (muon), the cluster parameters reconstructed with the elctromagnetic calorimeter (the track parameters reconstructed with the central tracker) are used. For the reconstruction of the jet parameters, the GCE algorithm is used, which corrects the jet energy globally to avoid the double counting. The error matrix of the quark jet is estimated by using Monte Carlo samples. Each diagonal component is defined as a function of polar angle and energy of the jet. Off-diagonal components are set to be zero.

Figures 6.3 (b) and (c) show the distributions of the fit probability and the reconstructed mass spectrum, for the Monte Carlo events. The constraints in this fit are the energy-momentum conservation, and the mass-equality of the two W bosons. Therefore an event yields a single reconstructed mass. To remove poorly reconstructed events and reduce the background, the fit probability is required to be greater than 0.1 %. Two jets of the hadronic system are defined using the "Durham" jet-finding algorithm [30]. The measured mass of each jet is taken into account of the invariant mass calculation because it gives an improved mass resolution and yields a better agreement between the reconstructed mass and the generated mass in Monte Carlo studies. If the mass-equality constraint is not applied, the reconstructed masses of two W bosons are strongly anti-correlated. The average of the two M_W values has a slightly worse resolution than in the case of imposing the equality.

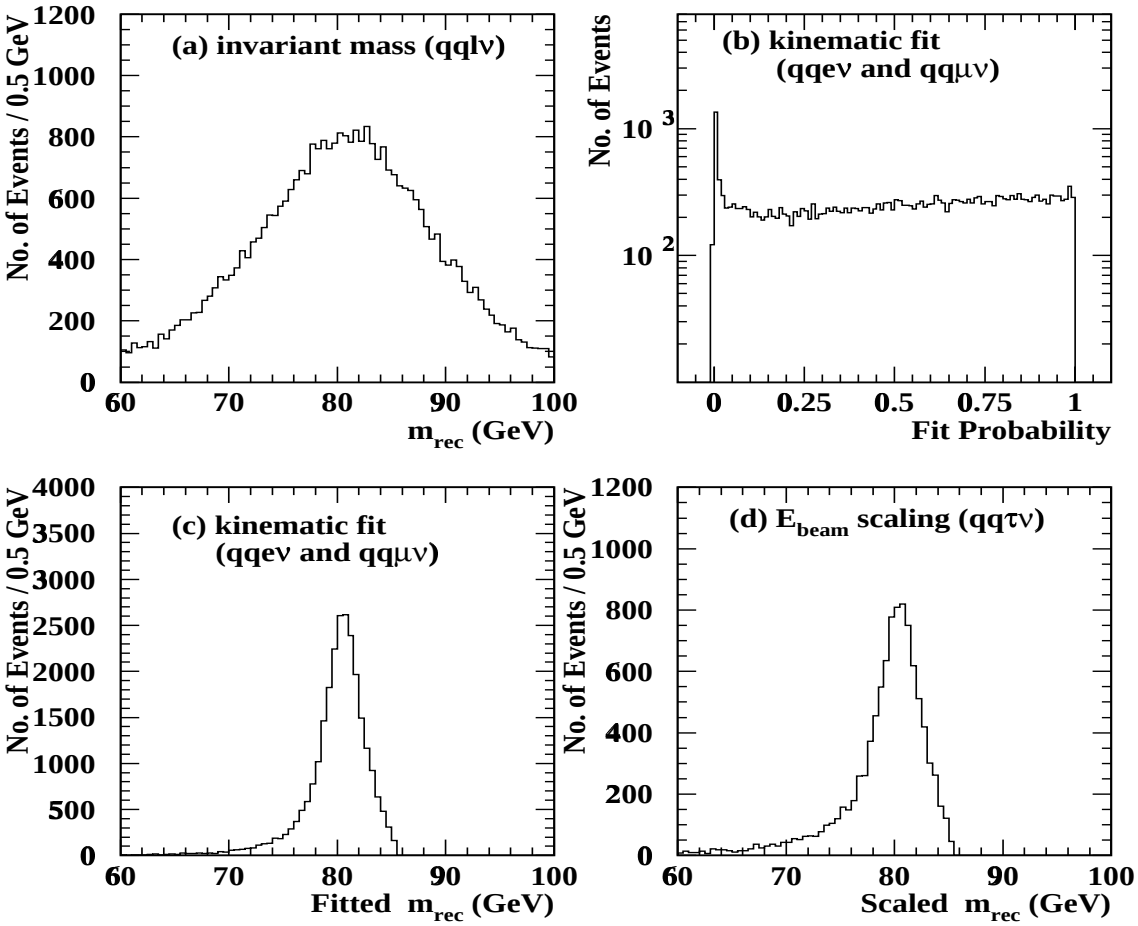

Figure 6.3: Illustrations of the reconstructed mass for the selected $W^+W^- \to q\bar{q}'\ell\bar{\nu}_\ell$ in the Monte Carlo sample: (a) without any constraint, (c) with constraints of energy-momentum conservation and the mass-equality of the two W bosons, and (d) the beam energy constraint for $q\bar{q}'\tau\bar{\nu}_\tau$ channel. Plot (b) shows the fit probability of the kinematic fit.

For the $W^+W^- \to q\bar{q}'\tau\bar{\nu}_\tau$ events, the visible energy of the tau decay products is often a poor estimate of the tau lepton energy because of the presence of neutrino in the tau decay. To account for the neutrinos two different methods are studied. First, only the hadronic system is used to reconstruct the W mass. Taking the beam energy constraint, the reconstructed mass is scaled as

$$m_{rec} = \frac{E_b}{E_{tot}}\sqrt{(E_{tot})^2 - (\vec{P}_{tot})^2},$$

where E_b is the beam energy. The beam energy constraint is exactly equivalent to the constraint that the masses of two W bosons are equal. Second, the direction of the tau lepton is taken as that of the measured tau jet in a kinematic fit. The energy of the tau lepton is set to half the beam energy with an error large enough to cover the kinematically allowed range. Monte Carlo studies show that the mass resolution of the fit is not significantly better than that obtained by the former method. Furthermore, the fit introduces more bias. Therefore the di-jet invariant mass with beam energy scaling is used to reconstruct the invariant mass for the $q\bar{q}'\tau\bar{\nu}_\tau$ channel. The mass spectrum for the Mote Carlo events is shown in Figure 6.3 (d).

6.2.2 The $W^+W^- \to q\bar{q}'q''\bar{q}'''$ Channel

In the $q\bar{q}'q''\bar{q}'''$ channel we do not know which jets are to be combined to produce the correct M_W. Three kinematic fits are performed for each event, corresponding to three possible jet-jet pairings, and are placed in a descending order of the resulting fit probabilities P_1, P_2, P_3. In Monte Carlo studies, the highest fit probability, P_1, corresponds to the correct jet-jet pairing in about 68% of the $q\bar{q}'q''\bar{q}'''$ events. In approximately 25% of events the second highest probability fit,P_2, corresponds to the correct combination. The lowest probability fit is dominated by incorrect combinations and is not used. Figure 6.4 (a) shows the distribution of the highest fit probability, P_1, for the selected $q\bar{q}'q''\bar{q}'''$ events of the Monte Carlo sample with $M_W = 80.33$ GeV. Figures 6.4 (b), (c), (d) show the reconstructed mass spectra with the highest, the second highest, and the lowest fit probability, respectively. The shaded histograms indicate the contribution of the wrong combination. The algorithms of jet-finding and jet energy reconstruction are the same as used in the $q\bar{q}'\ell\bar{\nu}_\ell$ channel. Constraints of energy-momentum conservation and equality of the two W masses are imposed to the kinematic fit. To reduce the higher background in the $q\bar{q}'q''\bar{q}'''$ channel, a tighter cut of the fit probability, $P_i > 1$ %, is applied.

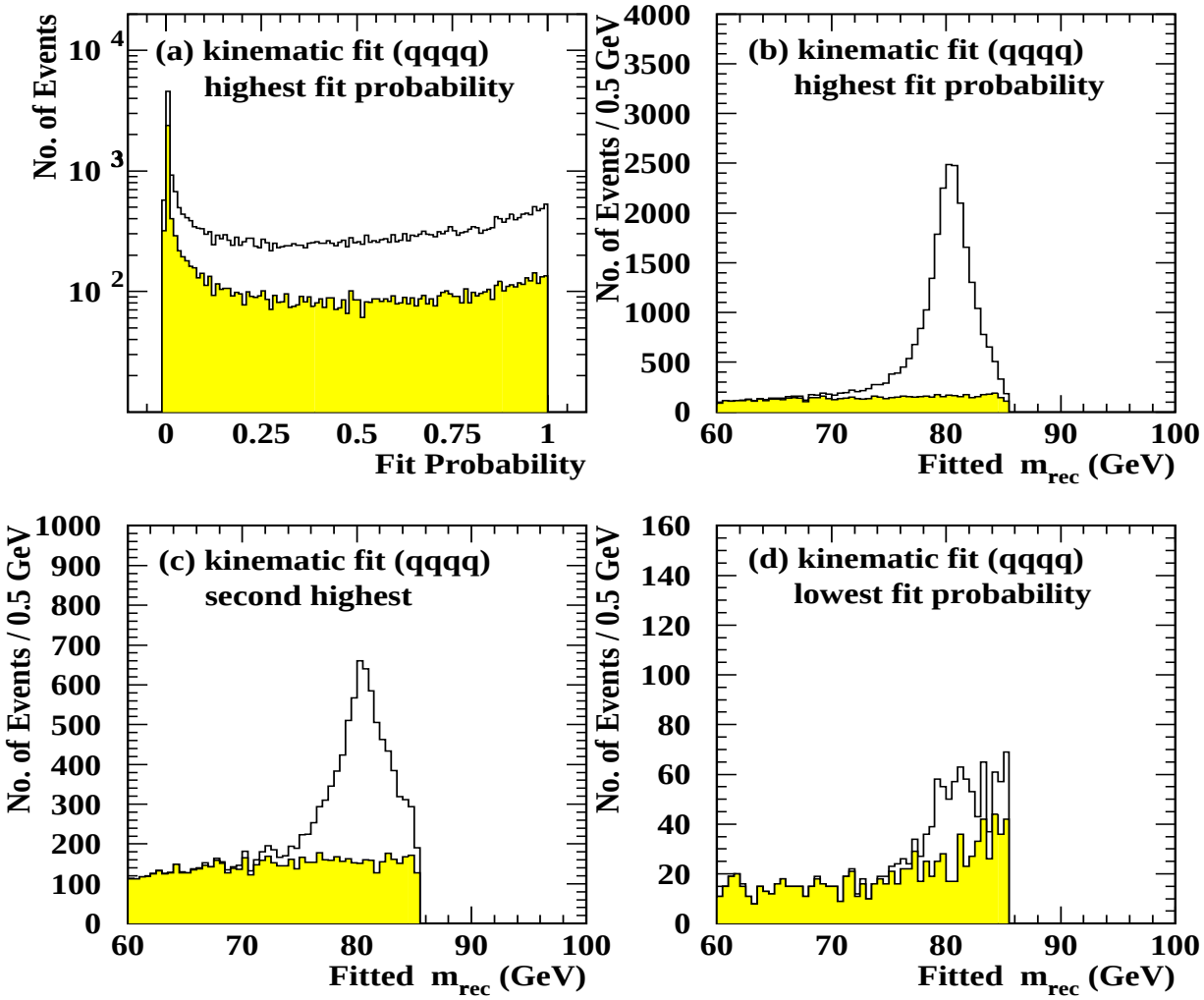

Figure 6.4: Distributions of the fit probability and the reconstructed mass spectra in different combinations for the $W^+W^- \to q\bar{q}'q''\bar{q}'''$ channel.

6.2.3 Test of the Kinematic Fit Procedure

For the kinematic fit to work properly, it is necessary that the measured input parameters are unbiased and their errors are adequately estimated. To this end, an alternative algorithm of the jet energy reconstruction is applied to the kinematic fit, which makes use of the matching method (MT) and a different parameterisation of the jet errors . Results with this alternative method is compared with the original ones.

Jet energy reconstruction:

The algorithm, GCE, sums up all the energies of tracks and clusters in a jet, and corrects the jet energy by using the estimation of a single charged particle response in the calorimeter. On the other hand, the MT corrects a cluster energy, if the cluster is identified as an overlap of a neutral particle and a charged particle. Therefore the GCE depends solely on the calorimeter information while the MT relies more on the track information. In general MT gives better resolution on the measurement of the jet direction, while the resolution of the jet energy is comparable for the two algorithms.

Input measured quantities:

As input parameters to the kinematic fit in an alternative method, $\log |p|$, polar angle θ, and azimuthal angle ϕ, of jets are adopted instead of $|p|$, $\cot\theta$, and ϕ used in the original method. Monte Carlo studies indicate that alternative set of parameters shows a better behavior.

Error matrix:

As against the original method of the error parameterisation, the alternative method is more complicated. The error function for the jet scalar momentum, $\Delta(\log |p|)$, is parameterised with $\cos\theta$ and jet momentum, P_j. The errors for the angles, $\Delta\theta$ and $\Delta\phi$, are parameterised with $\cos\theta$, jet energy, E_j, and jet mass, M_j. The $\cos\theta$ is represented as the detector configuration. Due to the particle escape in the beam pipe the errors are getting large at the $\cos\theta > 0.8$. To hold validity in wide range of the jet energy the errors are parameterised with P_j or E_j. The reason of using M_j is that it is expected to represent a broadness of the jet, which affect the angular resolution.

Correction of scalar momentum:

In the case of the jet direction close to the beam pipe, the scalar momentum is shifted to a lower value since some particles of the jet escape in the beam pipe region. To correct this shift, the $\log |p|$ is redefined as a function of $\cos\theta$. As the shift is seen to start at the $\cos\theta = 0.8$, the correction is performed only in the range of 0.8-1.0.

Results of the kinematic fits using the above alternative method with the MT and the different error matrix are shown in Figures 6.5 for the selected $W^+W^- \rightarrow q\bar{q}'e\bar{\nu}_e$ and $W^+W^- \rightarrow q\bar{q}'\mu\bar{\nu}_\mu$ Monte Carlo events. Plots (a) and (b) are the distributions of the fit probability and the reconstructed mass, respectively. Compared to the standard way of using the GCE, the mass resolution of the W boson is similar, while the mass peak is found to be shifted by several ten MeV. This mass shift is considered as an effect of the detector origin. However, it is not a problem because the distortion of the reconstructed mass spectrum, including the detector effect, is calibrated in the determination of the W mass. Results of both two methods after the calibration are in good agreement within an error of the Monte Carlo statistics. Therefore only the accuracy of this study is taken as a systematic uncertainty.

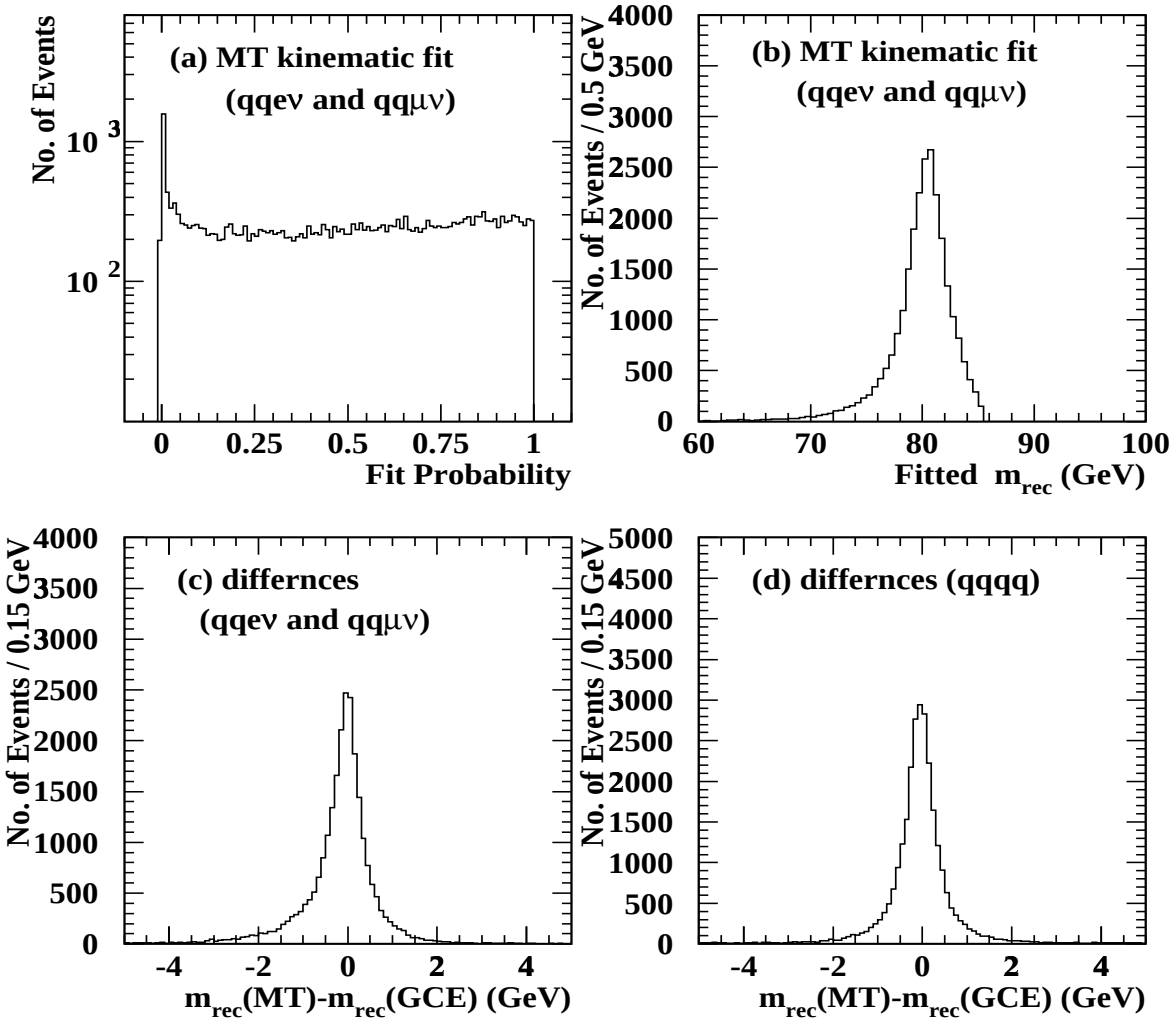

Figure 6.5: Results of the kinematic fits using the alternative way. Plots (c) and (d) show the differences in two methods.

The distribution of the event-by-event difference of the reconstructed masses are shown in Figures 6.5-(c) for $q\bar{q}'e\bar{\nu}_e$ and $q\bar{q}'\mu\bar{\nu}_\mu$ Monte Carlo events, and (d) for $q\bar{q}'q''\bar{q}'''$ channel. Asymmetry of the distributions comes from the different parameterisation of the error matrix, while the spread originates from the two alternative algorithms for the jet energy reconstruction. These differences are smaller than the detector resolution of the reconstructed invariant mass.

6.3 Determination of the W Mass

Biases introduced by the event selection, the detector resolution, the ISR and the phase-space affect to the reconstructed mass spectra. To measure the W mass with high precision their effects should be taken into account. The W boson mass is extracted by directly comparing the reconstructed mass distribution of the data to that estimated from the Monte Carlo samples with various values of M_W and Γ_W. A binned likelihood calculation gives the best description of the data for both M_W and Γ_W. In order to obtain the Monte Carlo spectrum for arbitrary values of M_W and Γ_W, a Monte Carlo reweighting technique is employed.

For a cross-check a simple curve fit is applied to the data, namely an unbinned likelihood

fit using an analytic function of the reconstructed mass spectra. The biases are calibrated by performing similar fits to the Monte Carlo samples generated with known W masses.

6.3.1 The Monte Carlo Reweighting Technique

A reweighting factor is given to each event in CC03 W^+W^- Monte Carlo samples produced with a given mass and a given width, (M_W^{MC}, Γ_W^{MC}), to reproduce a mass spectrum corresponding to a set of arbitrary mass and width, (M_W^{new}, Γ_W^{new}). A new mass spectrum for (M_W^{new}, Γ_W^{new}) is obtained by reweighting the reconstructed mass event-by-event. The reweighting factor is the ratio of the probability that the event would be produced assuming the new values of ($M_W^{new}, \Gamma_W^{new}$) to the probability that this same event would be produced for the input values (M_W^{MC}, Γ_W^{MC}). These production probabilities are given by the W pair production cross-section [34]

$$P(M_W, \Gamma_W; m_1, m_2) \propto \mathcal{BW}(M_W, \Gamma_W; m_1)\mathcal{BW}(M_W, \Gamma_W; m_2)\sigma_0(m_1, m_2, s),$$

where m_1 and m_2 are the generator level masses of the two W bosons produced in the event and σ_0 is the Born level cross-section of the W pair production with masses (m_1, m_2) at a centre-of-mass energy $\sqrt{s}$. The values m_1 and m_2 are distributed according to the relativistic Breit-Wigner function,

$$\mathcal{BW}(M_W, \Gamma_W; m) = \frac{1}{\pi} \frac{\frac{m^2}{M_W}\Gamma_W}{(m^2 - M_W^2)^2 + \frac{m^4}{M_W^2}\Gamma_W^2}.$$

The reweighting factor for the ith event, f_i, is then given by

$$f_i = \frac{\mathcal{BW}(M_W^{new}, \Gamma_W^{new}; m_1^i)\mathcal{BW}(M_W^{new}, \Gamma_W^{new}; m_2^i)}{\mathcal{BW}(M_W^{MC}, \Gamma_W^{MC}; m_1^i)\mathcal{BW}(M_W^{MC}, \Gamma_W^{MC}; m_2^i)}.$$

The Born level cross-section cancels in the ratio since it depends only on m_1, m_2 and $\sqrt{s}$.

6.3.2 The Reweighted Monte Carlo Mass Spectra

An estimate of the reconstructed mass spectrum for any ($M_W^{new}, \Gamma_W^{new}$) can be obtained from one Monte Carlo data sample with a given input (M_W^{MC}, Γ_W^{MC}). However for very large f_i, the reweighted spectrum becomes sensitive to statistical fluctuations in the input sample. To reduce this sensitivity, a total of 850 ,000 events combined from all W^+W^- Monte Carlo samples with full detector simulation are used (PYTHIA, HERWIG, EXCALIBUR, KORALW and grc4f Monte Carlo events). These samples cover a range of input (M_W^{MC}, Γ_W^{MC}) values, spanning $M_W = 78.33$ GeV to $M_W = 82.33$ GeV and widths of 1.7 GeV to 2.5 GeV. This ensures that the reweighted spectra are reasonably smooth over a large range of (M_W^{new}, Γ_W^{new}) values.

The normalised reweighted mass spectra of the individual Monte Carlo samples are combined into a single reweighted spectrum by taking a weighted average, bin-by-bin. Figure 6.6 compares the reweighted mass distribution for the $W^+W^- \to q\bar{q}'\ell\bar{\nu}_\ell$ channel for ($M_W^{new}, \Gamma_W^{new}$) =(79.33,2.047) GeV to the spectrum from the fully-simulated PYTHIA Monte Carlo samples generated with the same (M_W^{MC}, Γ_W^{MC}). Good agreement is found over the whole region.

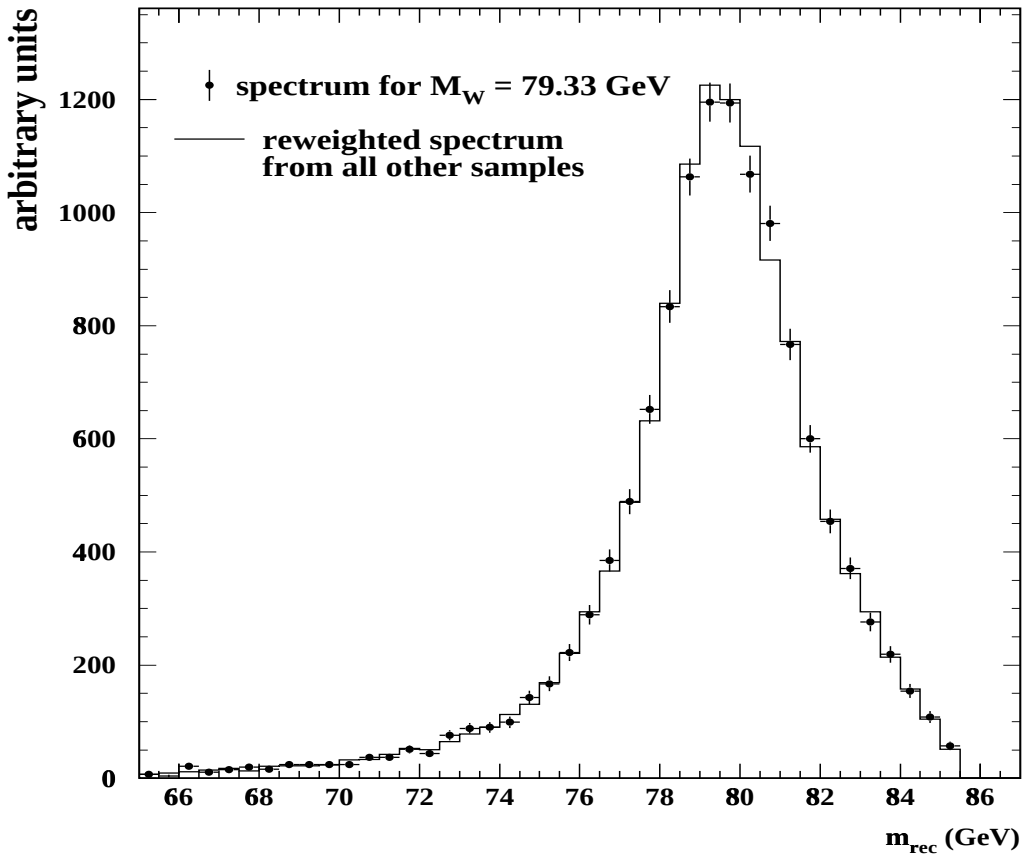

Figure 6.6: Illustration of the reweighting procedure for the reconstructed mass spectrum of the $W^+W^- \to q\bar{q}'\ell\bar{\nu}_\ell$ signal events. The spectrum produced with $M_W = 79.33$ GeV is compared with the reweighted spectrum obtained from samples with W boson masses between $M_W = 78.33$ GeV and $M_W = 82.33$ GeV. Only samples produced with the same Monte Carlo generator (PYTHIA) are used for this comparison and the $M_W = 79.33$ GeV sample has not been included in the reweighting procedure.

The background mass spectra are taken from the Monte Carlo and are assumed to be independent of M_W and Γ_W. The background distributions are normalised to the expected number of background events. The reweighted signal spectra are then normalised such that the total number of signal plus background events corresponds to the observed number of events. This is done separately for each channel.

Most of the Monte Carlo events are produced for a beam energy of $E_{beam}^{MC} = 85.50$ GeV, whereas the luminosity weighted average beam energy of the data is $E_{beam}^{data} = 86.06$ GeV. In order to correct for this, the mass M_W^{new} used for reweighting is modified to

$$M_W^{new} \to M_W^{new} \quad - \quad (E_{beam}^{data} - E_{beam}^{MC}),$$

hence shifting the resulting spectrum by $(E_{beam}^{data} - E_{beam}^{MC})$. Since not all the fully simulated samples are produced with the same centre-of-mass energy, this is done for each sample separately before combining the reweighted mass spectra. A corresponding shift is also made to the background mass spectra.

6.3.3 Fit to the Reconstructed Mass Spectrum using the Reweighting Method

A binned likelihood is formed from the product of the Poisson probabilities for obtaining the numbers of events observed in the data, N_i, in each ith bin of the reconstructed mass spectrum using the Monte Carlo expectation, $\mu_i(M_{\rm W}, \Gamma_{\rm W})$:

$$\mathcal{L} \;=\; \prod_i \frac{\mu_i^{N_i} e^{-\mu_i}}{N_i!}.$$

The number of expected events in the ith bin is given by

$$\mu_i(M_{\rm W}, \Gamma_{\rm W}) \;=\; f_s^i(M_{\rm W}, \Gamma_{\rm W}) N_s + f_b^i N_b$$

where $f_s^i(M_{\rm W}, \Gamma_{\rm W})$ is the fraction of signal events in the ith bin as determined from the reweighted spectrum corresponding to a W boson mass and width of $(M_{\rm W}, \Gamma_{\rm W})$, f_b^i is the fraction of background events in the ith bin and N_b is the expected number of background events. The number of signal events, N_s, is determined using the normalisation procedure described above. The log-likelihood curve is determined for each channel. Since each channel is statistically independent, the results are combined by adding together these likelihood curves. The resulting log-likelihood distribution as a function of the mass and the width allows the determination of $M_{\rm W}$ and $\Gamma_{\rm W}$ and their associated statistical uncertainties.

For the $\rm W^+W^- \to q\bar{q}'q''\bar{q}'''$ channel, there are three possible combination of jet-jet pairing. As discussed in Section 6.2.2, the lowest probability fit is not used. A two-dimensional mass distribution (M_1, M_2) is used to the fit, where M_1 and M_2 are the reconstructed masses corresponding to the combination having the first and second highest fit probabilities, P_1 and P_2. Both of the fit probabilities are required to be at least 1 %. For those events in which only P_1 exceeds 1 %, a one-dimensional spectrum is used. To further reduce the sensitivity to statistical fluctuations in the determination of the expected number of events, only events with a reconstructed mass in the range 65 GeV $< \rm m_{rec} <$ $\rm E_{beam}$ are included in the fit. For the two-dimensional mass spectrum, at least one of the two reconstructed masses is required to be greater than 70 GeV and the sum of the two masses must exceed 120 GeV. This rather limited mass range is also motivated by the fact that events with small reconstructed masses have very little sensitivity to $M_{\rm W}$. The numbers of events used in this analysis are listed in Table 6.3. The mass spectra of the individual channel are shown in Figure 6.7 together with the fitted reweighted spectra.

Channel	Selected events in the fit range BW method	RW method
$\rm W^+W^- \to q\bar{q}'q''\bar{q}'''$ ($P_1 > 0.01$ and $P_2 < 0.01$)	30	22
$\rm W^+W^- \to q\bar{q}'q''\bar{q}'''$ ($P_1 > 0.01$ and $P_2 > 0.01$)	12	21
$\rm W^+W^- \to q\bar{q}'e\bar{\nu}_e + W^+W^- \to q\bar{q}'\mu\bar{\nu}_\mu$	28	31
$\rm W^+W^- \to q\bar{q}'\tau\bar{\nu}_\tau$	14	17
Total	84	91

Table 6.3: Numbers of selected events in each channel for use in the W mass determination.

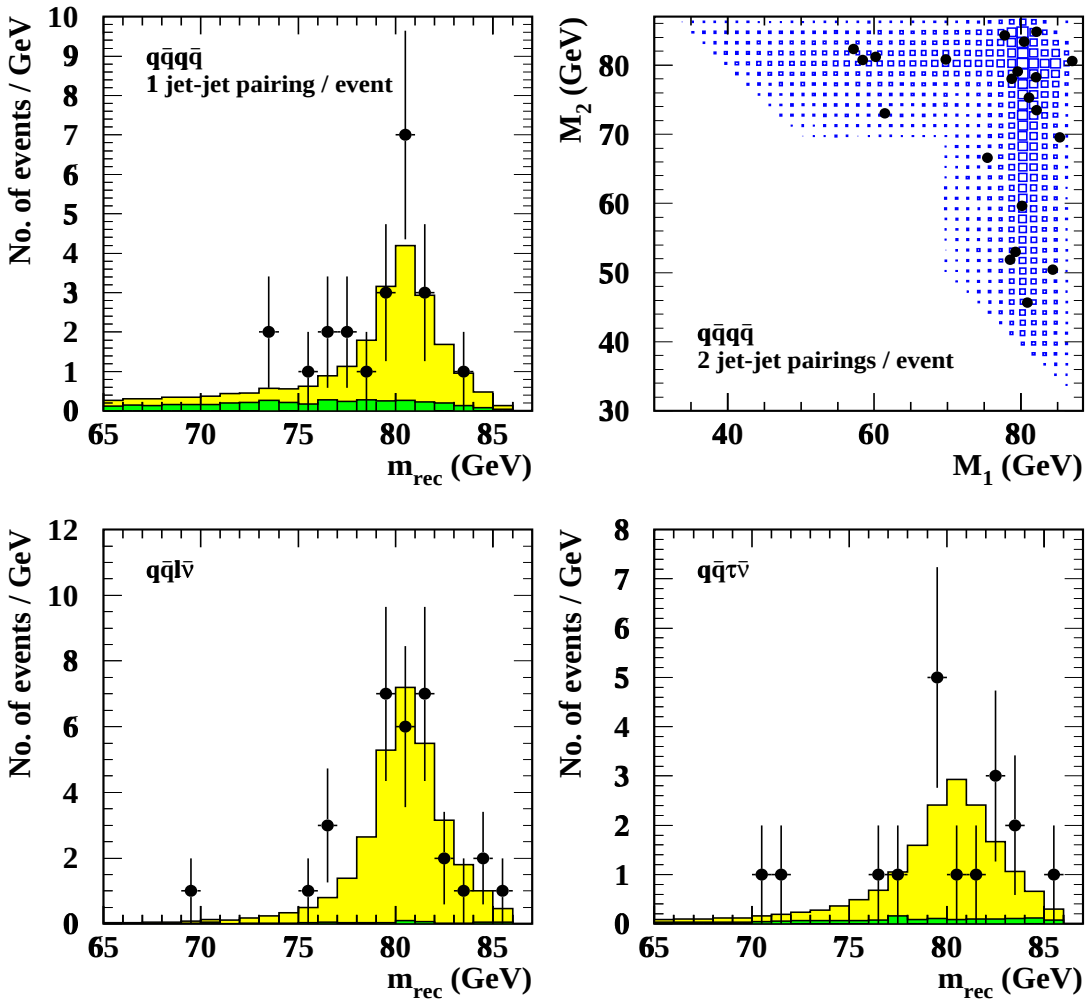

Figure 6.7: Fits to the mass spectra of the different channels using the reweighting method. The dots represent the data, the lightly shaded histograms the result from the fit for (M_{W},Γ_{W}) and the darkly shaded ones the background contributions. For the $\mathrm{W^+W^-} \to \mathrm{q\bar{q}'q''\bar{q}'''}$ candidates in which two jet-jet pairings per event are used, the underlying distribution represents the fit result. For clarity, the bin size used for the one-dimensional histograms is twice that used for the fit.

6.3.4 Bias Check of Fit Procedure with the Reweighting Method

The binned likelihood fit using the reweighting method takes into account all the effects of resolution, acceptance, ISR, and phase space and should be free from biases as long as these effects are correctly simulated. To check any biases in the reweighting procedure, various studies are made using fully simulated subsamples each corresponding to the same integrated luminosity as the data.

Consistencies of the fitted M_{W} are studied by fitting the PYTHIA Monte Carlo samples with input W masses between 78.33 GeV and 82.33 GeV. Only the PYTHIA samples are used in the reweighting procedure, excluding the sample being fitted. In Figure 6.8 (a), the shift of the fitted M_{W} from the input value is plotted as a function of input M_{W}. In the $\mathrm{q\bar{q}'}\ell\bar{\nu}_\ell$ channel no bias and no dependence on the input mass are found. In the $\mathrm{q\bar{q}'q''\bar{q}'''}$ channel there is an indication of a small systematic effect which is believed to be an artifact of finite Monte Carlo

statistics of the samples employed in the reweighting procedure. For values of $M_{\rm W}$ in the range of interest, 80.33 $\pm$ 0.50 GeV, this bias is within $\pm$20 MeV. A similar test is also performed with the different $\Gamma_{\rm W}$ and no bias is found for all channels.

The procedure to correct the difference between the actual beam energy and the beam energy with which the Monte Carlo samples are generated is checked in a similar way. Using only the PYTHIA samples generated with $\sqrt{s}$ = 171 GeV for the reweighting and background estimation, the fit is performed for PYTHIA subsamples generated with $\sqrt{s}$ = 172 GeV. No significant bias is observed.

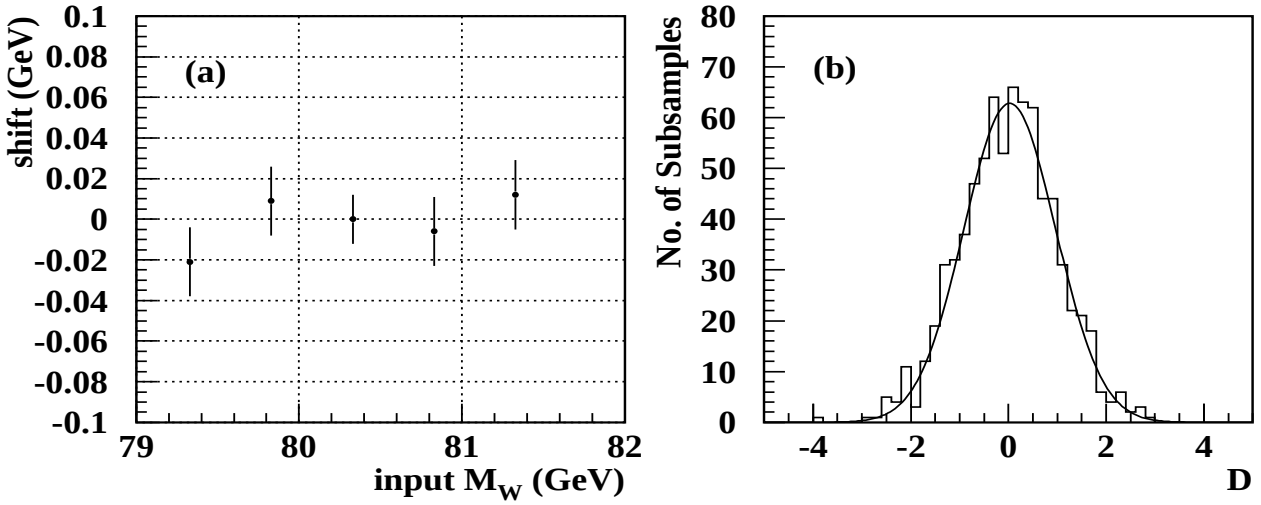

Figure 6.8: Results of the self-consistency checks in the reweighting procedure. The subsamples of the PYTHIA Monte Carlo are used in the study. Plot (a) shows the difference between the input and the fitted W mass at five different input $M_{\rm W}$ values. A combined result of the $\mathrm{q\bar{q}'}\ell\bar{\nu}_\ell$ channel and $\mathrm{q\bar{q}'q''\bar{q}'''}$ channel is plotted. Plot (b) shows the D distribution with the Monte Carlo subsamples for the $\mathrm{q\bar{q}'}\ell\bar{\nu}_\ell$ channel. The definition of the D is in the text.

In order to study the reliability of the fitted errors, a following parameter is defined as

$$D = \frac{M_{\rm W}^{fit} - M_{\rm W}^{MC}}{\sigma^{fit}},$$

where the $M_{\rm W}^{MC}$ is the input W mass and the σ^{fit} is the fitted errors for each subsample. These studies demonstrate that the error returned by the fit accurately reflects the r.m.s. spread of the fitted mass distribution. Figure 6.8 (b) presents the D distribution with $M_{\rm W}$ = 80.33 GeV for the $\mathrm{q\bar{q}'}\ell\bar{\nu}_\ell$ channel. Although the fitted error is slightly overestimated, the obtained distribution is symmetric and it forms the Gauss distribution. For further investigation of the reliability, additional 2000 Monte Carlo test subsamples are used, each corresponding to the same integrated luminosity as the data. No significant bias has been found in the fitting error estimation.

The bin width and the fit range have been varied to see their effect to the fitting. No significant effect is observed.

At last background treatment in this fitting procedure is considered. The effect of the finite Monte Carlo statistics of the background samples is studied by comparing the results of

repeated fits to a Monte Carlo sample using only fractions of the background sample. Variations in the normalisation of the predicted backgrounds, based upon uncertainties in the background cross-sections and efficiencies is verified too. The combined background is varied by 20% in the $q\bar{q}'q''\bar{q}'''$ channel, and 40% in the $q\bar{q}'\ell\bar{\nu}_\ell$ channels. The observed shifts in these studies are small and they are taken as systematic uncertainties.

6.3.5 Curve Fit with the Breit-Wigner Function

A variety of analytic forms to describe the signal and background shapes were investigated. From Monte Carlo studies the signal shape is found to be well described up to $m_{rec} \sim 84$ GeV by a function based on a relativistic Breit-Wigner function with fixed width,

$$S(m_{rec}) \;=\; \frac{m_{rec}^2\Gamma^2}{(m_{rec}^2 - m_0^2)^2 + m_{rec}^2\Gamma^2},$$

where m_0 and Γ are characteristic parameters of the signal peak. The fits are limited to the range 40–84 GeV, where the lower boundary is determined by considerations regarding the background normalisation and is discussed below. The width, Γ, should be regarded as a parameter which embodies both the width of the W boson and experimental effects and is fixed to the value predicted by the Monte Carlo, 3.8 GeV.

Background arises mainly in the $W^+W^- \to q\bar{q}'q''\bar{q}'''$ channel, both from $Z^0/\gamma \to q\bar{q}$ events, and from incorrect combinations in $q\bar{q}'q''\bar{q}'''$ events. Monte Carlo studies show that a quadratic form in m_{rec} describes the combinatorial background well up to $m_{rec} \sim 84$ GeV. The $q\bar{q}$ background has a different shape. It was found that this can be described by the function $Ap^\alpha e^{-\beta p}$, where $p = \sqrt{E_{\rm beam}^2 - m_{rec}^2}$ is the momentum with which a W pair of mass m_{rec} would have been produced and α and β are positive parameters. The shapes and relative normalisation of the background contributions are determined from Monte Carlo samples, but their overall normalisation is allowed to vary in the fit. Extending the allowed fit range down to 40 GeV improves the determination of the background fraction in the peak region, since this low mass region is dominated by background.

To extract $M_{\rm W}$ from the reconstructed mass distribution, an unbinned maximum likelihood fit to the relativistic Breit-Wigner plus background function, described above, is used. The fit is performed using the reconstructed mass distribution from all channels combined. In the $q\bar{q}'q''\bar{q}'''$ channel both the highest probability fit and second highest probability fit are included in the reconstructed mass distribution if both of the kinematic fit probabilities, P_1 and P_2 exceed 1%. For the second fit case a further constraint is required, $P_2 > 1/3\, P_1$. To reduce background and remove poorly reconstructed events in the $q\bar{q}'\tau\bar{\nu}_\tau$ channel, the kinematic fit probability must be greater than 0.01, though the mass is reconstructed with the scaling (see 6.2). The numbers of events used in this analyses are listed in Table 6.3. For comparison, it is also performed on the $q\bar{q}'q''\bar{q}'''$ and $q\bar{q}'\ell\bar{\nu}_\ell$ channels separately. In these cases the widths are fixed to different values in the two channels. The fit results are compared with the data in Figure 6.9.

The correction for the bias is estimated using PYTHIA Monte Carlo events corresponding to various input values of $M_{\rm W}$ and the beam energy, $E_{\rm beam}$. Monte Carlo subsamples of signal and background events corresponding to the integrated luminosity of the data are processed through the same event selection, mass reconstruction, and fitting routines as the data. The mean correction is determined by fitting a Gaussian to the resulting distribution of $(m_0^{\rm fit} - m_{\rm W}^{\rm true})$

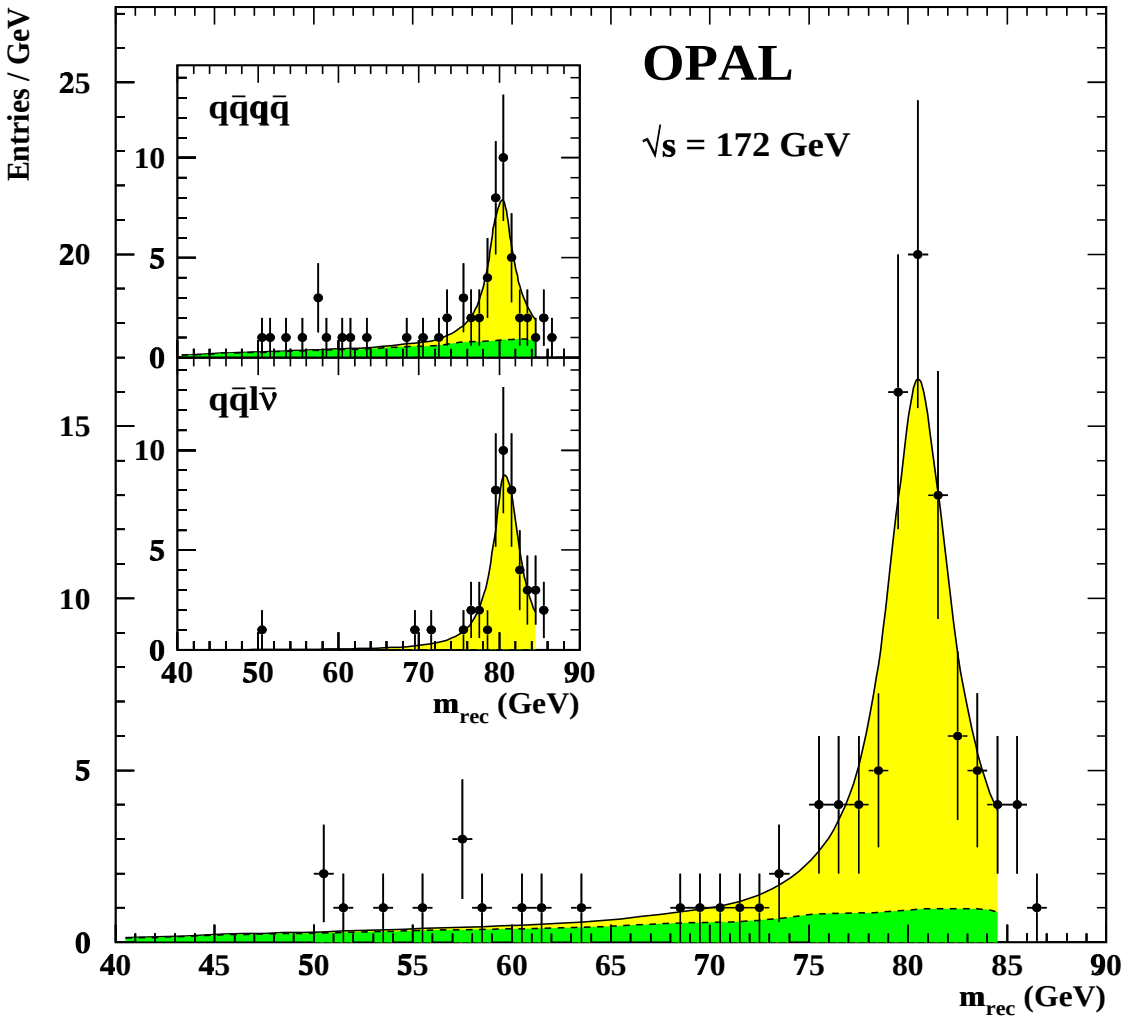

Figure 6.9: Reconstructed mass distributions for the data. The main plot shows the W^+W^- $\rightarrow q\bar{q}'q''\bar{q}'''$ and $W^+W^- \rightarrow q\bar{q}'\ell\bar{\nu}_\ell$ samples combined, and the inserts present them separately. The solid curves display the results of unbinned maximum likelihood fits to a relativistic Breit-Wigner signal plus background in the range 40-84 GeV as described in the text. The background function alone is shown by the dark shaded region.

where $m_{\mathrm{W}}^{\mathrm{MC}}$ is the W boson mass with which the Monte Carlo sample is generated. This correction is found to depend linearly on $(E_{\mathrm{beam}} - m_{\mathrm{W}}^{\mathrm{MC}})$, as shown in Figure 6.10. A straight line fit yields:

$$\begin{aligned}
\mathrm{W^+W^-} \to \mathrm{q\bar{q}'q''\bar{q}'''}: \quad & m_0^{\mathrm{fit}} - m_{\mathrm{W}}^{\mathrm{MC}} = -0.363 + 0.0911(E_{\mathrm{beam}} - m_{\mathrm{W}}^{\mathrm{MC}}) \\
\mathrm{W^+W^-} \to \mathrm{q\bar{q}'}\ell\bar{\nu}_\ell: \quad & m_0^{\mathrm{fit}} - m_{\mathrm{W}}^{\mathrm{MC}} = -0.107 + 0.0768(E_{\mathrm{beam}} - m_{\mathrm{W}}^{\mathrm{MC}}) \\
\mathrm{Combined}: \quad & m_0^{\mathrm{fit}} - m_{\mathrm{W}}^{\mathrm{MC}} = -0.193 + 0.0779(E_{\mathrm{beam}} - m_{\mathrm{W}}^{\mathrm{MC}})
\end{aligned}$$

with the masses and energies expressed in GeV. These relations are used to correct the fitted mass for all biases.

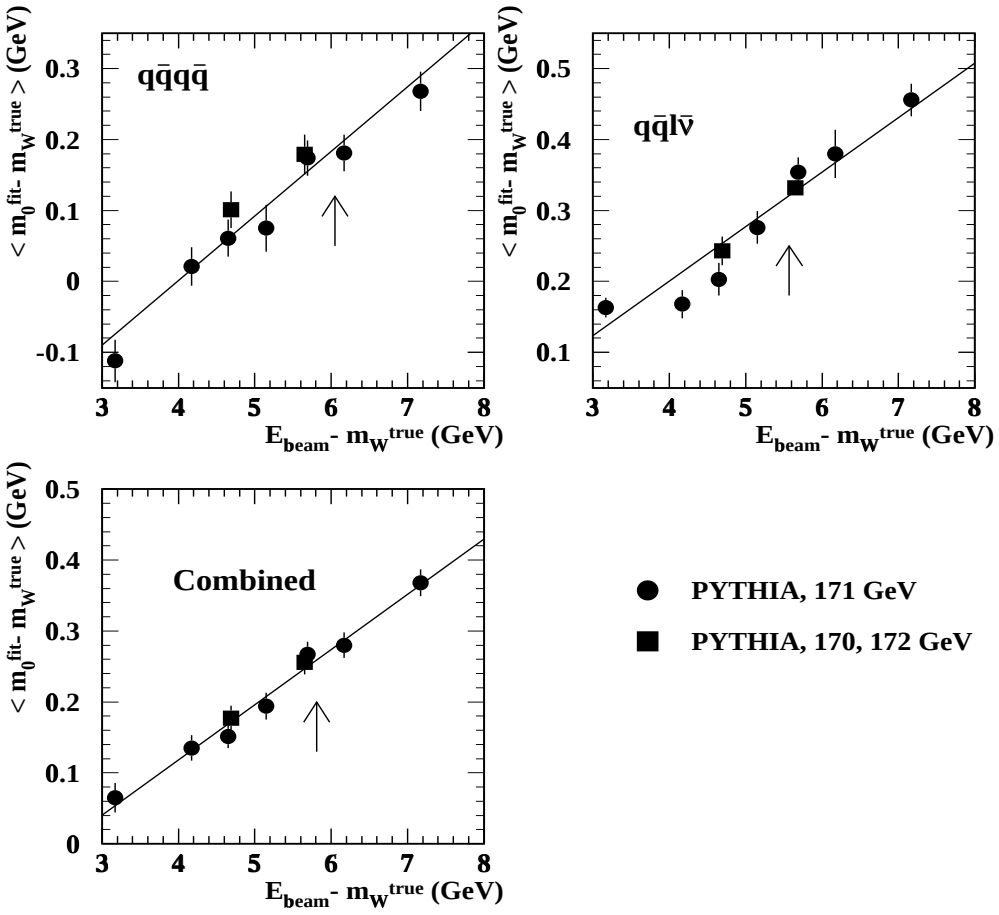

Figure 6.10: Mean of the difference between fitted and true mass from fits to many Monte Carlo subsamples, for PYTHIA Monte Carlo events generated with various input W masses and at different beam energies, plotted as a function of the difference between beam energy and true mass. The $\mathrm{W^+W^-} \to \mathrm{q\bar{q}'q''\bar{q}'''}$ and $\mathrm{q\bar{q}'}\ell\bar{\nu}_\ell$ samples are shown separately, as well as both combined. The lines represent fits to the points, with parameters given in the text. The arrows indicate the actual corrections applied.

6.4 Systematic Errors

The main sources of systematic uncertainty in the W mass measurement at $\sqrt{s} = 172$ GeV are studied by changing some features of the analysis. Errors coming from the accelerator, the knowledge of the underlying physics phenomena, the detector, and the fitting procedure, are considered. All studies are done for both of the fit methods using the reweighting and the Breit-Wigner function. The overall systematic errors calculated for the two analyses are in good agreement. The estimated errors are summarised in Table 6.4.

Systematic errors	BW-fit to M_W fixed width			RW-fit to M_W SM constrained width			RW-fit to M_W and Γ_W	
(MeV)	$q\bar{q}'q''\bar{q}'''$	$q\bar{q}'\ell\bar{\nu}_\ell$	comb.	$q\bar{q}'q''\bar{q}'''$	$q\bar{q}'\ell\bar{\nu}_\ell$	comb.	M_W	Γ_W
Beam Energy	27	27	27	30	30	30	30	15
ISR	22	22	22	20	20	20	20	61
Hadronisation	16	16	12	52	26	20	21	52
Four-fermion	42	37	37	42	48	42	35	70
Detector Effects	67	87	54	62	76	48	48	98
Fit procedure and Background	33	65	36	32	28	25	25	85
Colour Reconnection and Bose-Einstein	100	0	50	100	0	50	50	50
Total systematic error	137	121	96	144	104	94	92	175

Table 6.4: Summary of the systematic errors for the various fit methods. For the one-parameter fits to determine M_W, uncertainties are given for the fits to $W^+W^- \rightarrow q\bar{q}'q''\bar{q}'''$, $q\bar{q}'\ell\bar{\nu}_\ell$ and for the combined sample. For the two-parameter fit, the uncertainties for M_W and Γ_W are listed separately only for the fits to the combined sample.

6.4.1 Uncertainties of Beam Energy

Uncertainties in the LEP beam energy affect the reconstructed mass spectrum through the energy constraints imposed by the kinematic fit. The precision of the beam energy is estimated to be ± 30 MeV [14]. The influence of this uncertainty in the fit results is estimated by changing the beam energy in independent samples of signal and background Monte Carlo before performing the kinematic fits. In addition, the effect of a possible asymmetry between the e^+ and e^- energies is studied and found to be negligible.

6.4.2 Detector Effects

The effects of detector mis-calibrations and deficiencies in the Monte Carlo simulation of the data have been investigated by varying the inputs to the kinematic fit over reasonable ranges. The range is determined in each case from a detailed comparison of data and Monte Carlo using approximately 1.2 pb^{-1} of data recorded at $\sqrt{s} \sim M_Z$ during 1996. The following effects are considered:

- The Monte Carlo simulation is found to be accurate to within 1 % for the jet energy scale. The effect on the reconstructed masses is found to be negligible in both the data and the Monte Carlo.

- The calibration of the lepton momentum or energy scale is also found to be accurate to within 1%. The corresponding changes for the semi-leptonic (e/μ) channels are taken as systematic errors.

- Results of the kinematic fit depend on the error matrix of the input parameters, which are determined using Monte Carlo events. The jet energy errors in the data are understood to within 3%. No indication of mis-modeling of the errors associated with the jet angles was found. No indication is found for the corresponding lepton parameters either. According to the estimation of these uncertainties, the varied error matrix within its estimated uncertainty is input to the kinematic fit.

- At last the studies using the alternative algorithm of jet energy reconstruction and a different parameterisation of the jet errors, described in section 6.2.3, are considered. In addition, the mass reconstruction without using the hadron calorimeter is repeated to check a dependence of the hadron calorimeter. In general an energy resolution of the hadron calorimeter is much worse than that of the electromagnetic calorimeter or a track momentum resolution, and the contribution of neutral hadrons whose energies can only be measured with the hadron calorimeter is expected to be small. In all of these checks, the mean and r.m.s. of the shifts in the reconstructed masses observed in the data are compatible with the expectations from the Monte Carlo. The statistical precision of each comparison is taken as the associated uncertainty, and the largest of these is included in the total systematic error.

The errors from all of these checks are added in quadrature to give the total systematic error due to uncertainties associated with detector mis-calibrations and mis-modeling. This is the dominant experimental systematic uncertainty.

6.4.3 Theoretical Uncertainties

The following uncertainties are considered from theoretical aspects.

Initial State Radiation: The effect of initial state radiation is to increase systematically the reconstructed invariant mass, and consequently the resulting fitted mass, due to a bias introduced through the energy conservation constraint of the kinematic fit. This bias is already taken into account in the extraction of the W mass to the extent that ISR is accurately modeled in the Monte Carlo. The KORALW generator is used to estimate the systematic error associated with the incomplete modeling of ISR. Distributions of the mean M_{W} per event are compared in two samples, one including only first order corrections and the other including the full second order ISR corrections. From fits to these generator level distributions systematic uncertainties of 20 MeV for the mass is assigned.

Hadronisation: Sensitivity of the results to the choice of the hadronisation model is studied in two ways. In the first approach, a single sample of $\mathrm{W^+W^-}$ four-fermion final states is

hadronised separately by both PYTHIA and HERWIG, and the fit results are compared. By using the same four-fermion final states the comparison is sensitive only to the difference in hadronisation. Alternatively, the mean difference between the reconstructed mass and the generator level average mass is determined for the PYTHIA and HERWIG W^+W^- samples separately. No significant difference is observed in either comparison and the statistical precisions of the tests are taken as the systematic errors. Varying the hadronisation model for the background is found to have a negligible effect.

Four-fermion Interference Effects: The Monte Carlo samples used to calibrate in the fitting procedure include only the CC03 diagrams. In order to test the sensitivity of the results to the interference between the W^+W^- diagrams and other four-fermion processes, the fit results of a sample generated with the full set of interfering four-fermion diagrams are compared to one restricted to the CC03 W^+W^- diagrams alone. The comparison is made using both the grc4f generator and the EXCALIBUR generator. A small mass shift is found when using EXCALIBUR, while no such indication was found using grc4f. The assigned uncertainties accommodate the results from these two models.

Colour Reconnection Effects and Bose-Einstein Correlations: As discussed in [6] and references therein, a significant bias to the apparent W mass measured in the $W^+W^- \to q\bar{q}'q''\bar{q}'''$ channel could arise from the effects of color reconnection and Bose-Einstein correlations between the decay products of the W^+ and W^-. Neither of these effects are included in the currently available hadronisation models. There is no consensus to the magnitude of the effects, though in some models they produce a shift in the measured M_W by as much as +100 MeV [6]. In some models, color reconnection also affects other properties of $W^+W^- \to q\bar{q}'q''\bar{q}'''$ events, for example, the charged particle multiplicity. As is discussed in the reference [2], with the sensitivity afforded by the present statistics no indication of such reconnection effects is observed. In the absence of an experimental limit to the biases associated with these phenomena, a systematic uncertainty of $\pm$100 MeV is assigned to the $q\bar{q}'q''\bar{q}'''$ channel due to these effects. As the $q\bar{q}'q''\bar{q}'''$ channel comprises approximately half the total signal sample an uncertainty of $\pm$ 50 MeV is assigned in the combined analysis. One possible test of such effects is to compare the M_W values measured in the $q\bar{q}'q''\bar{q}'''$ channel with that determined from $q\bar{q}'\ell\bar{\nu}_\ell$. Within the present experimental errors the results are compatible.

6.4.4 Fitting Procedure with the Reweighting Method

Studies for possible biases associated with the fitting procedure of the reweighting are described in Section 6.3.4. Errors coming from the reweighting procedure for the $q\bar{q}'q''\bar{q}'''$ channel, from the statistical accuracy of the test which checks the beam energy treatment, and from the background treatment are assigned as the residual systematic errors. Using 800 fully simulated Monte Carlo subsamples corresponding to the same integrated luminosity as the data sample, the size of each error is estimated. All errors are added in quadrature to give the total systematic error.

6.4.5 Fitting Procedure with the Breit-Wigner Function

The effects of using different analytic functions to describe the signal and background shapes, of fixing various fitted parameters, and of varying the fit range are investigated. In each case, the shift in the fit mass observed in the data is compared with the expected shift estimated using 400 Monte Carlo subsamples, each corresponding to the same integrated luminosity as the data. The following variations are considered:

- A simple non-relativistic Breit-Wigner is used for the signal.
- The relativistic Breit-Wigner is multiplied by a factor p^{α}, where α is a free parameter, and p is the centre-of-mass momentum of a pair of particles of mass m_{rec}. In this case, the data are fitted up to the kinematic limit in m_{rec} with α fixed to the value determined from Monte Carlo.
- The width parameter, Γ, is left as a free parameter in the fit.
- The background is represented by a quadratic in m_{rec}, with parameters determined in the fit to the data.
- The background normalisation is fixed to that expected from Monte Carlo.
- The relative normalisation of the combinatorial and $\Gamma_Z \rightarrow q\bar{q}$ backgrounds is varied by $\pm 50\%$.
- The masses of the combinatorial and $q\bar{q}$ backgrounds are displaced by 1 GeV.

In each case, the shift in fitted mass observed in the data is consistent with that estimated from the Monte Carlo. The r.m.s. deviation of the differences of the observed shift between the data and Monte Carlo is taken as a systematic error.

6.5 Results of 172 GeV Analysis

The results of the analysis using the reweighting method for the 172 GeV data are as follows;

$$\begin{aligned} W^+W^- \rightarrow q\bar{q}'q''\bar{q}''' : \quad M_W &= 80.08 \pm 0.44 \pm 0.14 \text{ GeV}, \\ W^+W^- \rightarrow q\bar{q}'\ell\bar{\nu}_\ell : \quad M_W &= 80.53 \pm 0.41 \pm 0.10 \text{ GeV}, \\ \text{Combined} : \quad M_W &= 80.32 \pm 0.30 \pm 0.09 \text{ GeV}, \end{aligned}$$

where the width is constrained by the Standard Model relation,

$$\Gamma_W = (2.0817 \text{ GeV}) \frac{M_W^3}{(80.26 \text{ GeV})^3},$$

in the fit. The errors are statistical and systematic, respectively. At the current precision of the M_W measurement the statistical error is dominant.

The error on the fitted mass is correlated with the width of the reconstructed mass distribution. If M_{W} and Γ_{W} are taken as free parameters, the two-parameter fit gives

$$\begin{aligned} M_{\mathrm{W}} &= 80.30 \pm 0.27 \pm 0.09 \text{ GeV}, \\ \Gamma_{\mathrm{W}} &= 1.30^{+0.62}_{-0.55} \pm 0.18 \text{ GeV}, \end{aligned}$$

where the errors are statistical and systematic, respectively. The likelihood contours for the statistical errors are shown in Figure 6.11 together with the Standard Model prediction.

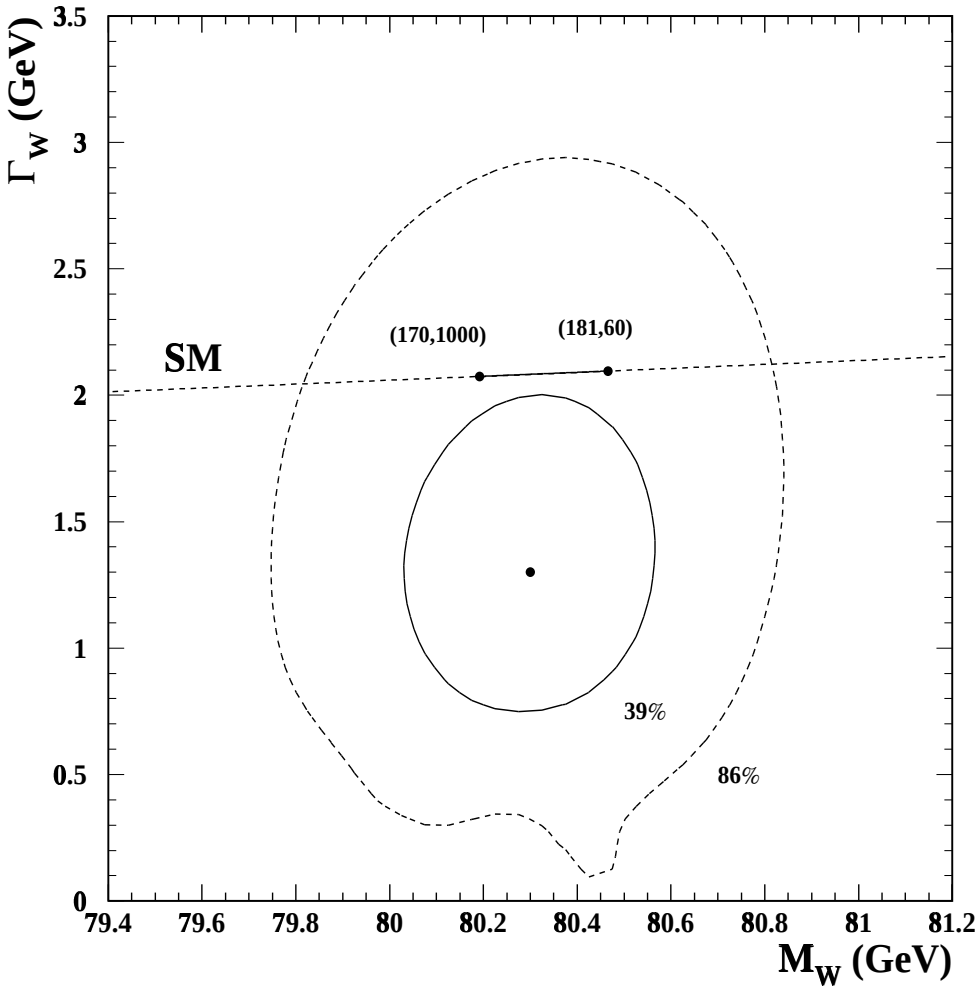

Figure 6.11: The 39% and 86% contour levels of the two-parameter fit using the reweighting method. The projections of these contours onto the axes give the one and two standard deviation errors quoted in the text. The straight dashed line gives the dependence of the width on the mass according to the Standard Model. The one-parameter fit for the mass alone is constrained to this line. The solid line is the Standard Model prediction for variations of (M_{top},M_{Higgs}), both given in GeV. For small fitted values of Γ_{W}, the 86% contour is very sensitive to the particular distribution of masses observed in the data.

Since this measurement is principally intended to determine the W mass as a Standard Model parameter, the result of the one-parameter fit is taken as the central result of this thesis for the W mass. The value of M_{W} obtained from the unbinned likelihood using the analytic Breit-Wigner function is consistent with that obtained using the reweighting method. The fitted masses, corrections and corrected masses using the analytic Breit-Wigner function are given in Table 6.5. Despite the difference in the two M_{W} determination procedures, the sizes of statistic and systematic errors are also in good agreement.

	$\mathrm{W^+W^-} \rightarrow \mathrm{q\bar{q}'q''\bar{q}'''}$	$\mathrm{W^+W^-} \rightarrow \mathrm{q\bar{q}'\ell\bar{\nu}_\ell}$	combined
Fitted mass (GeV)	80.19 ± 0.39	80.80 ± 0.37	80.50 ± 0.27
MC correction (GeV)	-0.19 ± 0.01	-0.32 ± 0.01	-0.26 ± 0.01
Corrected mass (GeV)	$80.01 \pm 0.43 \pm 0.14$	$80.48 \pm 0.40 \pm 0.12$	$80.24 \pm 0.30 \pm 0.10$

Table 6.5: Summary of fit results and Monte Carlo corrections to M_{W} for the BW fit method. The errors on the fitted mass and corrections are statistical only, while for the corrected mass the statistical and systematic errors are both listed (see Section 6.4 for details).

The reconstructed mass spectrum is independent of the cross-section information. As the CC03 cross-section at $\sqrt{s} = 172$ GeV depends, but weakly, on M_{W}, it can be obtained from the measured cross-section, $\sigma_{\mathrm{WW}}(172\ \mathrm{GeV}) = 12.3 \pm 1.3 \pm 0.3$ pb [2]. With the similar method to the 161 GeV analysis of using the GENTLE programme, the W mass can be obtained to be

$$M_{\mathrm{W}} = 80.5^{+1.4+0.5}_{-2.2-0.6}\ \mathrm{GeV}.$$

A combined result of the M_{W} at $\sqrt{s} = 161$-172 GeV is presented and discussed in Chapter 7.

Chapter 7

Discussion

7.1 Combined Result

Two measurements at $\sqrt{s} = 161$ GeV and 172 GeV utilize quite different approaches to determine the mass of the W boson. These measurements are thus complementary with each other. Except for the beam energy uncertainty, the errors of each measurement are considered to be independent. The obtained results are compatible with each other. Therefore we can combine the two measurements, yielding in the result of

$$M_{\mathrm{W}} = 80.35 \pm 0.24 \pm 0.06 \pm 0.03 \pm 0.03 \text{ GeV},$$

where the errors are the statistical, systematic, effects of color reconnection and Bose-Einstein correlation, and beam energy uncertainties, respectively.

7.2 Comparison with Other Measurements

The other three LEP2 experiments, ALEPH, DELPHI, and L3, have presented their measurements of the W mass with similar methods at $\sqrt{s} = 161$ GeV [35] and 172 GeV [36]. The results of their M_{W} measurements values are consistent with the OPAL results. Their statistical and systematic errors are also of similar sizes. Combined results of the four experiments are obtained to be

$$\begin{aligned} M_{\mathrm{W}} &= 80.40 \pm 0.22 \text{ GeV at } \sqrt{\mathrm{s}} = 161 \text{ GeV}, \\ M_{\mathrm{W}} &= 80.53 \pm 0.18 \text{ GeV at } \sqrt{\mathrm{s}} = 172 \text{ GeV}. \end{aligned}$$

At $\sqrt{s} = 161$ GeV the M_{W} value is determined from the combined CC03 $\mathrm{W^+W^-}$ cross-section using the GENTLE semi-analytic programme. The combined result of the 161 GeV data and the 172 GeV data is shown in Figure 7.1.

The measurement of the W boson mass at $\mathrm{p\bar{p}}$ colliders uses a different method from those at LEP2. Using clear signals of $\mathrm{W} \rightarrow \mathrm{e}\bar{\nu}_{\mathrm{e}}$ or $\mu\bar{\nu}_{\mu}$ decays, they measure the W mass. The

signature of a W $\rightarrow$ $e\bar{\nu}_e$ ($\mu\bar{\nu}_\mu$) decay is identified as an isolated high p_t electron (muon) and large missing transverse momentum. Since $p_z(\nu)$ is unknown, the invariant mass can not be reconstructed. Instead of the invariant mass, the electron (muon) transverse momentum, p_t, or the transverse mass,

$$m_T = \sqrt{2p_t(l)p_t(\nu)(1-\cos(\phi(l)-\phi(\nu)))},$$

where l = e or μ, is used as a kinematic variable for the mass measurement. The sharp end-point spectrum of these variables has the information of M_W.

The combined result of the $p\bar{p}$ collider experiments is shown in Figure 7.1. The world average of the direct measurements is also shown together.

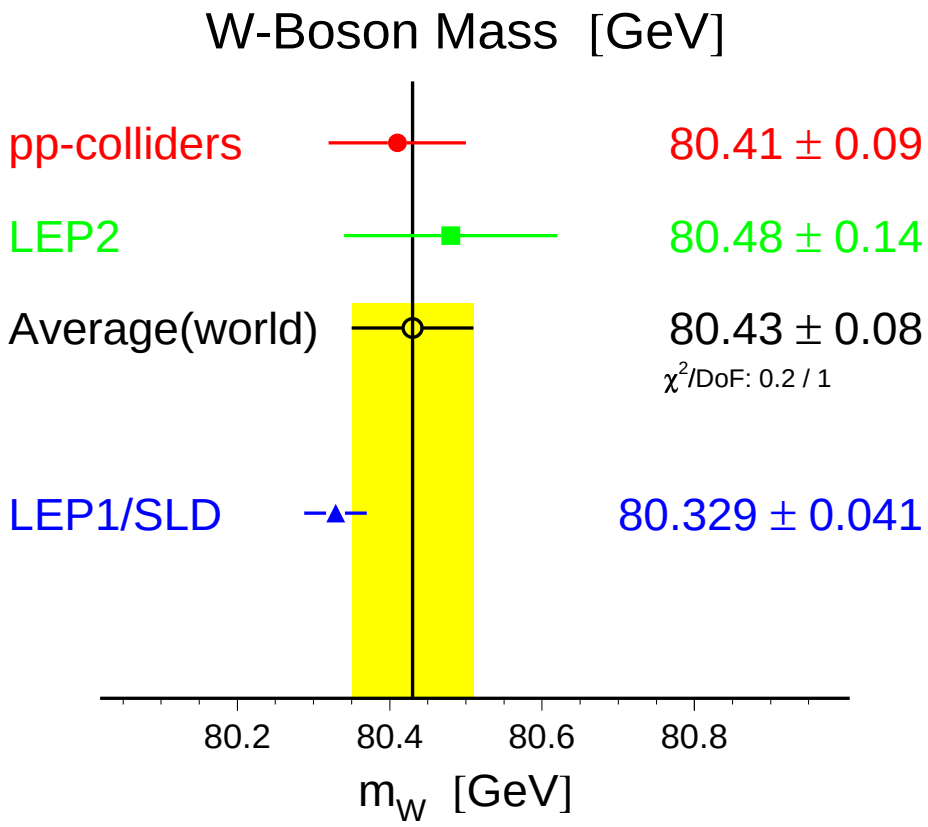

Figure 7.1: Current status of the W mass measurement, from Ref.[37].

7.3 Comparison with the Theories

The current value from the indirect measurement through the global Standard Model fit is also shown in Figure 7.1. The M_W value from the direct measurements is slightly higher than the indirect value, but both agree well within the errors. A fit including all data from the electroweak measurements yields an upper limit of the Higgs bosn mass, $M_H < 420$ GeV at 95 % confidence level. The lower limit on M_H of approximately 77 GeV obtained from direct searches is not used in the determination of this upper limit.

Figure 7.2 is the same plot as Figure 1.1,where the current world averages of $M_{\rm W}$ (80.43 $\pm$ 0.08 GeV) and $M_{\rm t}$ (175.6 $\pm$ 5.5 GeV) are shown together. Although the central point tends to prefer the MSSM, both the Standard Model and the MSSM are consistent with the measured $M_{\rm W}$ and $M_{\rm t}$ values with the present accuracy.

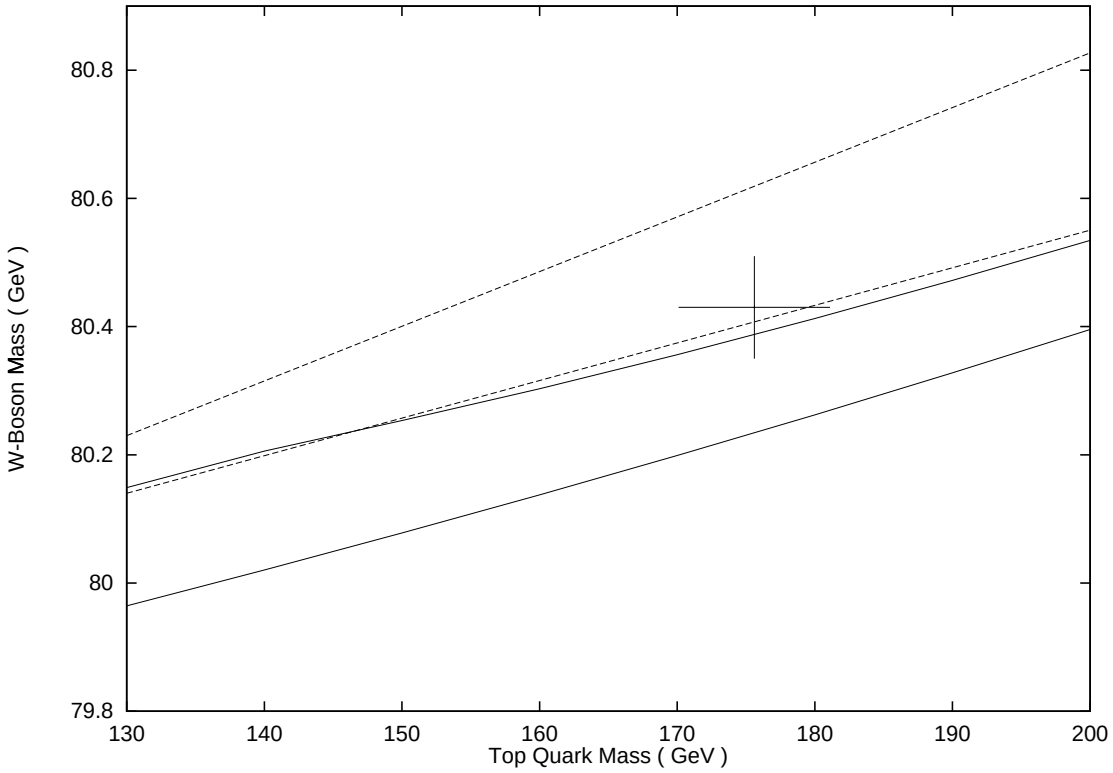

Figure 7.2: Predictions for $M_{\rm W}$ as a function of $M_{\rm t}$ in the SM (solid lines) and in the MSSM (dashed lines), from Ref.[7]. The current experimental results of $M_{\rm W}$ and $M_{\rm t}$ are presented.

7.4 Future Prospects

In 1997 LEP2 was operated at $\sqrt{s}$ = 183 GeV. Each experiment collected a data sample of an integrated luminosity of more than 50 pb^{-1}, corresponding to more than 600 $\rm W^+W^-$ candidates. As the expected statistical error of $M_{\rm W}$ is estimated to be around 140 $\sim$ 150 MeV per each experiment, the accuracy of the LEP2 combined result will be improved to be compatible with the current world average. Although the common systematic error of the current $M_{\rm W}$ measurements at LEP2 is roughly 70 MeV, it will be reduced by the studies of the W properties using the large samples of W pairs. Further improvement of the W boson mass measurement is expected in the future LEP2 experiments.

Chapter 8

Conclusion

The W boson pairs are successfully produced in e^+e^- collision at LEP2. In the OPAL detector a total of 28 and 120 candidates have been observed for an integrated luminosity of 9.89 ± 0.06 pb^{-1} at $\sqrt{s} = 161.3$ GeV and 10.36 ± 0.06 pb^{-1} at $\sqrt{s} = 172.12$ GeV, respectively. For each centre-of-mass energy the optimum method is adopted to derive the W boson mass.

The cross-section at the centre-of-mass energy just above the W^+W^- production threshold is sensitive to the mass of the W boson. From an analysis of the accepted cross-section at $\sqrt{s} =$ 161.3 GeV based on a calculation of complete four-fermion processes, the W mass is measured to be

$$M_W = 80.40^{+0.44+0.09}_{-0.41-0.10} \pm 0.03 \text{ GeV},$$

where the first and second uncertainties are statistical and systematic, respectively, and the third arises from the beam energy uncertainty.

At higher centre-of-mass energy, $\sqrt{s} = 172.12$ GeV, the measurement of the W mass is performed from the direct reconstruction of the invariant mass of the W decay products. The kinematic fit techniques, imposing energy-momentum conservation and equality of the two W masses in each event, are used to improve the mass resolution. A Monte Carlo based reweighting method is utilized to fit the reconstructed mass spectra of the selected hadronic and semi-leptonic W pair events. The result is

$$M_W = 80.32 \pm 0.30 \pm 0.09 \text{ GeV},$$

where the first uncertainties is statistical and the second is systematic.

The measured M_W values from the W^+W^- production cross-section and from the direct reconstruction can be combined, assuming that the systematic effects are uncorrelated, apart from the uncertainty associated with the LEP beam energy. The result is obtained to be

$$M_W = 80.35 \pm 0.24 \pm 0.07 \text{ GeV},$$

where the errors are the statistical and systematic, respectively.

These results are in good agreement with those of other LEP2 measurements and the $p\bar{p}$ collider measurements. No discrepancy is found between our results and the Standard Model expectation.

Appendix A

The Standard Model

The Standard Model of the electro-weak interaction is based on a gauge invariant quantum field theory with the symmetry group $SU(2) \times U(1)$. The $SU(2)$ part represents the weak isospin symmetry, and the $U(1)$ part is for the weak hyper-charge. In the theory, the spontaneous symmetry breaking with the Higgs mechanism generates the masses of the W and Z^0 bosons.

The model includes three generations spin -1/2 spin fermions; neutrinos(ν_e, ν_μ, ν_τ), charged leptons (e, μ, τ), quarks with charge 2/3 (u, c, t) and -1/3 (d, s, b), and intermediate bosons $W^{\pm}$, Z^0, γ. Each fermion has a corresponding antiparticle. It should be noted, however, the number of generations cannot be predicted by the theory. In order to take into account the fact that the charged current (CC) interactions are of the V-A form (V = vector, A = axial-vector), the left-handed fermions are put into weak isospin doublets;

$$leptons : \begin{pmatrix} \nu_e \\ e \end{pmatrix}_L \begin{pmatrix} \nu_\mu \\ \mu \end{pmatrix}_L \begin{pmatrix} \nu_\tau \\ \tau \end{pmatrix}_L$$

$$quarks : \begin{pmatrix} u \\ d \end{pmatrix}_L \begin{pmatrix} c \\ s \end{pmatrix}_L \begin{pmatrix} t \\ b \end{pmatrix}_L ,$$

while right-handed fermions are isospin singlets in the minimal Standard Model;

$$leptons : e_R \ \mu_R \ \tau_R$$

$$quarks : u_R \ c_R \ t_R \ d_R \ s_R \ b_R.$$

The left-handed and right-handed fields for a fermion, f, are defined by;

$$\begin{aligned} f_L &= \frac{1}{2}(1 + \gamma_5)f, \\ f_R &= \frac{1}{2}(1 - \gamma_5)f. \end{aligned}$$

The right-handed neutrinos do not exist.

Three vector bosons for the $SU(2)_L$ group ($W_\mu^{1,2,3}$) and one vector boson for the $U(1)$ group (B_μ) are introduced, requiring a local symmetry of the free fermion field Lagrangian for phase transformation of all fields and a rotation of the isospin left-handed doublets. The gauge

couplings of the W_μ and of the B_μ to the fermions are defined by two constants, g and g', corresponding to two symmetry groups $SU(2)_L$ and $U(1)$, respectively.

The Lagrangian which describes the interactions of the vector bosons with the fermion fields f contains three terms;

$$L = L^{CC} + L^{em} + L^{NC}.$$

The charged current term L^{CC} is given by;

$$L^{CC} = \frac{g}{\sqrt{2}}(J^{\mu+}_{CC} W^-_\mu + h.c.).$$

The charged current is given by,

$$J^{\mu+}_{CC} = \bar{f}_L \gamma^\mu f'_L,$$

where the fields f_L and f'_L represent the members of the weak isodoublet with the third component of 1/2 and -1/2, respectively. The W boson fields are expressed by;

$$W^\pm_\mu = \frac{1}{\sqrt{2}}(W^1_\mu \mp i W^2_\mu).$$

The second, electromagnetic term is;

$$L^{em} = g \sin\theta_{\rm W} (J^\mu_{em} A_\mu + h.c.).$$

The electromagnetic current J^μ_{em} is given by,

$$J^\mu_{em} = q_f \bar{f} \gamma^\mu f$$

for any fermion f with charge q_f. Here, the weak mixing angle $\theta_{\rm W}$ is defined as

$$\sin\theta_{\rm W} = \frac{g'}{\sqrt{g^2 + g'^2}}.$$

The photon field is expressed by;

$$A_\mu = \sin\theta_{\rm W} W^3_\mu + \cos\theta_{\rm W} B_\mu.$$

Comparing the Lagrangian with that of the usual electromagnetic interaction, it follows that

$$e = g \sin\theta_{\rm W},$$

where e is the electron charge.

The third term is the weak neutral current (NC) Lagrangian;

$$L^{NC} = \frac{e}{\sin\theta_{\rm W} \cos\theta_{\rm W}} (J^\mu_{NC} Z_\mu + h.c.).$$

The neutral current J^μ_{NC} is given by;

$$J^\mu_{NC} = c^f_V \bar{f} \gamma^\mu f - c^f_A \bar{f} \gamma^\mu f$$

for any fermion. The vector and axial-vector coupling constants c_V^f and c_A^f are defined by

$$c_V^f = I_3 - 2q_f \sin^2\theta_{\rm W},$$

$$c_A^f = I_3,$$

where I_3 is the third component of the weak isospin. The Z^0 boson is described by the field Z_μ obtained by a linear combination of the B_μ and W_μ^3 fields,

$$Z_\mu = \cos\theta_{\rm W} W_\mu^3 - \sin\theta_{\rm W} B_\mu.$$

The above formulations describe massless gauge bosons and massless fermions. Their masses are generated by spontaneous breaking of the $SU(2) \times U(1)$ symmetry. In order that the weak bosons are massive and the photon is kept massless, four real scalar fields ϕ_i are introduced to form a Higgs doublet

$$\phi = \begin{pmatrix} \phi^+ \\ \phi^0 \end{pmatrix}, \phi^+ = \frac{1}{\sqrt{2}}(\phi_1 + i\phi_2), \phi^0 = \frac{1}{\sqrt{2}}(\phi_3 + i\phi_4),$$

and $SU(2) \times U(1)$ gauge invariant lagrangian for these fields is taken as

$$L^{Higgs} = \mid (i\partial_\mu - g\frac{\vec{\sigma}}{2} \cdot \vec{W}_\mu - g'\frac{Y}{2}B_\mu)\phi \mid^2 - V(\phi).$$

The arrangement of the four fields in an isospin doublet with weak hypercharge $Y = 1$ is the most economical choice to keep the Lagrangian gauge invariant. In L^{Higgs}, $\vec{\sigma}$'s are the Pauli mtrices, and

$$V(\phi) = \mu^2\phi^\dagger\phi + \lambda(\phi^\dagger\phi)^2$$

is the field potential. The parameters λ is positive and μ^2 is negative. The $\mu^2 < 0$ is required for the spontaneous symmetry breaking of the theory. A vacuum expectation value ϕ_0 of these fields is chosen as

$$\phi_0 \equiv \frac{1}{\sqrt{2}} \begin{pmatrix} 0 \\ v \end{pmatrix}.$$

The gauge boson masses are obtained by substituting the vacuum expectation value in the Lagrangian. The relevant term becomes

$$\mid (-ig\frac{\vec{\sigma}}{2} \cdot \vec{W}_\mu - ig'\frac{Y}{2}B_\mu)\phi \mid^2 = (\frac{1}{2}vg)^2 W_\mu^+ W^{-\mu} + \frac{v^2}{8}(W_\mu^3, B_\mu) \begin{pmatrix} g^2 & -gg' \\ -gg' & g'^2 \end{pmatrix} \begin{pmatrix} W^{3\mu} \\ B^\mu \end{pmatrix}.$$

The charged W boson masses can be read off directly from the first term,

$$M_{\rm W} = \frac{1}{2}vg \ .$$

The second term becomes diagonal with the fields A_μ and Z_μ, gives the masses,

$$M_{\rm A} = 0,$$

$$M_{\rm Z} = \frac{1}{2} v \sqrt{g^2 + g'^2} \ .$$

Therefore we can obtain a mass relation,

$$M_{\rm Z} = \frac{M_{\rm W}}{\cos\theta_{\rm W}}.$$

In a similar way, the fermion masses can also be generated with the same Higgs doublet. The complete Lagrangian of the electroweak interaction including the mass terms of fermion is summarised as;

$$\begin{aligned} L &= -\frac{1}{4}\vec{W}_{\mu\nu}\vec{W}^{\mu\nu} - \frac{1}{4}B_{\mu\nu}B^{\mu\nu} \\ &\quad + \bar{f}_L\gamma^\mu(i\partial_\mu - g\frac{\vec{\sigma}}{2}\cdot\vec{W}_\mu - g'\frac{Y}{2}B_\mu)f_L \\ &\quad + \bar{f}_R\gamma^\mu(i\partial_\mu - g'\frac{Y}{2}B_\mu)f_R \\ &\quad + \mid (i\partial_\mu - g\frac{\vec{\sigma}}{2}\cdot\vec{W}_\mu - g'\frac{Y}{2}B_\mu)\phi \mid^2 - V(\phi) \\ &\quad - (G_1\bar{f}_L\phi f_R + G_2\bar{f}_L\phi_c f_R + h.c.). \end{aligned}$$

The first and second terms give the kinematic energies and self interactions of the gauge bosons ($\rm W^{\pm}, Z^0, \gamma$). The third and forth terms give the kinematic energies of fermions (leptons and quarks) and their interactions with the gauge bosons. The fifth gives the masses of gauge bosons and their couplings to the Higgs boson. The last one gives the masses of the leptons and quarks and their couplings to the Higgs boson.

Appendix B

Event Selection used in the 161 GeV Analysis

B.1 $W^+W^- \to q\bar{q}'q''\bar{q}'''$ event selection

Selected events are firstly identified as hadronic final states [33]: they should have at least six tracks and six electromagnetic clusters, the sum of measured energies more than 50 GeV using tracks, electromagnetic clusters and hadronic clusters. Tracks and calorimeter clusters are then combined into four jets using the "Durham" jet-finding algorithm [30], and the energy and momentum of each jet are corrected to reduce for double-counting [31].

Events having an energetic initial state photon in the detector are removed by demanding the energy of the most energetic electromagnetic cluster to be less than $0.71E_\gamma$, where E_γ is the expected energy of an initial state photon produced in association with a real Z^0 (E_γ = 54.7 GeV at $\sqrt{s}$ = 161 GeV). A well separated four-jet topology is ensured by requiring events to have the jet resolution parameter for the three- to four-jet transition, $y_{34} > 0.01$. Events are rejected if any jet contains no tracks, in order to remove poorly reconstructed jets and radiative events which satisfy the E_γ criterion above. The four-vectors of the jets are used in a kinematic fit, which imposes conservation of energy and momentum and equality of the masses of the two jet pairs forming the W candidates. At least one of the three possible assignments of the jets to W candidates must yield a fitted mass of more than 72 GeV, with a corresponding fit probability of at least 1%. These requirements remove more than 99% of the $Z^0/\gamma \to q\bar{q}$ background.

B.2 $W^+W^- \to q\bar{q}'e\bar{\nu}_e$ and $q\bar{q}'\mu\bar{\nu}_\mu$ event selection

Purely leptonic final states are removed by requiring at least six tracks and at least eight electromagnetic calorimeter clusters in an event. A muon candidate is a track which has associated hits in the muon chambers or the hadron calorimeter, and has only a small energy deposit in the electromagnetic calorimeter. Electrons are identified by requiring a tight matching between the measured ϕ coordinates of a track and an electromagnetic cluster, by removing tracks consistent with photon conversions, and by requiring the ionisation energy loss, dE/dx, and the ratio of the electromagnetic cluster energy, E, to the track momentum, p, to be consistent with the expectation for an electron. Rejecting events with significant associated hadronic activity beyond the electromagnetic calorimeter further enhances the purity of the $q\bar{q}'e\bar{\nu}_e$ sample.

As the lepton candidate should be energetic, muons are required to have momentum $|\vec{p}| > 20$ GeV, and electrons to have energy $E > 25$ GeV. In the region $|\cos\theta| > 0.90$, residual photon conversion background is reduced by insisting that electron candidates also satisfy $|\vec{p}| > 25$ GeV. The lepton candidate must be isolated, *i.e.* $I \equiv \sum E + \sum |\vec{p}| < 2.5$ GeV, where the sum includes all tracks and clusters within a 200 mrad cone around the lepton track, excluding the cluster associated with the track. To remove events containing $Z^0 \to \ell^+\ell^-$ decays, lepton candidates are rejected if their invariant mass together with any other track is within 10 GeV of the Z^0 mass. The total visible energy and momentum of the event, $(E_{\rm vis}, \vec{p}_{\rm vis})$, are evaluated using the algorithm of [31] for the hadronic system, and adding the four-momentum of the lepton candidate.

A $W^+W^- \to q\bar{q}'\ell\bar{\nu}_\ell$ event has a high momentum neutrino, and therefore has missing momentum and a reduced visible energy. Radiative Z^0/γ background events and singly resonant gauge boson events tend to have missing momentum along the beam direction, whereas the signal events normally have an unbalanced momentum in the $r-\phi$ plane. The following criteria exploit these characteristics. Events are required to have the jet resolution parameter in the "Durham" scheme for the two- to three-jet transition, $y_{23} > 0.005$, evaluated using tracks and unassociated electromagnetic clusters. The energy of the most energetic isolated electromagnetic cluster must be less than $0.75E_\gamma$. Events are required to have a scaled missing momentum, $R_{\rm miss} = |\vec{p}_{\rm miss}|/\sqrt{s} > 0.07$, where $\vec{p}_{\rm miss} = -\vec{p}_{\rm vis}$. The scaled visible energy, $R_{\rm vis} = E_{\rm vis}/\sqrt{s}$, must lie in the interval $0.30 < R_{\rm vis} < 1.00$ (0.95) when the lepton candidate is a muon (electron). The polar angle $\theta_{\rm miss}$ of the missing momentum vector must be in the region given by $|\cos\theta_{\rm miss}| < 0.95$. The $r-\phi$ component of the momentum vector $\vec{p}_{\rm vis}$ is used to calculate the total transverse momentum in the event, $\sum p_T$, which must be greater than 12 (16) GeV when the lepton candidate is a muon (electron).

B.3 $W^+W^- \to q\bar{q}'\tau\bar{\nu}_\tau$ event selection

Events must be identified as hadronic [33], consisting of at least six tracks and eight electromagnetic clusters, and should not be selected as $W^+W^- \to q\bar{q}'q''\bar{q}'''$, $q\bar{q}'e\bar{\nu}_e$ or $q\bar{q}'\mu\bar{\nu}_\mu$. Three jets are formed in the event using the $k_\perp$ algorithm and, in contrast to the $q\bar{q}'\mu\bar{\nu}_\mu$ and $q\bar{q}'e\bar{\nu}_e$ selections where a high energy charged lepton has been identified, the total energy and momentum of the entire event are corrected as in [31]. Events are required to satisfy the following conditions: $|\cos\theta_{\rm miss}| < 0.85$, $R_{\rm miss} > 0.1$, $0.3 < R_{\rm vis} < 0.9$ and $y_{23} > 0.005$, where the variables are as described in the previous selection. In this case, as no lepton is explicitly identified, some of the criteria are slightly more restrictive than the previous selection. Requiring that all jets have at least one associated charged track removes events in which an energetic photon is reconstructed as a jet.

The pair of jets with the largest opening angle is assumed to be the $q\bar{q}$ pair from the hadronic W decay, leaving the remaining jet as the τ candidate. Monte Carlo studies of $W^+W^- \to q\bar{q}'\tau\bar{\nu}_\tau$ events indicate that this assignment is correct in 75% of events. It fails when the τ lepton is not well separated from one of the quark jets, or the W^+W^- pair is sufficiently off-shell that the decay products of the hadronically decaying W are no longer the back-to-back pair of the jets. The jet assigned as the τ candidate is required to have either one or three tracks within 10° of the jet axis. It must also have less than 1.5 GeV of isolation energy, I, between 10° and 20° from the jet axis.

B.4 $W^+W^- \rightarrow \ell^-\bar{\nu}_\ell\ell'^+\nu_{\ell'}$ event selection

Identifications of electrons and muons are the same as the $q\bar{q}'e\bar{\nu}_e$ and $q\bar{q}'\mu\bar{\nu}_\mu$ channels. Cone jets[1] [38] are formed in low multiplicity events [39] having between two and six tracks, and a total number of charged tracks and electromagnetic clusters less than 13. Two- and three-jet events are selected: two jets are required to contain tracks, and at least one of these jets should also include an electromagnetic cluster. One more jet without any tracks is accepted to allow for photon radiation. Vetoes are made against events which are consistent with $Z^0/\gamma \rightarrow \ell^+\ell^-$ or with having a hard initial state photon in the detector, and against events which have muons close to the beam axis or jets with the same charge.

Two-jet events must be consistent with a di-lepton having significant missing energy and transverse momentum. One jet must have $|\cos\theta| < 0.96$ and the other $|\cos\theta| < 0.90$, their opening angle must be less than 170°, all tracks in the event must be associated with a jet, and events without identified electrons or muons must have electromagnetic clusters present in both jets. Acoplanarity, $\phi_{\rm acop}$, is defined as 180° minus the di-jet opening angle in the $r-\phi$ plane. Events with $\phi_{\rm acop} > 60°$ must have $|\cos\theta_{\rm miss}| < 0.90$. For events with $\phi_{\rm acop} < 60°$, the transverse momentum perpendicular to the event thrust axis[2], $a_t^{\rm miss}$, and the direction of the associated missing momentum, $\theta_a^{\rm miss}$, are required to satisfy $a_t^{\rm miss}/E_{\rm beam} > 0.025$ and $|\cos\theta_a^{\rm miss}| < 0.99$. Here $E_{\rm beam}$ is the beam energy, $\theta_a^{\rm miss} = \tan^{-1}(a_t^{\rm miss}/p_z^{\rm miss})$ and $-p_z^{\rm miss}$ is the longitudinal missing momentum [40].

Events are finally selected if they satisfy all criteria in any of the categories defined in Table B.1. Events may be selected by up to three independent selections. Category A is optimised for e^+e^-, $\mu^+\mu^-$ and $e^\pm\mu^\mp$ events and is independent of lepton identification, category B is based on significant missing transverse energy and requires at least one identified e or μ, and category C is based on identification of the di-lepton classes. C is further subdivided into four exclusive categories: C1 requires two e's or two μ's, C2 requires no e or μ identification, C3 requires one e and one μ, while C4 requires one jet to be identified as e or μ and the other not to be identified.

Three-jet events must have fewer than five tracks, be aplanar, have at least one identified e or μ, satisfy $|\cos\theta_{\rm miss}| < 0.90$, have a transverse momentum greater than $0.2E_{\rm beam}$, and be kinematically inconsistent with a $\tau\tau\gamma$ final state [41]. The event is defined as aplanar if the sum of the opening angles among the three di-jet parings is less than 350°. In addition, the energy sum of the third jet and the jet closer to the third must exceed $0.35E_{\rm beam}$.

[1] The cone jet parameters of a minimum energy of 2.5 GeV and a cone half angle of 20° are used.

[2] This reduces the sensitivity to neutrinos from tau decays or poorly measured particles.

Observable	Category					
	A	B	C1	C2	C3	C4
Lepton identification required	None	>1 e or μ	ee or $\mu\mu$	no e or μ	1 e and 1 μ	1 e or 1 μ not both
$\phi_{\rm acop}$(degrees)	>7.5	>20.0	>7.5	>15.0	>5.0	>7.5
x_T	>0.08	>0.20	>0.08	>0.08	–	>0.08
x_1	$>0.75-x_2$	–	>0.35	>0.20	>0.35	>0.35
x_2	>0.325	–	>0.10	>0.10	>0.05	>0.05
$m_{\ell\ell}$ (GeV)	–	>10.0	>10.0	>10.0	–	–
$\lvert m_{\rm recoil}-M_{\rm Z}\rvert$ (GeV)	–	$>3\Gamma_{\rm Z}$	$>3\Gamma_{\rm Z}$	–	–	–

Table B.1: Di-jet analysis kinematic cut values for the $\rm W^+W^-\ \rightarrow\ \ell^-\bar{\nu}_\ell\ell'^+\nu_{\ell'}$ selection, where $\phi_{\rm acop}$ is the di-jet acoplanarity angle, x_T is the transverse momentum of the event scaled by the beam energy, $x_{1(2)}$ is the energy of the more (less) energetic jet scaled by the beam energy, $m_{\ell\ell}$ is the di-lepton mass, and $m_{\rm recoil}$ its recoil mass. The $\rm Z^0$ mass and width are taken to be $M_{\rm Z}=91.19$ GeV and $\Gamma_{\rm Z}=2.5$ GeV respectively.

Appendix C

Event Selection used in the 172 GeV Analysis

C.1 $W^+W^- \rightarrow q\bar{q}'q''\bar{q}'''$ event selection

The selection of $W^+W^- \rightarrow q\bar{q}'q''\bar{q}'''$ events is divided into two parts, namely the preselection and the likelihood based discriminant formed from a combination of seven observables.

C.1.1 Preselection

Candidate events are required to be classified as hadronic [33] and not to be selected by the $W^+W^- \rightarrow q\bar{q}'\ell\bar{\nu}_\ell$ selections described in the next section. Tracks and calorimeter clusters are combined into four jets using the Durham jet-finding algorithm [30], and the total momentum and energy of each jet are corrected for double-counting of energy [31]. To remove events which are clearly inconsistent with $W^+W^- \rightarrow q\bar{q}'q''\bar{q}'''$, predominantly radiative $Z^0/\gamma \rightarrow q\bar{q}$ events, candidate events are required to satisfy the following preselection criteria:

- $\sqrt{s'}$, the fitted invariant mass of the hadronic system, must be greater than 140 GeV.
- The energy of the most energetic isolated photon must be less than $0.3\sqrt{s}$.
- The visible energy of the event must be greater than $0.7\sqrt{s}$.
- $y_{23} > 0.003$, where y_{ij} is the value of the jet resolution parameter at which an event is reclassified from i jets to j jets.
- Each jet is required to contain at least one charged track.
- A kinematic fit, which imposes energy and momentum conservation and equality of the W masses, is performed on all three possible assignments of jets to W candidates in the event. At least one of these combinations must result in a convergent fit.

The efficiency of these preselection requirements for $W^+W^- \rightarrow q\bar{q}'q''\bar{q}'''$ events, ϵ_{sig}^{pre}, is 90.3%, whilst rejecting 96.6% of the $Z^0/\gamma \rightarrow q\bar{q}$ events. The total background cross-section after the preselection, σ_{bgd}^{pre}, is estimated to be 4.5 pb. The preselection accepts 99 events in data.

C.1.2 Likelihood Variables

Events satisfying the preselection criteria are subjected to a likelihood selection, which discriminates between signal and the remaining four-jet-like QCD background. The likelihoods are based on a set of seven variables, y_i. The probability density distribution is determined for each y_i, using both simulated $W^+W^- \rightarrow q\bar{q}'q''\bar{q}'''$ and $Z^0/\gamma \rightarrow q\bar{q}$ events. The likelihoods, $L^{q\bar{q}'q''\bar{q}'''}$ and $L^{q\bar{q}}$, are calculated as product of these probabilities. The relative likelihood discriminant, $\mathcal{L}^{q\bar{q}'q''\bar{q}'''}$, is defined in terms of these two likelihoods as:

$$\mathcal{L}^{q\bar{q}'q''\bar{q}'''} = \frac{L^{q\bar{q}'q''\bar{q}'''}}{L^{q\bar{q}'q''\bar{q}'''} + L^{q\bar{q}}}.$$

The value of $\mathcal{L}^{q\bar{q}'q''\bar{q}'''}$, between zero and one, is used to discriminate between signal and background events.

The following seven variables, which use the characteristic four-jet-like nature, momentum balance and angular structure of $W^+W^- \rightarrow q\bar{q}'q''\bar{q}'''$ to distinguish events from the remaining background, are used to construct the likelihoods:

- the logarithm of y_{34},
- the logarithm of y_{45},
- the sphericity S of the event, defined as

  $$S = \frac{3}{2}\min\left(\frac{\sum_j p_{jt}^2}{\sum_j |\vec{p}_j|^2}\right),$$

  where $\vec{p}_j$ is the momentum of a track in a jet and p_{jt} is the transverse component of the momentum with respect to the sphericity axis,
- the quantity J_{mom}, defined as

  $$J_{mom} = \frac{(p_1 + p_2 - p_3 - p_4)}{\sqrt{s}},$$

  where p_i's are the jet momenta, and the jets are ordered by energy such that p_1 is the momentum of the most energetic jet,
- the cosine of the modified Nachtmann-Reiter angle, $\cos\theta_{N-R}$ (see [42]),
- the cosine of the angle between the two least energetic jets, $\cos\theta_{34}$,
- the logarithm of the QCD event weight, qcd_{420}[43], which is calculated using the tree level matrix element for the processes $e^+e^- \rightarrow q\bar{q}q\bar{q}, q\bar{q}gg$. This quantity should have large values for hadronic Z^0/γ decays and smaller values for W^+W^- events.

C.2 $W^+W^- \rightarrow q\bar{q}'\ell\bar{\nu}_\ell$ event selection

The selection of $W^+W^- \rightarrow q\bar{q}'\ell\bar{\nu}_\ell$ events is divided into four distinct stages, namely identification of a charged lepton candidate, preselection, relative likelihood selection to separate signal from the remaining background, and event categorisation. Details of each stage are given below.

C.2.1 Identification of the Candidate Electron and Muon

In order to maximise efficiency, no explicit lepton identification is required. Instead, the track which is most consistent with being an electron (muon) from the decay $W \rightarrow e\bar{\nu}_e$ ($W \rightarrow \mu\bar{\nu}_\mu$) is taken to be the candidate lepton in the event. This track is identified using two types of variables: a) lepton identification variables, for example, number of hits in the hadron calorimeter or specific energy loss in the central tracking chamber; and b) variables representing the probability that the lepton arises from a W decay, for example, energy and isolation. These variables are used to calculate, for each track, the probability that the track arises from a $W \rightarrow e\bar{\nu}_e$ decay, $P(e)$, or from a $W \rightarrow \mu\bar{\nu}_\mu$ decay, $P(\mu)$. These probabilities are the products of probabilities from the individual variables, which are determined using probability density functions obtained from the W^+W^- Monte Carlo. The track with the highest value of $P(e)$ is taken to be the candidate electron in the $W^+W^- \rightarrow q\bar{q}'e\bar{\nu}_e$ selection and the track with the highest value of $P(\mu)$ is taken to be the candidate muon in the $W^+W^- \rightarrow q\bar{q}'\mu\bar{\nu}_\mu$ selection. Each event thus yields one candidate electron track and one candidate muon track.

C.2.2 Definition of Variables

Having selected the most likely electron and muon candidates, variables are constructed which are used in the preselection and, subsequently, in the likelihood selection. The following variables are used:

- E_{lept}, the energy of the candidate lepton. For electrons this is calculated using the electromagnetic calorimeter energy; for muons the track momentum is used,
- $\cos\theta_{\mathrm{lpmis}}$, the cosine of the angle between the lepton track and the missing momentum vector,
- $|\cos\theta_{\mathrm{miss}}|$, the cosine of the angle the missing momentum from the beam axis,
- E_{200}, the energy in a cone of 200 mrad around the candidate lepton, evaluated using tracks and ECAL clusters,
- $P(e)$ or $P(\mu)$, the electron or muon identification probability for the candidate lepton track,
- R_{vis}, the visible energy of the event scaled by $\sqrt{s}$,
- y_{23}, where y_{ij} is the value of the jet resolution parameter (Durham scheme [30]) at which an event is reclassified from i jets to j jets,
- $\sum p_T$, the transverse momentum of the event relative to the beam axis, calculated using tracks, ECAL clusters and HCAL clusters,
- $P(s')$, the probability from a kinematic fit which estimates the invariant mass of the event, $\sqrt{s'}$,
- θ_{jet}, the angle between the lepton candidate and the jet axis of the nearest hadronic jet.

C.2.3 Preselection

Preselection cuts are applied to remove events which are clearly inconsistent with $W^+W^- \rightarrow q\bar{q}'\ell\bar{\nu}_\ell$ decays. In particular, the preselections are designed to remove most two-photon events and a significant fraction of the $Z^0/\gamma \rightarrow q\bar{q}$ background. Slightly different preselection cuts are applied in the $W^+W^- \rightarrow q\bar{q}'e\bar{\nu}_e$ and $W^+W^- \rightarrow q\bar{q}'\mu\bar{\nu}_\mu$ selections. Firstly, events are required to have more than five charged tracks and more than seven electromagnetic calorimeter clusters. The main preselection cuts are: $E_{\rm lept} > 10.0$ GeV, $0.30 < R_{\rm vis} < 1.05$, the total energy in the forward luminosity monitors < 40 GeV, $\cos\theta_{\rm lpmis} < 0.0$ and the energy of the highest energy isolated photon in the event $< (E_{\rm ISR}$ - 10) GeV, where $E_{\rm ISR}$ is the expected energy of an initial state photon for radiative events with $\sqrt{s'} \sim M_{\rm Z}$. An isolated photon is defined as an ECAL cluster which is not associated with a track and which satisfies the isolation requirement of less than 2.5 GeV of energy in a 200 mrad cone around the cluster. Finally, loose cuts are applied to the lepton identification probabilities and, in the case of the $W^+W^- \rightarrow q\bar{q}'e\bar{\nu}_e$ selection, several cuts are additionally made to reduce the background from converting photons. The preselection is approximately 92% efficient for $W^+W^- \rightarrow q\bar{q}'e\bar{\nu}_e$ and $q\bar{q}'\mu\bar{\nu}_\mu$ events, where about half the loss in efficiency arises from cases where the lepton is outside the experimental acceptance. The preselection cuts remove approximately 90% of the $Z^0/\gamma \rightarrow q\bar{q}$ background.

C.2.4 Relative Likelihood Selection

For events passing the electron preselection, a relative likelihood method is used to distinguish $W^+W^- \rightarrow q\bar{q}'e\bar{\nu}_e$ events from the background of $Z^0/\gamma \rightarrow q\bar{q}$ events. After the preselection cuts the signal to background ratio is still less than 0.1. The likelihoods are based on a set of variables, x_i, where the observed values are compared to the expected distributions (obtained from Monte Carlo) for $W^+W^- \rightarrow q\bar{q}'e\bar{\nu}_e$ events from which the probabilities, $P_i(x_i)$, are obtained. The likelihood, $L^{q\bar{q}'e\bar{\nu}_e}$, is calculated as the product of these probabilities for the individual variables used in the analysis. The background likelihood, $L^{q\bar{q}}$, is obtained in the same way using Monte Carlo distributions for $Z^0/\gamma \rightarrow q\bar{q}$ events. The relative likelihood, $\mathcal{L}^{q\bar{q}'e\bar{\nu}_e}$, is calculated as:

$$\mathcal{L}^{q\bar{q}'e\bar{\nu}_e} = \frac{L^{q\bar{q}'e\bar{\nu}_e}}{L^{q\bar{q}'e\bar{\nu}_e} + f \times L^{q\bar{q}}},$$

where the normalisation factor, f, is the ratio of preselected background to signal cross-sections from Monte Carlo. The variables used in the $W^+W^- \rightarrow q\bar{q}'e\bar{\nu}_e$ likelihood are: $E_{\rm lept}$, E_{200}, $P(e)$, y_{23}, $R_{\rm vis}$, $|\cos\theta_{\rm miss}|$, $\sum p_T$, $\cos\theta_{\rm lpmis}$, $P(s')$ and $\theta_{\rm jet}$. The $q\bar{q}'\mu\bar{\nu}_\mu$ relative likelihood, $\mathcal{L}^{q\bar{q}'\mu\bar{\nu}_\mu}$, is obtained in a similar way with a slightly modified set of variables; with $P(\mu)$ replacing $P(e)$ and $\theta_{\rm jet}$ not used. The inclusion of $\theta_{\rm jet}$ in the $q\bar{q}'e\bar{\nu}_e$ likelihood is to improve the signal and background separation whereas in the $q\bar{q}'\mu\bar{\nu}_\mu$ selection this is not the case.

C.2.5 Event Categorisation

Although the above likelihood selections are optimised to separate $W^+W^- \rightarrow q\bar{q}'e\bar{\nu}_e$ and $W^+W^- \rightarrow q\bar{q}'\mu\bar{\nu}_\mu$ events from the $Z^0/\gamma \rightarrow q\bar{q}$ background, they also select approximately 25% of $W^+W^- \rightarrow q\bar{q}'\tau\bar{\nu}_\tau$ decays. For this reason events passing the $q\bar{q}'e\bar{\nu}_e$ selection are re-classified as either $W^+W^- \rightarrow q\bar{q}'e\bar{\nu}_e$ or $W^+W^- \rightarrow q\bar{q}'\tau\bar{\nu}_\tau$, and events passing the $q\bar{q}'\mu\bar{\nu}_\mu$

selection are re-classified as either $W^+W^- \rightarrow q\bar{q}'\mu\bar{\nu}_\mu$ or $W^+W^- \rightarrow q\bar{q}'\tau\bar{\nu}_\tau$. The predominant $W^+W^- \rightarrow q\bar{q}'\tau\bar{\nu}_\tau$ contamination in the $q\bar{q}'e\bar{\nu}_e$ selection arises from cases where the tau lepton decays to an electron or decays into a one prong hadronic final state. Therefore, for events identified as $W^+W^- \rightarrow q\bar{q}'\tau\bar{\nu}_\tau$, two relative likelihoods, analogous to those described in the previous section, are constructed using the same variables as were used in the $W^+W^- \rightarrow q\bar{q}'e\bar{\nu}_e$ likelihood selection. The first relative likelihood attempts to separate $W^+W^- \rightarrow q\bar{q}'\tau\bar{\nu}_\tau \rightarrow q\bar{q}(e\bar{\nu}_e\nu_\tau)\bar{\nu}_\tau$ decays from $W^+W^- \rightarrow q\bar{q}'e\bar{\nu}_e$ decays and the second attempts to separate $W^+W^- \rightarrow q\bar{q}'\tau\bar{\nu}_\tau \rightarrow q\bar{q}(\pi^\pm n\pi^0\nu_\tau)\bar{\nu}_\tau$ from $W^+W^- \rightarrow q\bar{q}'e\bar{\nu}_e$. If either of these relative likelihoods is greater than 0.5 the event is re-categorised as $W^+W^- \rightarrow q\bar{q}'\tau\bar{\nu}_\tau$. A similar procedure is applied to events passing the $W^+W^- \rightarrow q\bar{q}'\mu\bar{\nu}_\mu$ selection. The result of the event categorisation is that all events passing the $q\bar{q}'e\bar{\nu}_e$ and $q\bar{q}'\mu\bar{\nu}_\mu$ selections are categorised as either $W^+W^- \rightarrow q\bar{q}'e\bar{\nu}_e$, $W^+W^- \rightarrow q\bar{q}'\mu\bar{\nu}_\mu$ or $W^+W^- \rightarrow q\bar{q}'\tau\bar{\nu}_\tau$.

C.2.6 $W^+W^- \rightarrow q\bar{q}'\tau\bar{\nu}_\tau$ Event Selection

A relative likelihood selection designed to separate $W^+W^- \rightarrow q\bar{q}'\tau\bar{\nu}_\tau$ from $Z^0/\gamma \rightarrow q\bar{q}$ background is applied to events which fail the $W^+W^- \rightarrow q\bar{q}'e\bar{\nu}_e$ and $W^+W^- \rightarrow q\bar{q}'\mu\bar{\nu}_\mu$ selections. Approximately 25% of events finally selected as $W^+W^- \rightarrow q\bar{q}'\tau\bar{\nu}_\tau$ are from the analysis given in above sections, the remaining events being selected as summarised below. The $W^+W^- \rightarrow q\bar{q}'\tau\bar{\nu}_\tau$ event selection proceeds in a similar manner to the $W^+W^- \rightarrow q\bar{q}'e\bar{\nu}_e$ selection, *i.e.* 'lepton' identification, preselection and relative likelihood selection. In this case no additional event categorisation is performed. The selection has been designed to be sensitive to the four main tau decay classes: electron, muon, hadronic one prong and hadronic three prong. Consequently four separate selections are applied. The lepton identification of the $W^+W^- \rightarrow q\bar{q}'e\bar{\nu}_e$ selection is replaced by the identification of the track most consistent with being from $W \rightarrow \tau\bar{\nu}_\tau \rightarrow (e\bar{\nu}_e\nu_\tau)\bar{\nu}_\tau$, $W \rightarrow \tau\bar{\nu}_\tau \rightarrow (\mu\bar{\nu}_\mu\nu_\tau)\bar{\nu}_\tau$ and $W \rightarrow \tau\bar{\nu}_\tau \rightarrow (\pi^\pm n\pi^0\nu_\tau)\bar{\nu}_\tau$ decays. To be sensitive to three prong tau decays, the combination of three tracks which is most consistent with a $W \rightarrow \tau\bar{\nu}_\tau \rightarrow (2\pi^\pm\pi^\mp\nu_\tau)\bar{\nu}_\tau$ decay is also identified. The $W^+W^- \rightarrow q\bar{q}'\tau\bar{\nu}_\tau$ selection then proceeds as four preselections, one for each of the above cases, and four corresponding likelihood selections. The variables used in the likelihood are similar to those used above but include more information about the track (or tracks) identified as the tau decay *e.g.* the invariant mass of all tracks and clusters within a 200 mrad cone around the track. An event with a relative likelihood greater than 0.75 for any of the four tau likelihoods, is categorised as a $W^+W^- \rightarrow q\bar{q}'\tau\bar{\nu}_\tau$ event.

Bibliography

[1] OPAL Collaboration, K. Ackerstaff *et al.*, Phys. Lett. **B389** (1996) 416.

[2] OPAL Collaboration, K. Ackerstaff *et al.*, *Measurement of the W Boson Mass and W^+W^- Production and Decay properties in e^+e^- Collisions at $\sqrt{s}$=172 GeV*, CERN-PPE/97-116, Submitted to Z. Phys. C.

[3] The Particle Data Group, R.M. Barnett *et al.*, Phys. Rev. **D54** (1996) 1.

[4] CDF Collaboration, F. Abe *et al.*, Phys. Rev. Lett. **75** (1995) 11, Phys. Rev. **D52** (1995) 4784;
CDF Collaboration, F. Abe *et al.*, Phys. Rev. Lett. **65** (1990) 2243, Phys. Rev. **D43** (1991) 2070;
UA2 Collaboration, J. Alitti *et al.*, Phys. Lett. **B276** (1992) 354;
UA1 Collaboration, C. Albajar *et al.*, Z. Phys. **C44** (1989) 15.

[5] D0 Collaboration, S. Abachi *et al.*, Phys. Rev. Lett. **77** (1996) 3309.

[6] Proceedings of CERN LEP2 Workshop, CERN 96-01, Vols. 1 and 2,
eds. G. Altarelli, T. Sjöstrand and F. Zwirner, February 1996.

[7] Kyungsik Kang and Sin Kyu Kang, *The minimal Supersymmetric Standard Model and Precision of W-Boson mass and Top Quark Mass*, BROWN-HET-1092, hep-ph/9708409, August 1997.

[8] D. Bardin *et al.*, Nucl. Phys. B, Proc. Suppl. **37B** (1994) 148;

[9] S. Myers, "LEP2: PRESENT AND FURURE PERFORMANCE AND LIMITAIONS", 1997 Particle Accelarator Conference, Vancouver Canada, May 1997, CERN-SL/97-022(DI).

[10] OPAL Collaboration, K. Ahmet *et al.*, Nucl. Instr. Meth. **A305** (1991) 275;
P.P. Allport *et al.*, Nucl. Instr. Meth. **A324** (1993) 34;
P.P. Allport *et al.*, Nucl. Instr. Meth. **A346** (1994) 476.

[11] M. Hauschild *et al.*, Nucl. Instr. Meth. **A314** (1992) 74;
O. Biebel *et al.*, Nucl. Instr. Meth. **A323** (1992) 169.

[12] B.E. Anderson *et al.*, IEEE Transactions on Nuclear Science, **41** (1994) 845.

[13] OPAL Collaboration, G. Alexander *et al.*, Phys. Lett. **B376** (1996) 232.

[14] LEP Energy Working Group, *LEP Energy Calibration in 1996*, LEP Energy Group/97-01, 20th March 1997.

[15] S. Jadach, E. Richter-Wąs, B.F.L. Ward and Z. Wąs, Comput. Phys. Commun. **70** (() 1992) 305.

[16] L. Arnaudon *et al.*, Z. Phys. **C66** (1995) 45.

[17] J. Allison *et al.*, Nucl. Instr. Meth. **A317** (1992) 47.

[18] J. Fujimoto *et al.*, Comput. Phys. Commun. **100** (1997) 128.

[19] F.A. Berends, R. Pittau and R. Kleiss, Comput. Phys. Commun. **85** (1995) 437.

[20] T. Sjöstrand, Comput. Phys. Commun. **82** (1994) 74.

[21] M. Skrzypek *et al.*, Comput. Phys. Commun. **94** (1996) 216;
M. Skrzypek *et al.*, Phys. Lett. **B372** (1996) 289.

[22] G. Marchesini *et al.*, Comput. Phys. Commun. **67** (1992) 465.

[23] L. Lönnblad, Comput. Phys. Commun. **71** (1992) 15.

[24] S. Jadach *et al.*, Comput. Phys. Commun. **79** (1994) 503.

[25] S. Jadach, W. Placzek, B.F.L. Ward, Phys. Lett. **B390** (1997) 298.

[26] J. Hilgart, R. Kleiss and F. Le Diberder, Comput. Phys. Commun. **75** (1993) 191.

[27] R. Engel and J. Ranft, Phys. Rev. **D54** (1996) 4244;
R. Engel, Z. Phys. **C66** (1995) 203.

[28] A. Buijs, W.G.J. Langeveld, M.H. Lehto and D.J. Miller, Comput. Phys. Commun. **79** (1994) 523.

[29] J.A.M. Vermaseren, Nucl. Phys. **B229** (1983) 347.

[30] N. Brown and W.J. Stirling, Phys. Lett. **B252** (1990) 657;
S. Bethke, Z. Kunszt, D. Soper and W.J. Stirling, Nucl. Phys. **B370** (1992) 310;
S. Catani *et al.*, Phys. Lett. **B269** (1991) 432;
N. Brown and W.J. Stirling, Z. Phys. **C53** (1992) 629.

[31] OPAL Collaboration, M.Z. Akrawy *et al.*, Phys. Lett. **B253** (1991) 511.

[32] OPAL Collaboration, K. Ackerstaff *et al.*, CERN-PPE/97-083, Accepted by Z. Phys. C (28/11/97).

[33] OPAL Collaboration, G. Alexander *et al.*, Z. Phys. **C52** (1991) 175.

[34] T. Muta, R. Najima, S. Wakaizumi, Mod. Phys. Lett. **A1** (1986) 203.

[35] DELPHI Collaboration, P. Abreu *et al.*, Phys. Lett. **B397** (1997) 158.
L3 Collaboration, M. Acciarri *et al.*, Phys. Lett. **B398** (1997) 223.
ALEPH Collaboration, R. Barate *et al.*, Phys. Lett. **B401** (1997) 347.

[36] L3 Collaboration, M. Acciarri *et al.*, *Measurements of Mass, Width and Gauge Couplings of the W Boson at LEP* , CERN-PPE/97-98, Submitted to Phys. Lett. B.
ALEPH Collaboration, *W mass measurement through direct reconstruction in ALEPH* , contributed paper to EPS-HEP-97, Jerusalem, EPS-600.
DELPHI Collaboration, *Measurement of the W-pair cross-section and of the W mass in* e^+e^- *interactions at 172 GeV* , contributed paper to EPS-HEP-97, Jerusalem, EPS-347.

[37] LEP Electroweak Working Group, *A combination of Preliminary Electroweak Measurements and Constraints on the Standard Model*, CERN-PPE/97-154, December 1997.

[38] OPAL Collaboration, R. Akers *et al.*, Z. Phys. **C63** (1994) 197.

[39] OPAL Collaboration, M.Z. Akrawy *et al.*, Phys. Lett. **B235** (1990) 379.

[40] OPAL Collaboration, G. Alexander *et al.*, Z. Phys. **C73** (1997) 201.

[41] OPAL Collaboration, G. Alexander *et al.*, Phys. Lett. **B377** (1996) 181.

[42] O. Nachtmann and A. Reiter, Z. Phys. **C16** (1982) 45;
M. Bengtsson, Z. Phys. **C42** (1989) 75.

[43] S. Catani and M.H. Seymour, Phys. Lett. **B378** (1996) 287.